In situ Measurements of Chemical Tracers in the Stratosphere: CO, N_2O, and CH_4

Thesis by

Robert Laird Herman

In Partial Fulfillment of the Requirements

for the Degree of

Doctor of Philosophy

California Institute of Technology

Pasadena, California

1998

(Submitted May 4, 1998)

ACKNOWLEDGMENTS

I must start by sincerely thanking my thesis advisor, Yuk Yung, for his patience, humor, insight, remarkably broad knowledge of atmospheric chemistry, and for introducing me to Chris Webster and allowing me to collaborate with his group at JPL. I thank Chris Webster for being my experimental advisor at JPL, and for his patience, cooperation, and enthusiasm about my thesis project. I also thank the members of his group: Randy May, Dave Scott, Greg Flesch, Lin Kroll, Katy Modarress, Liz Moyer, Hua Hu, Lyatt Jaeglé, and all the others. Ross Salawitch deserves a special thank-you for in-depth discussions and for carefully critiquing my manuscripts and ideas. I thank the Caltech faculty, staff, and students who have made graduate school stimulating and exciting, in particular Andy Ingersol, Geoff Blake, Ed Stolper, George Rossman, Ariel Anbar, Peter Green, Rich Dissly, Hari Nair, Dave Evans, and the folks in the entering class of 1991. Thank-you to Adam Showman for your wonderful friendship. Many support staff have helped this thesis come to fruition: the JPL balloon group, Bob MacMillan, the Space Instruments machine shop, the Chemistry machine shop at Caltech, and many people at Caltech, including Jim O'Donnell, Mike Black, Kay, Irma, Tammie, Donna, Marcia, Bernice, and Priscilla. I especially thank my parents, brother Matt, and sister Sarah for their wonderful support while I have been in school. Thanks to my longtime friends John, Susan, Miguel, and Suzanne for their companionship. Alan Kulawik deserves special thanks for his inestimable help. Last but certainly not least, I thank my wonderful fiancée Jen for her endless patience, care, love, and willingness to put up with my long hours at JPL and in the field.

ABSTRACT

IN SITU MEASUREMENTS OF CHEMICAL TRACERS IN THE STRATOSPHERE: CO, N_2O, AND CH_4

by Robert Laird Herman

Stratospheric transport is studied with measurements of long-lived tracers. The Aircraft Laser Infrared Absorption Spectrometer II (ALIAS II) was designed and built to make *in situ* measurements of atmospheric trace gases at altitudes ranging from 7 km to 30 km. With this spectrometer, nitrous oxide (N_2O) and methane (CH_4) mixing ratios were measured on six high-altitude balloon flights from the tropics (7°S), mid-latitudes (34°N), and high latitudes (65°N). Comparisons of measured mixing ratios with model predictions are used to quantify meridional transport rates in the stratosphere. The mean time scale for entrainment of mid-latitude stratospheric air into the tropics is estimated to be 7^{+10}_{-7} months for altitudes between the tropical tropopause and 20 km, and 16^{+18}_{-8} months for 20 to 28 km. These results suggest that most of the stratospheric entrainment into the tropics occurs at altitudes roughly below 20 km, and that the tropical stratosphere is dynamically isolated from the mid-latitude stratosphere at altitudes between 20 and 28 km.

Faster transport in the lower stratosphere was studied with measurements of atmospheric carbon monoxide (CO) by the ALIAS instrument, predecessor to ALIAS II. This instrument measured CO on fifty eight flights of the NASA

ER-2 high-altitude aircraft from October, 1995, to September, 1997, during two aircraft campaigns: Stratospheric Tracers of Atmospheric Transport (STRAT) and Photochemistry of Ozone Loss in the Arctic Region in Summer (POLARIS). These flights covered altitudes up to 22 km and latitudes from 3°S to 90°N. CO has a photochemical lifetime of only several months in the upper troposphere and lower stratosphere, so its mixing ratio is sensitive to rapid transport. These measurements indicate that quasi-horizontal poleward outflow from the tropical stratosphere occurs on rapid time scales of roughly one month for altitudes between 16 and 20 km.

TABLE OF CONTENTS

LIST OF FIGURES

Number *Page*

Chapter 1.

Chapter 2.

Chapter 3.

LIST OF TABLES

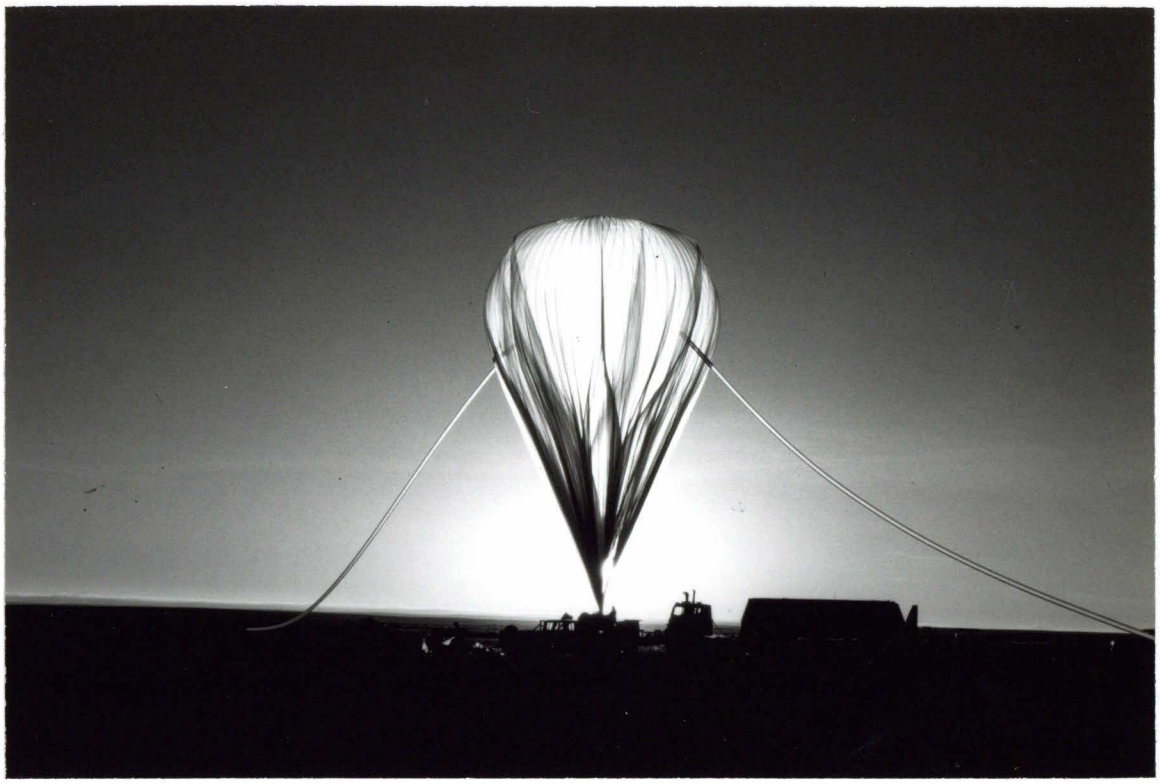

Balloon launch of ALIAS II on the OMS payload, Ft. Sumner, NM, 960921.

Chapter 1

Stratospheric Transport and Tracers - an Overview

1.1 Introduction

In this work, long-lived trace gases are measured in the lower and middle stratosphere in order to infer rates of stratospheric transport. The importance of understanding stratospheric transport is very broad. It is essential for accurate predictions of both future global warming and changes in stratospheric ozone (O_3) concentrations. Global warming is caused by atmospheric buildup of greenhouse (i.e., infrared-active) gases, mainly carbon dioxide (CO_2), nitrous oxide (N_2O), methane (CH_4), and the chlorofluorocarbons (CFCs) [IPCC, 1990]. H_2O is the most important greenhouse gas, but its atmospheric loading is limited by its saturation vapor pressure. CO_2 does not have a significant sink in the stratosphere or mesosphere, so its atmospheric budget is determined by the global carbon cycle [Schlesinger, 1991]. For the other species, though, the global lifetime (i.e., atmospheric residence time) depends on the rate of vertical transport to altitudes where significant photochemical loss occurs. The global lifetime of N_2O is approximately 120 years [WMO, 1995], controlled by photochemical loss in the stratosphere. The CFCs have global lifetimes ranging from 40 to 100 years [WMO, 1995] that are also controlled by stratospheric loss. The largest CH_4 sinks are in the troposphere, yielding a

global lifetime of 10 years [WMO, 1995]. However, the CH_4 that enters the stratosphere has a lifetime of roughly 160 years [Avallone and Prather, 1997] due to slower transport in the stratosphere and slow photochemical loss in the lower stratosphere, as discussed in section 1.3. Perturbations to stratospheric transport can change the global lifetimes of these greenhouse gases and thus affect global warming.

Transport and photochemistry determine the distribution of atmospheric O_3 [Dobson, 1956]. Stratospheric O_3 is important because it shields the biosphere from ultraviolet radiation [e.g., WMO, 1995] and plays an important role in the atmospheric radiation budget, which affects both climate and atmospheric dynamics [e.g., IPCC, 1990]. In the lower stratosphere, the photochemical lifetime of odd oxygen ($O_x = O_3 + O$) is long enough that the distribution of O_3 is controlled mostly by transport. The major catalytic cycles that destroy O_3 in the stratosphere involve reactive species produced from the source gases N_2O, CH_4, H_2O, and the CFCs. These reactive species are indirectly affected by transport through the distribution of their source gases. N_2O is the major source of odd nitrogen ($NO_x = NO + NO_2$), which causes catalytic loss of O_3 [Crutzen, 1970; Johnston, 1971], especially in the middle to upper stratosphere. CH_4 and H_2O are the major sources of odd hydrogen ($HO_x = OH + HO_2$), which also causes catalytic loss of O_3 [Bates and Nicolet, 1950]. The HO_x cycle is the most important O_3 loss mechanism in the lower stratosphere outside of the Arctic and Antarctic polar vortices [e.g., Cohen et al., 1994; Wennberg et al., 1994]. CFC photolysis yields free chlorine ($ClO_x = Cl + ClO$), another catalyst for O_3 loss [Molina and Rowland, 1974],

particularly in the Arctic and Antarctic spring [e.g., WMO, 1995; McElroy et al., 1992]. Many of these reactive species are rapidly removed in the troposphere and thus are also affected by the rate of transport between the stratosphere and troposphere (hereafter called "stratosphere-troposphere exchange").

A practical application of stratospheric transport is found in global atmospheric models used to assess the impact of anthropogenic pollutants on stratospheric O_3. The National Aeronautics and Space Administration (NASA) is currently involved in an assessment of the atmospheric impact of high-speed civil transports (HSCT) [e.g., Stolarski et al., 1995]. These supersonic commercial aircraft, the next generation of the Concorde, would fly at Mach 2.4 in the mid-latitude lower stratosphere at 20 km altitude. Latest economic projections estimate that 1300 to 1900 HSCT could be flying by the year 2025 [A. Wilhite, pers. comm.]. Their NO_x and particle emissions could have a significant impact on O_3 [Johnston, 1971; Crutzen, 1970]. This issue was studied intensively in the early 1970s [e.g., CIAP, 1974], but refinements in models, rate constants, and heterogeneous chemistry lead to the discovery that the impact of NO_x emissions on O_3 is strongly altitude-dependent [e.g., Liu et al., 1980]. One important factor which will be addressed in this study (see Chapter 5) is the time scale for mid-latitude air in the lower stratosphere to be transported to the tropics. Once polluted air is entrained into the tropical stratosphere, it ascends to the region of greatest O_3 production, where enhanced NO_x could be a significant catalytic sink of O_3 [Volk et al., 1996].

1.2 Tracers

A tracer is defined here as a chemical species with production or loss time scales longer than relevant transport time scales. Species that are very short-lived (e.g., HO_x with a lifetime on the order of minutes) are in photochemical steady-state and have concentrations determined solely by local chemistry, not transport. Species that are not destroyed in the atmosphere, e.g., Ar, are totally homogenized by turbulent mixing at altitudes less than 100 km. Between these two extremes are species with a wide range of lifetimes that can be used as probes of atmospheric transport. The most useful tracers are those with photochemical lifetimes within an order of magnitude of transport time scales. The distributions of these species (called "long-lived tracers") are strongly influenced by dynamics, but retain significant spatial gradients due to photochemistry.

The dynamical time scales that are relevant to this discussion affect the regional to global distributions of species in the stratosphere. Throughout the stratosphere, zonal transport (east or west) is much faster than in any other direction. Typical zonal velocities in the stratosphere are 10 to 30 m/s, so global transport time scales are 2 to 6 weeks at the equator and less at higher latitudes, where the latitude circles are smaller. Species with longer photochemical lifetimes are zonally homogeneous in the stratosphere, except in the case of rapid meridional transport associated with waves [e.g., Leovy et al., 1985; Randel et al., 1993; Waugh, 1993].

Meridional transport (north or south) in the stratosphere is usually much slower than zonal transport. Typical meridional velocities are difficult to measure, but are inferred from tracer distributions to be roughly 0.5 m/s. Within one hemisphere, a typical meridional transport time scale is one to three months. However, wave activity can enhance meridional transport at middle latitudes. For instance, quasi-stationary planetary waves cause zonally asymmetric flow in the winter hemisphere of the stratosphere [Brasseur and Solomon, 1986]. When the stratospheric flow becomes zonally asymmetric, a large component of the velocity is in the meridional direction. There are barriers to meridional transport at the edge of the polar vortex (ca. 65° latitude) and in the subtropics (ca. 15° latitude), as described below.

Vertical motion in the stratosphere is extremely slow because the temperature inversion makes this region of the atmosphere very stable. Typical time scales of vertical motion through one scale height (i.e., e-folding vertical length scale) are months to years depending on altitude and latitude. Consider a tracer with concentration given by:

$$n = n_o e^{-z/H} \tag{1.1}$$

where the scale height H is approximately 7 km for inert species but only 5 km for N_2O. By order of magnitude analysis, the vertical advective time scale $\tau_w = H/w$. If the scale height H is 5 km and the vertical velocity w is approximately 0.5 mm/s, then the time scale τ_w is approximately 3 to 4 months [Brasseur and Solomon, 1986].

1.3 Tracer Distributions and Photochemistry

N_2O and CH_4 are excellent tracers in the stratosphere because their volume mixing ratio (i.e., mole fraction, hereafter called "mixing ratio") decreases by at least a factor of two between the tropopause and 30 km altitude. Figures 1 and 2 are the zonal mean distributions of N_2O and CH_4, respectively, predicted by the Caltech-JPL two-dimensional (2D) photochemical model for the month of March. It will be shown in Chapter 4 that this model reproduces the qualitative, large-scale features of N_2O and CH_4, but does not quantitatively agree with the measured N_2O and CH_4.

N_2O is produced by the oceans, bacterial denitrification and nitrification in soils, and anthropogenic sources such as fertilizer production, combustion, nylon production, and biomass burning [e.g., Nevison and Holland, 1997; Schlesinger, 1991; IPCC, 1990]. The tropospheric distribution of N_2O is nearly homogeneous due to its long lifetime. However, the N_2O mixing ratio decreases with altitude in the stratosphere due to large sinks and no significant local sources (see Figure 1). N_2O is destroyed by two loss mechanisms, photolysis and reaction with excited atomic oxygen, $O(^1D)$:

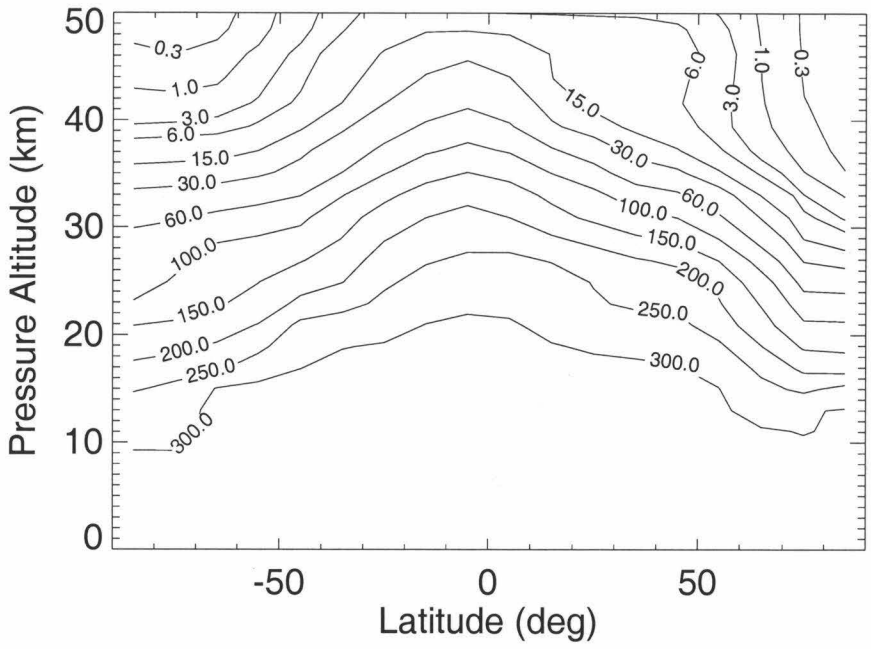

Figure 1. Zonal mean N_2O distribution (ppb) in March from the Caltech-JPL 2D Photochemical Model.

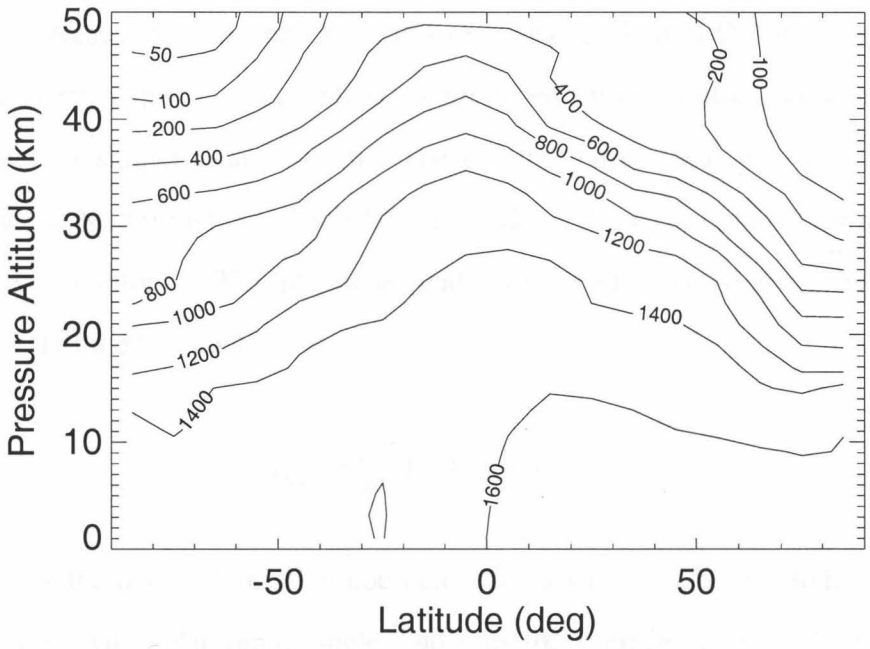

Figure 2. Zonal mean CH_4 distribution (ppb) in March from the Caltech-JPL 2D Photochemical Model.

$$N_2O \xrightarrow{h\nu} N_2 + O(^1D) \tag{1.2}$$

$$\begin{aligned} N_2O + O(^1D) &\rightarrow N_2 + O_2 \quad (42\%) \\ &\quad NO + NO \quad (58\%) \end{aligned} \tag{1.3}$$

Photolysis (1.2) is the dominant sink of N_2O, accounting for more than 90% of the loss. Reaction (1.3) with $O(^1D)$ is a secondary sink of N_2O but the major source of stratospheric NO_x. $O(^1D)$ is produced by O_3 photodissociation at wavelengths shorter than 310 nm. The distribution of local photochemical lifetimes of N_2O from the Caltech-JPL 2D model is shown in Figure 3 for near-equinox conditions. The photochemical lifetime of N_2O is given by the reciprocal of the loss coefficient:

$$\tau_{N_2O} = 1/\left\{J + k_{(1.5)}\left[O(^1D)\right]\right\} \tag{1.4}$$

where J is the photodissociation coefficient or "J-value" of N_2O. Both J and $O(^1D)$ vary with solar zenith angle, and must be averaged over 24 hours to obtain the N_2O lifetime.

CH_4 is produced by anaerobic bacteria associated with swamps, tundra, rice paddies, and enteric fermentation within termites and cattle [e.g., Schlesinger, 1991; IPCC, 1990]. Anthropogenic sources of CH_4 include natural gas production, sewage processing, and other industrial sources. The dominant sink of CH_4 is reaction with OH in the troposphere (see 1.5 below), but the rate is slow relative to transport. Therefore, CH_4 is nearly

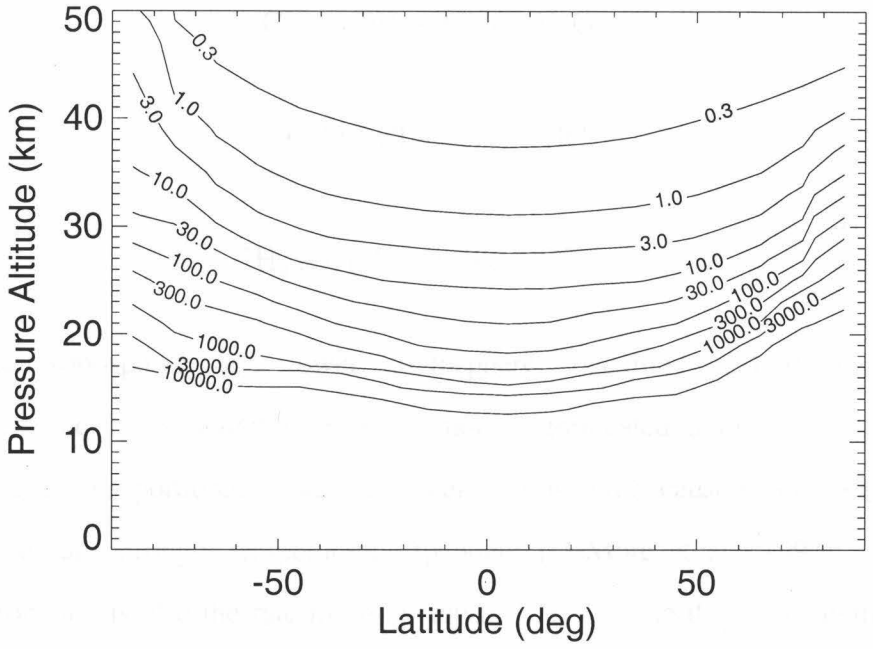

Figure 3. Local photochemical lifetime (yr) of N_2O in March from the Caltech-JPL 2D Photochemical Model. Contours less than 0.3 yr or greater than 10,000 yr are not shown.

homogeneous in the troposphere, except for slightly higher loading in the northern hemisphere due to larger local sources (Figure 2). CH_4 loss rates increase with altitude in the stratosphere, where vertical transport is slow, so the CH_4 mixing ratio decreases with altitude (Figure 2). The initiation step of CH_4 loss is abstraction of H by a free radical, either OH, Cl, or $O(^1D)$:

$$CH_4 + OH \rightarrow CH_3 + H_2O \tag{1.5}$$

$$CH_4 + Cl \rightarrow CH_3 + HCl \tag{1.6}$$

$$CH_4 + O(^1D) \rightarrow CH_3 + OH \tag{1.7}$$

In the troposphere and lower stratosphere, reaction (1.5) dominates. Photochemical destruction of CH_4 is more complicated than that of N_2O because it is proportional to radical concentrations and because reactions (1.5) and (1.6) are strongly temperature dependent [DeMore et al., 1997]. The initiation step is also the rate-limiting step in CH_4 loss, so the photochemical lifetime of CH_4 is given by:

$$\tau_{CH_4} = 1/\left\{k_{(1.7)}[OH] + k_{(1.8)}[Cl] + k_{(1.9)}[O(^1D)]\right\} \tag{1.8}$$

using 24-hour mean radical concentrations. Figure 4 shows the photochemistry of the CH_4 oxidation pathway, based on Logan et al. [1981]. Figure 5 shows the local photochemical lifetimes of CH_4 from the Caltech-JPL 2D model. CH_4 lifetimes have a local maximum near the tropopause due to low OH concentrations and low temperatures.

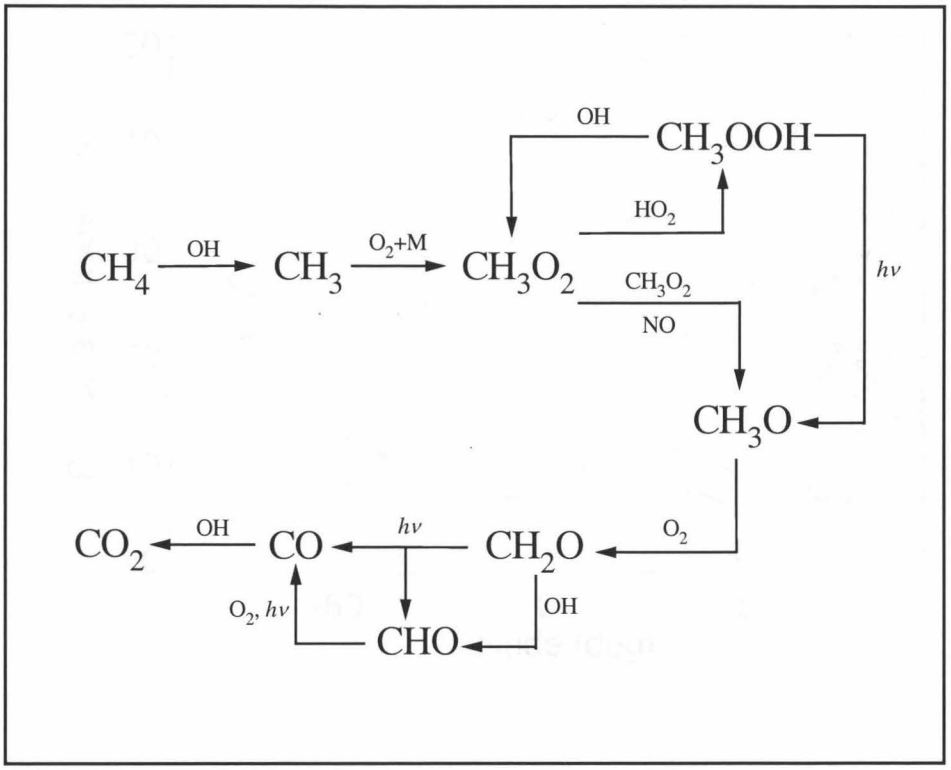

Figure 4. CH_4 oxidation pathway, based on Logan et al. [1981]. In addition to the reactions shown above, tropospheric rainout is an important sink for CH_3OOH and CH_2O.

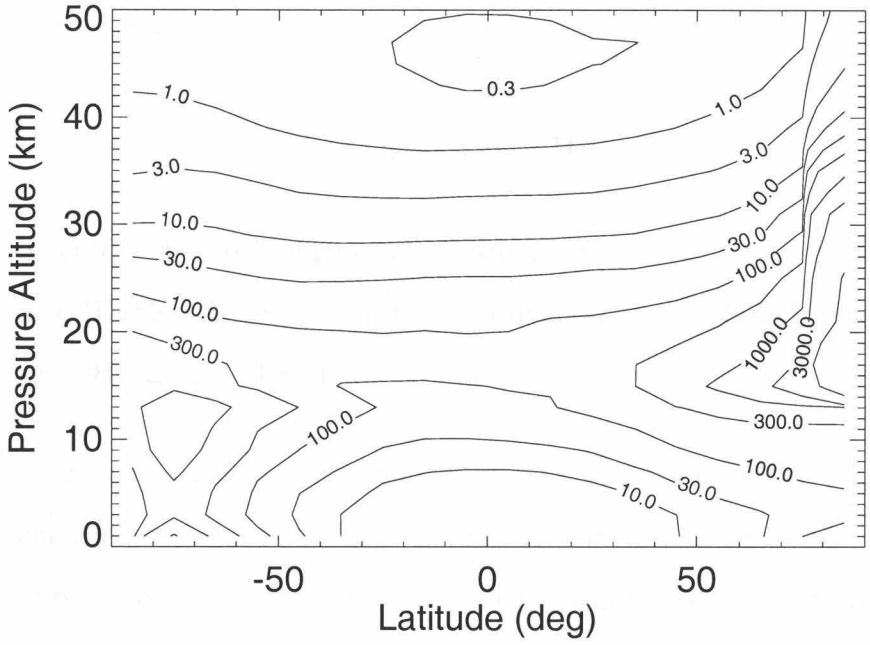

Figure 5. Local photochemical lifetime (yr) of CH_4 in March from the Caltech-JPL 2D Photochemical Model. Contours less than 0.3 yr or greater than 3000 yr are not shown.

Carbon monoxide (CO) is the longest-lived intermediate in the oxidation pathway from CH_4 to CO_2, with a typical stratospheric lifetime of 3 to 6 months (see Chapter 3). In the troposphere, roughly half of the CO source is oxidation of CH_4 and non-methane hydrocarbons (NMHC). The other half comes from biomass burning and direct anthropogenic emissions [Logan et al., 1981]. The dominant CO sink is reaction with OH [Logan et al., 1981; Pressman and Warneck, 1970]:

$$CO + OH \rightarrow CO_2 + H \qquad (1.9)$$

Reaction (1.9) has no temperature dependence, but a slight pressure dependence [DeMore et al., 1997] due to formation of the HOCO transient species [e.g., Hynes et al., 1986].

Figure 6 is the mean distribution of CO measured by the ALIAS instrument aboard the ER-2 aircraft during autumn (see Chapter 3). CO decreases by an order of magnitude within the first 5 km of the stratosphere due to its relatively short photochemical lifetime. Thus, CO is useful as a tracer of transport on monthly time scales in the lower stratosphere. The relatively short lifetime of CO causes large spatial and temporal variability that cannot be totally reproduced in a 2D model because the model grid scale is too coarse and because variations with longitude are important. Predicting atmospheric CO with three-dimensional global circulation models (GCMs) is currently an active field of research [e.g., Allen et al., 1996].

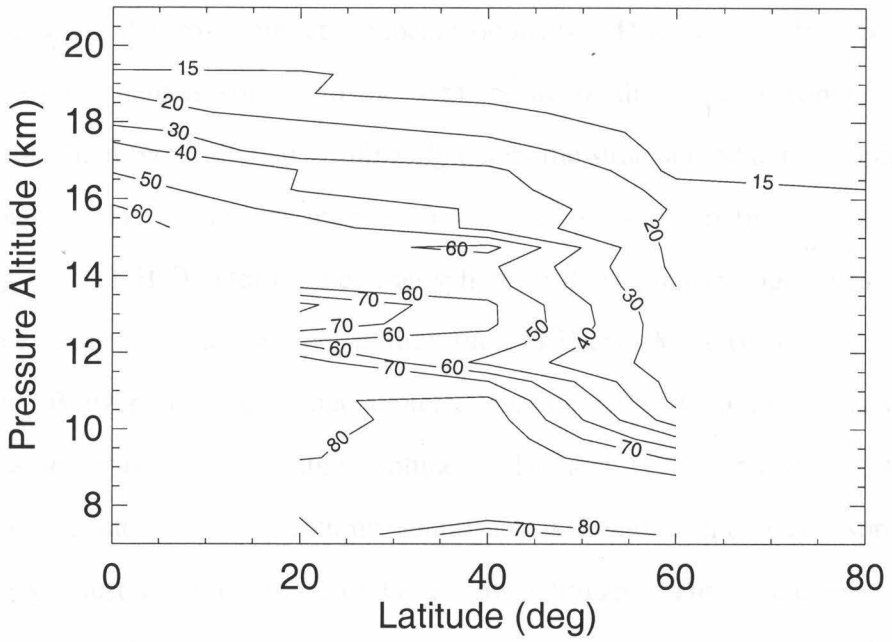

Figure 6. Mean distribution of CO (ppb) in the Northern Hemisphere autumn, as measured by the ALIAS instrument on the ER-2 aircraft.

1.4 Stratospheric Circulation as Inferred from Tracers

The modern picture of stratospheric circulation was inferred by Brewer [1949] and Dobson [1956], based on tracer observations. Brewer noted that the frost point (temperature at which air is saturated with respect to ice) in the mid-latitude lower stratosphere is considerably lower than either the temperature or the frost point at the local tropopause. However, the frost point in the stratosphere is similar to the temperature of the tropical tropopause. From this, he inferred that air dominantly enters the stratosphere at the tropical tropopause. The minimum temperature creates a cold trap that limits the mixing ratio of H_2O entering the stratosphere to its saturation vapor pressure over ice, namely a few parts per million (at 190 K and 90 hPa). By material balance, Brewer concluded that stratospheric air must descend across the tropopause at middle and high latitudes. Dobson [1956] noted that the maximum stratospheric O_3 column abundance is found in the Arctic spring despite greatest net production of O_3 at low latitudes. This could only be explained by poleward advection of air in the stratosphere. Thus, the resultant meridional circulation (called the Brewer-Dobson circulation) consists of rising air in the tropics, poleward transport, and descent at middle and high latitudes. This circulation qualitatively explains the large-scale distribution of tracers in the stratosphere [e.g., Tuck et al., 1997].

Subsequent tracer studies focused on radioactive debris injected into the stratosphere by atmospheric tests of nuclear weapons. The goal of these studies was to explain the long residence times of fallout in the stratosphere. A

series of nuclear detonations in the equatorial Pacific in 1958 released ^{185}W into the stratosphere. At altitudes above 20 km, this radioisotope remained concentrated in the tropical stratosphere, with sharp meridional gradients approximately 20° from the equator [Newell, 1963]. These gradients imply that mixing is slow between the tropics and extra-tropics. Below 20 km, meridional transport out of the tropics appeared to be somewhat faster. In the early 1960s, measurements of ^{14}C and ^{90}Sr from mid- and high latitude atmospheric tests were useful for quantifying time scales for hemispheric and interhemispheric mixing within the stratosphere and stratosphere-troposphere exchange [e.g., Junge, 1963a, b; Sheppard, 1963; Kellogg, 1964; Newell, 1963].

Another major advance associated with these radioisotope measurements was the discovery that the Brewer-Dobson advective circulation must be modified by large-scale quasi-horizontal mixing [Reed and German, 1965]. This mixing is associated with transient eddies [e.g., Brasseur and Solomon, 1986]. Mahlman et al. [1986] and Holton [1986] showed that tracer isopleth slopes are determined by a balance between advection and quasi-horizontal mixing. If the meridional circulation of the stratosphere was purely advective, then isopleths of constant tracer mixing ratio would have steeper slopes than observed. The isopleth slopes are flattened by quasi-horizontal mixing that occurs along isentropes, i.e., surfaces of constant potential temperature (the temperature of an air parcel adiabatically compressed or expanded to 1000 hPa). Species with long lifetimes relative to quasi-horizontal transport time scales are rapidly homogenized along mixing surfaces. Their isopleths have

similar "equilibrium slopes" determined by dynamics [Plumb and Ko, 1992], as seen in the N_2O and CH_4 distributions in Figures 1 and 2, respectively.

This picture of advection modified by quasi-horizontal mixing was used in the development of 2D atmospheric models [e.g., Tung, 1982]. The stratospheric circulation in 2D models is a combination of Brewer-Dobson advection and quasi-horizontal mixing parameterized as "eddy diffusion" [e.g., Shia et al., 1990; Yang et al., 1991]. The mean advective circulation has been shown to be very similar to the diabatic circulation (the circulation caused by heating due to absorption of solar radiation and cooling due to emission of infrared radiation) [Dunkerton, 1978]. A radiative transfer model is usually used to determine the diabatic circulation, but uncertainties are large. The absolute strength of this circulation has been calibrated with the ^{14}C database [Shia et al., 1989]. Quasi-horizontal mixing is determined from dynamical models of stratospheric waves [Summers et al., 1997]. Mixing rates have been refined by comparisons of model tracers, such as N_2O and CH_4, with global satellite observations [e.g., Ko et al., 1993; Solomon et al., 1986; Jones and Pyle, 1984].

Satellite observations of volcanic aerosol have revealed seasonal and interannual variations in stratospheric transport. The dispersion of volcanic aerosol in the stratosphere has been studied for many years to develop a climatology of stratospheric transport [Hitchman et al., 1994]. Trepte and Hitchman [1992] found two transport regimes in the aerosol distributions. Below 20 km in the tropics, there is strong poleward and downward transport, especially in the winter hemisphere. Between 22 and 30 km, the aerosol

loading is concentrated in the tropics and has large meridional gradients in the subtropics, as seen in the ^{185}W data twenty years earlier. At latitudes between roughly 15° and 65°, aerosol and other tracers show flat isopleths due to rapid mixing associated with breaking planetary waves, in the so-called "surf zone" [McIntyre and Palmer, 1983]. This mixing is especially strong in the winter hemisphere. Meridional gradients are largest in the subtropics because this region is on the edge of the "surf zone."

The quasi-biennial oscillation (QBO) in tropical stratospheric winds has profound effects on the shape of the tropical aerosol reservoir [e.g., Trepte and Hitchman, 1992]. The subtropical aerosol gradient is larger when tropical winds are easterly than when they are westerly. Thus, the time scale for transport between the tropics and extra-tropics depends on the phase of the QBO. This is not entirely unexpected because stratospheric wave forcing is quite different in the two phases of the QBO [Andrews et al., 1987].

The isolation of ^{185}W and aerosol in the tropics is evidence that mixing between the tropical and mid-latitude stratosphere is slower than mixing within the "surf zone." Further evidence comes from aircraft measurements of reactive nitrogen (NO_y) and O_3. Murphy et al. [1993] have shown that the ratio of NO_y to O_3 is markedly lower in the tropics than the extra-tropics, with large gradients in the subtropics. These two species are long-lived in the lower stratosphere, so the different ratios of NO_y to O_3 imply that rapid quasi-horizontal mixing does not extend into the tropics [Plumb and Ko, 1992]. H_2O observations by the microwave limb sounder (MLS) and the Halogen Occultation Experiment (HALOE) aboard the Upper Atmosphere Research

Satellite (UARS) indicate that the seasonal cycle of H_2O at the tropical tropopause propagates upward with small attenuation because the tropical stratosphere is relatively isolated from the extra-tropics [Mote et al., 1995; 1996; 1997]. These pieces of evidence lead to the development of the tropical pipe model [Plumb, 1996], in which a subtropical barrier to meridional transport prevents quasi-horizontal mixing between the tropics and extra-tropics. In this case, the only transport in the tropical stratosphere is diabatic ascent and poleward outflow. The model predicts different relationships between two long-lived tracers for the tropics and extra-tropics, provided that the photochemical sources and sinks of the two tracers have different geographic distributions. Different tropical and extra-tropical relationships have been observed for NO_y and O_3 [Murphy et al., 1993], CFCs [Volk et al., 1996], and also for N_2O and CH_4 (see Chapter 5).

Tracer studies indicate that the subtropical barrier cannot be completely impermeable. Satellite maps of O_3 and N_2O suggest that breaking planetary waves sometimes extend into the tropics, transporting material poleward [e.g., Leovy et al., 1985; Randel et al., 1993]. Furthermore, tropical tracer profiles can only be reproduced by models that have some entrainment of extra-tropical stratospheric air [Avallone and Prather, 1996; Minschwaner et al., 1996; Volk et al., 1996; Schoeberl et al., 1997; Mote et al., 1997]. Entrainment rate estimates have been limited by the accuracy and number of tropical measurements of tracers like N_2O and CH_4, particularly at altitudes above 22 km. Previous balloon measurements of N_2O and CH_4 in the tropics [e.g., Goldan et al., 1981; Bush et al., 1978] have estimated uncertainties of 10% to 25%, and satellite N_2O data from the Cryogenic Limb Array Etalon

Spectrometer (CLAES) aboard UARS [Roche et al., 1993] have roughly 20% uncertainty [Minschwaner et al., 1996]. In Chapters 3 and 5, high accuracy, high precision *in situ* measurements of long-lived tracers are used to quantify the rates of transport into and out of the tropical stratosphere.

1.5 Thesis Outline

In this thesis, we present *in situ* measurements of N_2O and CH_4 from the Aircraft Laser Infrared Absorption Spectrometer II (ALIAS II), a new instrument designed and built to measure trace gases in the lower and middle stratosphere, up to 30 km altitude. We also present *in situ* measurements of CO from ALIAS, the predecessor to ALIAS II. The author participated in most of the field measurements and calibration of both instruments during the period 1995 to present. Chapter 2 covers the ALIAS II instrument, its operation, and challenges we faced when designing a spectrometer to survive the harsh environment of the middle stratosphere. In Chapter 3, the measured distribution of atmospheric CO is described. Then, tropical stratospheric CO is compared with mid-latitude data to infer the mean time scale for isentropic transport out of the tropics. ALIAS II measurements are compared with other observations and the Caltech-JPL 2D model in Chapter 4 in order to assess the instrument accuracy and the quality of the model. In Chapter 5, we interpret the measurements of N_2O and CH_4 by ALIAS II. The functional relationship between these two trace gases is used to infer relative time scales for mixing within the tropics and within the mid-latitude "surf zone." Following this, a

tropical tracer model is compared with the observations to quantify the mean time scale for entrainment of extra-tropical air into the tropical stratosphere. Finally, the results and scientific implications of this thesis are summarized in Chapter 6.

BIBLIOGRAPHY

Allen, D. J., P. Kasibhatla, A. M. Thompson, R. B. Rood, B. G. Doddridge, K. E. Pickering, R. D. Hudson, and S.-J. Lin, Transport-induced interannual variability of carbon monoxide determined using a chemistry and transport model, *J. Geophys. Res., 101,* 28,655-69, 1996.

Andrews, D. G., J. R. Holton, and C. B. Leovy, *Middle Atmosphere Dynamics*, Academic Press, Orlando, 1987.

Avallone, L. M., and M. J. Prather, Photochemical evolution of ozone in the lower tropical stratosphere, *J. Geophys. Res., 101,* 1457-61, 1996.

Avallone, L. M., and M. J. Prather, Tracer-tracer correlations: Three-dimensional model simulations and comparisons to observations, *J. Geophys. Res., 102,* 19,233-46, 1997.

Bates, D. R., and M. Nicolet, The photochemistry of atmospheric water vapor, *J. Geophys. Res., 55,* 301-27, 1950.

Brasseur, G., and S. Solomon, *Aeronomy of the Middle Atmosphere,* 2nd. ed., D. Reidel Publishing Company, Dordrecht, Netherlands, 1986.

Brewer, A. W., Evidence for a world circulation provided by the measurements of helium and water vapor distribution in the stratosphere, *Q. J. Roy. Meteor. Soc., 75,* 351-63, 1949.

Bush, Y. A., A. L. Schmeltekopf, F. C. Fehsenfeld, and D. L. Albritton, Stratospheric Measurements of Methane at Several Latitudes, *Geophys. Res. Let., 5,* 1027-9, 1978.

CIAP (Climatic Impact Assessment Program), The natural stratosphere of 1974, Monograph 1, Report No. DOT-TST-75-51, Dept. of Transportation, Washington, D. C., 1974.

Cohen, R. C., P. O. Wennberg, R. M. Stimpfle, J. Koplow, J. G. Anderson, D. W. Fahey, E. L. Woodbridge, E. R. Keim, R. Gao, M. H. Proffitt, M. Loewenstein, and K. R. Chan, Are models of catalytic removal of O_3 by HO_x accurate? Constraints from in situ measurements of the OH to HO_2 ratio, *Geophys. Res. Let., 21,* 2539-42, 1994.

Crutzen, P. J., The influence of nitrogen oxides on the atmospheric ozone content, *Q. J. Roy. Meteor. Soc., 96,* 320-5, 1970.

DeMore, W. B., S. P. Sander, D. M. Golden, R. F. Hampson, M. J. Kurylo, C. J. Howard, A. R. Ravishankara, C. E. Kolb, and M. J. Molina, Chemical Kinetics and Photochemical Data for Use in Stratospheric Modeling, Evaluation No. 12, *JPL Publication 97-4*, 1997.

Dobson, G. M. B., Origin and distribution of the polyatomic molecules in the atmosphere, *Proc. Roy. Soc. London, A, 236,* 187-93, 1956.

Dunkerton, T. J., On the mean meridional mass motions of the stratosphere and mesosphere, *J. Atmos. Sci., 35,* 2325-33, 1978.

Goldan, P. D., W. C. Kuster, A. L. Schmeltekopf, F. C. Fehsenfeld, and D. L. Albritton, Correction of Atmospheric N_2O Mixing-Ratio Data, *J. Geophys. Res., 86,* 5385-6, 1981.

Hitchman, M. H., M. McKay, and C. R. Trepte, A climatology of stratospheric aerosol, *J. Geophys. Res., 99,* 20,689-700, 1994.

Holton, J. R., A dynamically based transport parameterization for one-dimensional photochemical models of the stratosphere, *J. Geophys. Res., 91,* 2681-6, 1986.

Hynes, A. J., P. H. Wine, and A. R. Ravishankara, Kinetics of the OH + CO Reaction Under Atmospheric Conditions, *J. Geophys. Res., 19,* 11,815-20, 1986.

IPCC (Intergovernmental Panel on Climate Change), *Climate Change: the IPCC Scientific Assessment*, Houghton, J. T., G. J. Jenkins, and J. J. Ephraums, ed., Cambridge Univ. Press, Cambridge, U. K., 1990.

Johnston, H. S., Reduction of stratospheric ozone by nitrogen oxide catalysis from SST exhaust, *Science, 173,* 517-22, 1971.

Jones, R. L., and J. A. Pyle, Observations of CH_4 and N_2O by the NIMBUS 7 SAMS: A Comparison With In Situ Data and Two-Dimensional Numerical Model Calculations, *J. Geophys. Res., 89,* 5263-79, 1984.

Junge, C. E., *Air Chemistry and Radioactivity*, Academic Press, New York, 1963a.

Junge, C. E., Studies of global exchange processes in the atmosphere by natural and artificial tracers, *J. Geophys. Res., 68,* 3849-55, 1963b.

Kellogg, W. W., Pollution of the upper atmosphere by rockets, *Space Sci. Rev., 3,* 275-316, 1964.

Ko, M. K. W., H. R. Schneider, R.-L. Shia, D. K. Weisenstein, and N.-D. Sze, A Two-Dimensional Model With Coupled Dynamics, Radiation, and Photochemistry: 1. Simulation of the Middle Atmosphere, *J. Geophys. Res., 98,* 20,429-40, 1993.

Leovy, C. B., C.-R. Sun, M. H. Hitchman, E. E. Remsberg, J. M. Russell, III, L. L. Gordley, J. C. Gille, and L.V. Lyjak, Transport of ozone in the middle stratosphere: evidence for planetary wave breaking, *J. Atmos. Sci., 42,* 230-44, 1985.

Liu, S. C., D. Kley, M. McFarland, J. D. Mahlman, and H. Levy, II, On the origin of tropospheric ozone, *J. Geophys. Res., 85,* 7546, 1980.

Logan, J. A., M. J. Prather, S. C. Wofsy, and M. B. McElroy, Tropospheric Chemistry: A Global Perspective, *J. Geophys. Res., 86,* 7210-54, 1981.

Mahlman, J. D., H. Levy, II, and W. J. Moxim, Three-dimensional simulations of stratospheric N_2O: predictions for other trace constituents, *J. Geophys. Res., 91,* 2687-707, 1986.

McElroy, M. B., R. J. Salawitch, and K. Minschwaner, The Changing Stratosphere, *Planet. Space Sci., 40,* 373-401, 1992.

McIntyre, M. E., and T. N. Palmer, Breaking planetary waves in the stratosphere, *Nature, 305,* 593-600, 1983.

Minschwaner, K., A. E. Dessler, J. W. Elkins, C. M. Volk, D. W. Fahey, M. Loewenstein, J. R. Podolske, A. E. Roche, and K. R. Chan, Bulk properties of isentropic mixing into the tropics in the lower stratosphere, *J. Geophys. Res., 101,* 9433-9, 1996.

Molina, M. J., and F. S. Rowland, Stratospheric sink for chlorofluoromethanes: Chlorine atom catalyzed destruction of ozone, *Nature, 249,* 810-4, 1974.

Mote, P. W., K. H. Rosenlof, R. S. Harwood, J. R. Holton, and J. W. Waters, Seasonal variations of water vapor in the tropical lower stratosphere, *Geophys. Res. Let., 22,* 1093-6, 1995.

Mote, P. W., K. H. Rosenlof, M. E. McIntyre, E. S. Carr, J. C. Gille, J. R. Holton, J. S. Kinnersley, H. C. Pumphrey, J. M. Russell III, and J. W. Waters, An atmospheric tape recorder: The imprint of tropical tropopause temperatures on stratospheric water vapor, *J. Geophys. Res., 101,* 3989-4006, 1996.

Mote, P. W., T. J. Dunkerton, M. E. McIntyre, E. A. Ray, and P. H. Haynes, Vertical velocity, vertical diffusion, and dilution by midlatitude air in the tropical lower stratosphere, submitted to *J. Geophys. Res.*, 1997.

Murphy, D. M., D. W. Fahey, M. H. Proffitt, S. C. Liu, K. R. Chan, E. S. Eubank, S. R. Kawa, and K. K. Kelly, Reactive Nitrogen and Its

Correlation With Ozone in the Lower Stratosphere and Upper Troposphere, *J. Geophys. Res., 98,* 8751-73, 1993.

Nevison, C. D., and E. A. Holland, A reexamination of the impact of anthropogenically fixed nitrogen on atmospheric N_2O and the stratospheric O_3 layer, *J. Geophys. Res., 101,* 6741-8, 1997.

Newell, R. E., Transfer through the tropopause and within the stratosphere, *Quart. J. Roy. Met. Soc., 89,* 167-204, 1963.

Plumb, R. A., A "tropical pipe" model of stratospheric transport, *J. Geophys. Res., 101,* 3957-72, 1996.

Plumb, R. A., and M. K. W. Ko, Interrelationships between mixing ratios of long-lived stratospheric constituents, *J. Geophys. Res., 97,* 10,145-56, 1992.

Pressman, J., and P. Warneck, The stratosphere as a chemical sink for carbon monoxide, *J. Atm. Sci., 27,* 155-63, 1970.

Randel, W. J., J. C. Gille, A. E. Roche, J. B. Kumer, J. L. Mergenthaler, J. W. Waters, E. F. Fishbein, and W. A. Lahoz, Stratospheric transport from the tropics to middle latitudes by planetary-wave mixing, *Nature, 365,* 533-5, 1993.

Reed, R. J., and K. E. German, A contribution to the problem of stratospheric diffusion by large-scale mixing, *Mon. Wea. Rev., 93,* 313-21, 1965.

Roche, A. E., J. B. Kumer, J. L. Mergenthaler, G. A. Ely, W. G. Uplinger, J. F. Potter, T. C. James, and L. W. Sterritt, The Cryogenic Limb Array Spectrometer (CLAES) on UARS: experiment description and performance, *J. Geophys. Res., 98,* 10,763-76, 1993.

Schlesinger, W. H., *Biogeochemistry: an analysis of global change*, Academic Press, San Diego, 1991.

Schoeberl, M. R., A. E. Roche, J. M. Russell III, D. Ortland, P. B. Hays, and J.W. Waters, An estimation of the dynamical isolation of the tropical lower stratosphere using UARS wind and trace gas observations of the quasi-biennial oscillation, *Geophys. Res. Let., 24,* 53-6, 1997.

Sheppard, P. A., Atmospheric tracers and the study of the general circulation of the atmosphere, *Rept. Progr. Phys., 26,* 213-67, 1963.

Shia, R.-L., Y. L. Ha, J.-S. Wen, and Y. L. Yung, Two-Dimensional Atmospheric Transport and Chemistry Model: Numerical Experiments With a New Advection Algorithm, *J. Geophys. Res., 95,* 7467-83, 1990.

Solomon, S., J. T. Kiehl, R. R. Garcia, and W. Grose, Tracer Transport by the Diabatic Circulation Deduced from Satellite Observations, *J. Atmos. Sci., 43,* 1603-17, 1986.

Stolarski, R. S., S. L. Baughcum, W. H. Brune, A. R. Douglass, D. W. Fahey, R. R. Friedl, S. C. Liu, R. A. Plumb, L. R. Poole, H. L. Wesoky, and D. R. Worsnop, 1995 Scientific Assessment of the Atmospheric Effects of Stratospheric Aircraft, *NASA Reference Publ. 1381*, 1995.

Summers, M. E., D. E. Siskind, J. T. Bacmeister, R. R. Conway, S. E. Zasadil, and D. F. Strobel, Seasonal variation of middle atmospheric CH_4 and H_2O with a new chemical dynamical model, *J. Geophys. Res., 102,* 3503-26, 1997.

Trepte, C. R., and M. H. Hitchman, Tropical stratospheric circulation deduced from satellite aerosol data, *Nature, 355,* 626-8, 1992.

Tuck, A. F., et al., The Brewer-Dobson circulation in the light of high altitude *in situ* aircraft observations, *Quart. J. Roy. Met. Soc., 123,* 1-69, 1997.

Tung, K. K., On the Two-Dimensional Transport of Stratospheric Trace Gases in Isentropic Coordinates, *J. Atmos. Sci., 39,* 2330-55, 1982.

Volk, C. M., J. W. Elkins, D. W. Fahey, R. J. Salawitch, G. S. Dutton, J. M. Gilligan, M. H. Proffit, M. Loewenstein, J. R. Podolske, K. Minschwaner, J. J. Margitan, and K. R. Chan, Quantifying transport between the tropical and mid-latitude lower stratosphere, *Science, 272,* 1763-8, 1996.

Waugh, D. W., Subtropical stratospheric mixing linked to disturbances in the polar vortices, *Nature, 365,* 535-7, 1993.

Wennberg, P. O., et al., Removal of stratospheric O_3 by radicals: *In situ* measurements of OH, HO_2, NO, NO_2, ClO, and BrO, *Science, 266,* 398-404, 1994.

WMO (World Meteorological Organization), Global Ozone Research and Monitoring Project - Report No. 37, *Scientific Assessment of Ozone Depletion: 1994*, WMO, Geneva, Switzerland, 1995.

Yang, H., E. Olaguer, and K. K. Tung, Simulation of the Present-Day Atmospheric Ozone, Odd Nitrogen, Chlorine and Other Species Using a Coupled 2-D Model in Isentropic Coordinates, *J. Atmos. Sci., 48,* 442-71, 1991.

Chapter 2

Instrument Description

2.1 Introduction

The Aircraft Laser Infrared Absorption Spectrometer II (ALIAS II) is a lightweight, compact, high resolution (0.0003 cm^{-1}), scanning, mid-infrared absorption spectrometer. It was designed and built by the author in collaboration with the Atmospheric Laser Spectroscopy Group of the Jet Propulsion Laboratory (JPL) to make *in situ* measurements of chemical species from the upper troposphere to 30 km altitude in the middle stratosphere. The incentive for building this particular instrument is the need for high accuracy, high resolution measurements of chemical tracers in the stratosphere above the 21 km cruising altitude of the NASA ER-2 stratospheric research aircraft. The instrument was originally designed to fly on Perseus-A, a new, high-altitude, unmanned aircraft built for NASA by Aurora Flight Sciences [Monastersky, 1991]. However, aircraft development difficulties required us to reconfigure the instrument for a payload lofted by a helium balloon. In this configuration, ALIAS II has made six successful flights from three different locations (New Mexico, Alaska, and Brazil) with an estimated accuracy of 5% relative to calibration standards from the National Oceanic and Atmospheric

Administration (NOAA) Climate Monitoring and Diagnostics Laboratory (CMDL).

ALIAS II is a two-channel, miniaturized version of ALIAS, the four-channel infrared spectrometer built six years ago by the Atmospheric Laser Spectroscopy Group to fly on the ER-2 aircraft [Webster et al., 1994]. Diagrams of ALIAS and ALIAS II are shown in Figures 1a and 1b-e, respectively. ALIAS II is more compact than its predecessor is and features an open-path sample cell (an optical cell that is open to the atmosphere and does not require air to be pumped through it). With this design, we minimize payload mass, volume, and any possible contamination effects from wall reactions. The spectroscopic technique, lasers, detectors, electronics, flight software, and data processing software are nearly the same as for ALIAS. Both ALIAS and ALIAS II use second-harmonic spectroscopy to detect absorptions as small as 1 part in 10^5 over a 3-sec integration period, corresponding to sensitivities in the sub-ppb range [Webster et al., 1994; May and Webster, 1993]. The measurement technique is described in detail below in the Spectroscopic Theory section of this thesis. Each channel uses a lead-salt tunable diode laser (TDL) and InSb photovoltaic detector to measure the concentrations of chemical species by absorption of infrared radiation. The TDLs are scanned across narrow spectral intervals (typically 1 cm^{-1}) at a 10-Hz repetition rate with a superimposed, small-amplitude modulation frequency (12 or 14 kHz). Thirty spectral scans are averaged together to yield the 3-sec integration time. To achieve greater infrared absorption, the laser beams are reflected multiple times between the end mirrors of the sample cell in a

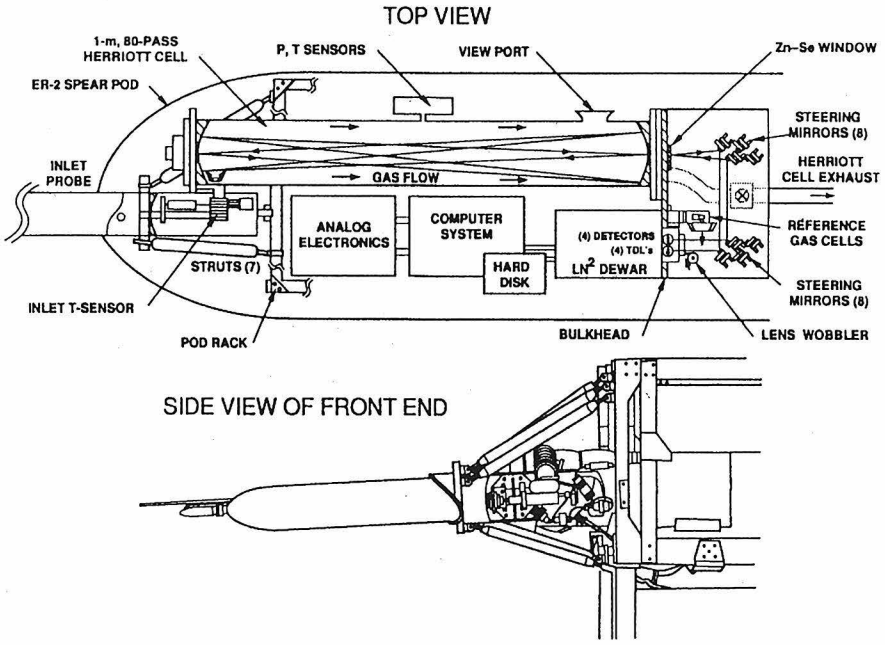

Figure 1a. Diagram of ALIAS, shown in the right spear pod of the ER-2 aircraft.

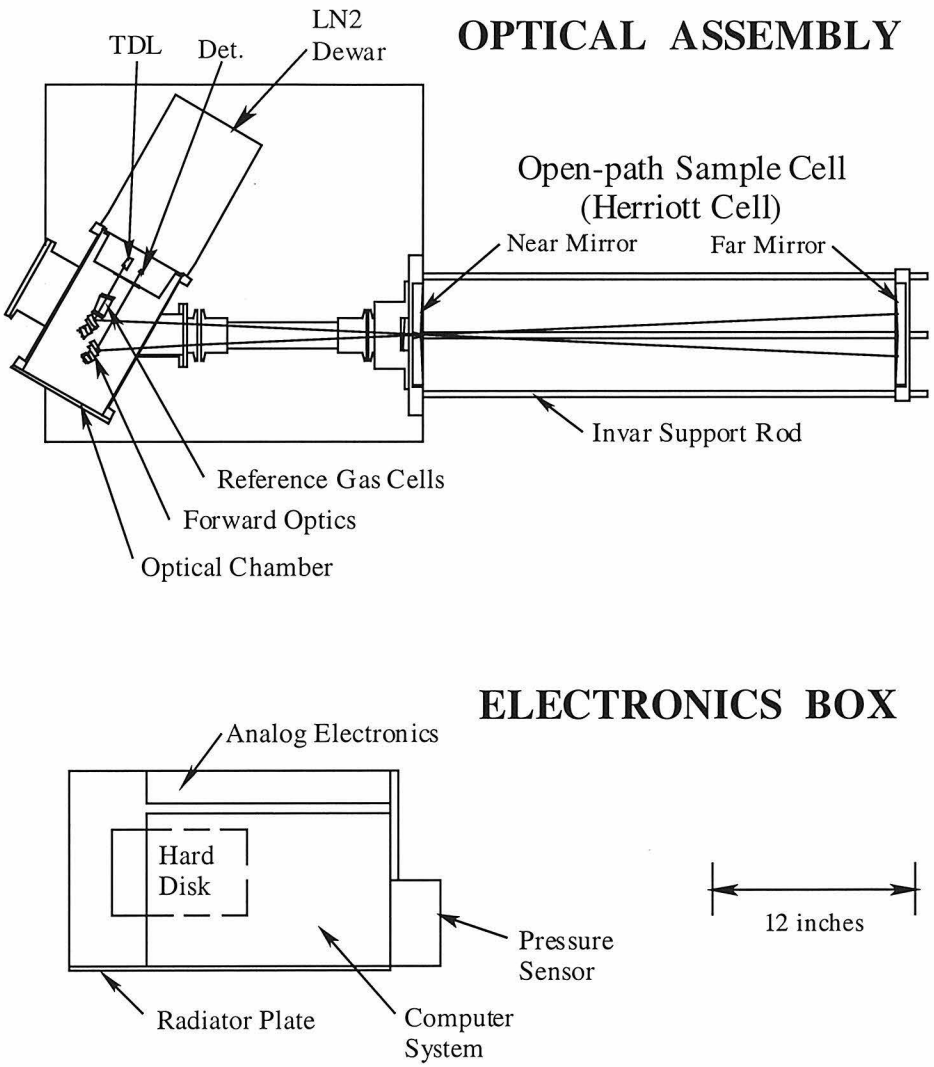

Figure 1b. Diagram of ALIAS II (top view). The optical assembly and electronics box are mounted separately inside the balloon gondola.

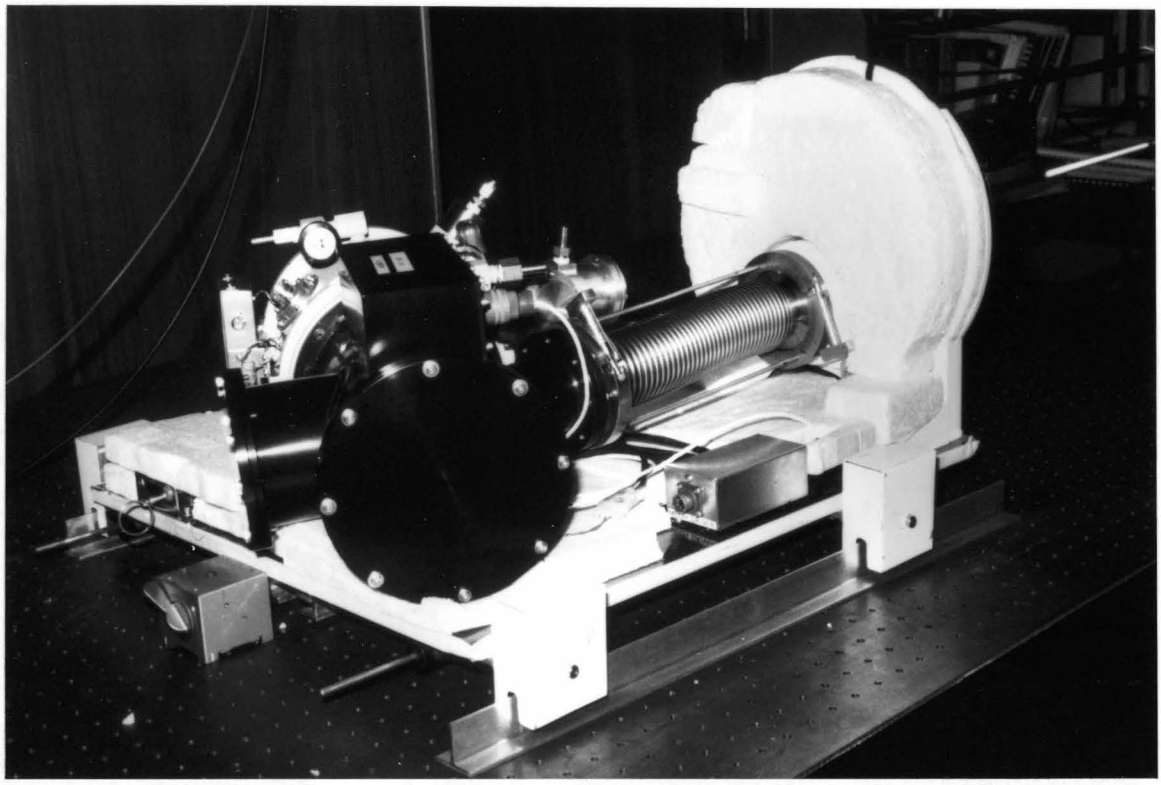

Figure 1c. Photograph of ALIAS II (side view).

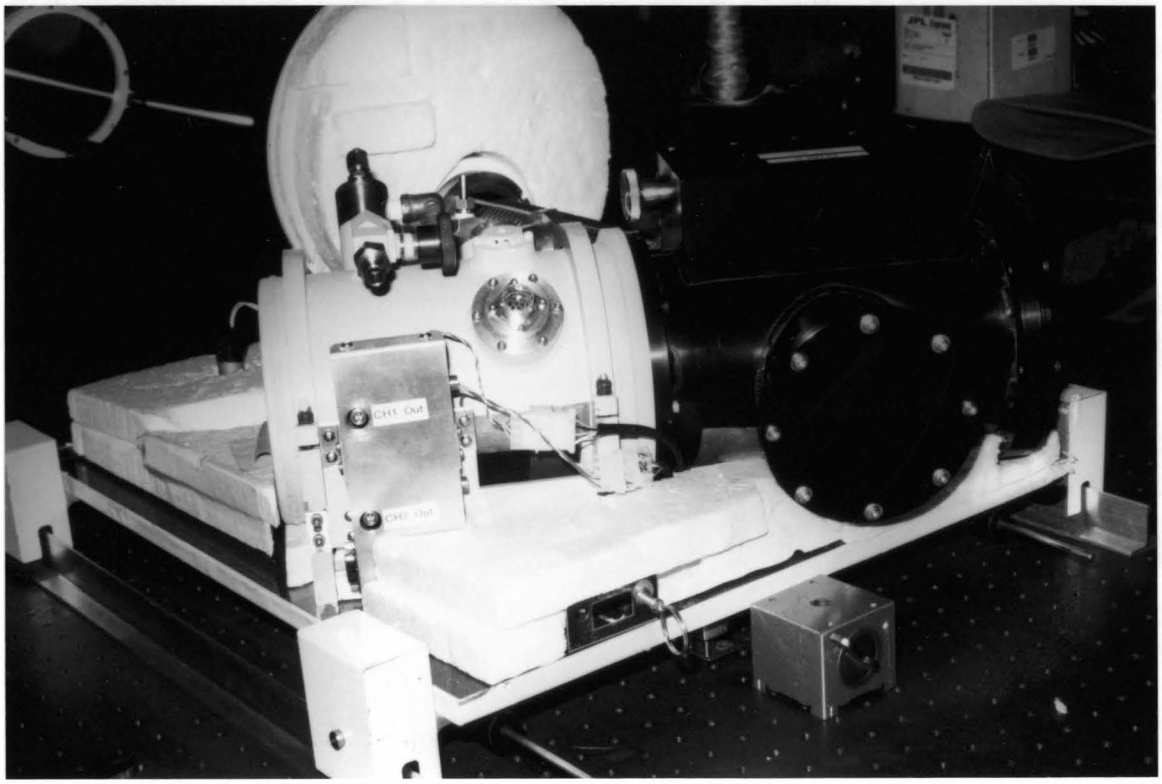

Figure 1d. Photograph of ALIAS II (side view).

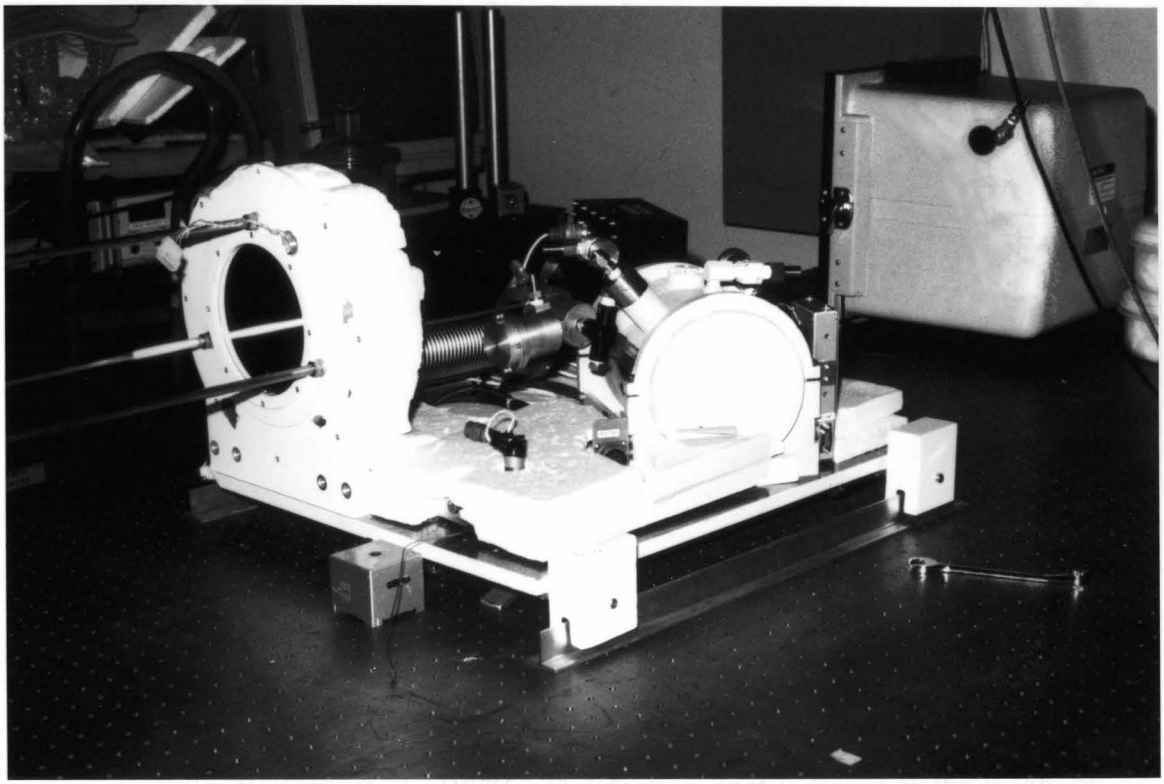

Figure 1e. Photograph of ALIAS II (side view).

Herriott cell configuration [Herriott et al., 1964]. With InSb detectors, both instruments can measure any atmospheric gases that have strong infrared absorptions between wavelengths of 3 and 5 μm and stratospheric volume mixing ratios of at least 1 ppb. These gases include N_2O, CH_4, CO, H_2O, and HCl. If HgCdTe photoconductive detectors are used instead, then the instruments can operate within the wider 3 to 16 μm wavelength range, and additional gases such as NO_2 or HNO_3 can be measured. The following sections cover the spectroscopic theory, mechanical design, optical design, data acquisition, data processing, instrument calibration, and accuracy and precision of ALIAS II. The discussion covers details essential to a thorough understanding of instrument operation, highlighting unique features of ALIAS II. At the end of the chapter is a set of suggestions for future improvements to the instrument.

2.2 Spectroscopic Theory

ALIAS and ALIAS II utilize mid-infrared second-harmonic spectroscopy, a well-developed technique for detection of trace gases [Schiff et al., 1994; Webster et al., 1988]. This section briefly describes the theory of harmonic spectroscopy, which was reviewed by Webster et al. [1988]. Consider electromagnetic radiation propagating along the z direction. The attenuation of the radiation by absorption is directly proportional to the irradiance I and the concentration of absorbers n:

$$dI = -\kappa(\bar{\nu})nIdz \tag{2.1}$$

where κ is the absorption coefficient. By integrating equation (2.1), we get the famous Beer-Lambert Law

$$I(\bar{\nu}, z) = I_0 \exp\left[-\kappa(\bar{\nu})nz\right] \tag{2.2}$$

which states that irradiance decays exponentially as the radiation passes through an absorbing medium.

In the mid-infrared region of the electromagnetic spectrum, molecules absorb photons at discrete wavelengths corresponding to the spacing between quantized vibrational-rotational energy levels. The spacing between vibrational energy levels (~10^3 cm^{-1}) is much larger than the spacing between rotational levels (~1 cm^{-1}), so vibrational absorption bands consist of discrete lines corresponding to transitions between different rotational levels of the upper and lower vibrational levels. Quantum mechanical selection rules allow transitions from the ground vibrational state to an excited state if the molecular dipole moment changes. If the vibrational angular momentum does not change, then rotational transitions of $\Delta J = \pm 1$ are allowed to accompany vibrational transitions (Figure 2). ALIAS II measures both N_2O and CH_4 in P-branches ($\Delta J = -1$) of the ν_3 fundamental stretching mode. N_2O is measured at 2207 cm^{-1} at the P(18) vibrational-rotational line and CH_4 is measured at 2948 cm^{-1} in a quartet of P(7) lines (see Figure 3 for CH_4 spectra).

Infrared absorption lines have a finite width of frequency due to Doppler and pressure broadening and an intrinsic laser linewidth. Doppler broadening

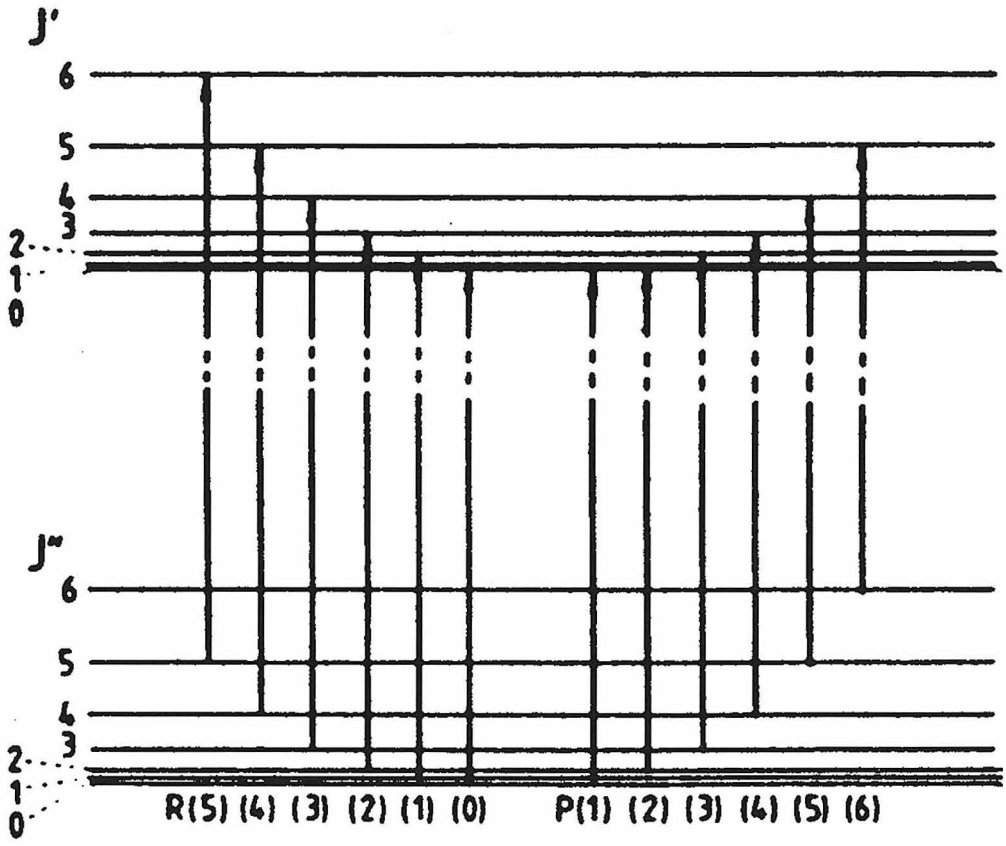

Figure 2. Energy level diagram for vibrational-rotational transitions. J' is the upper state rotational energy level and J" is the lower state rotational energy level. The R-branch has $\Delta J = +1$ and the P-branch has $\Delta J = -1$.

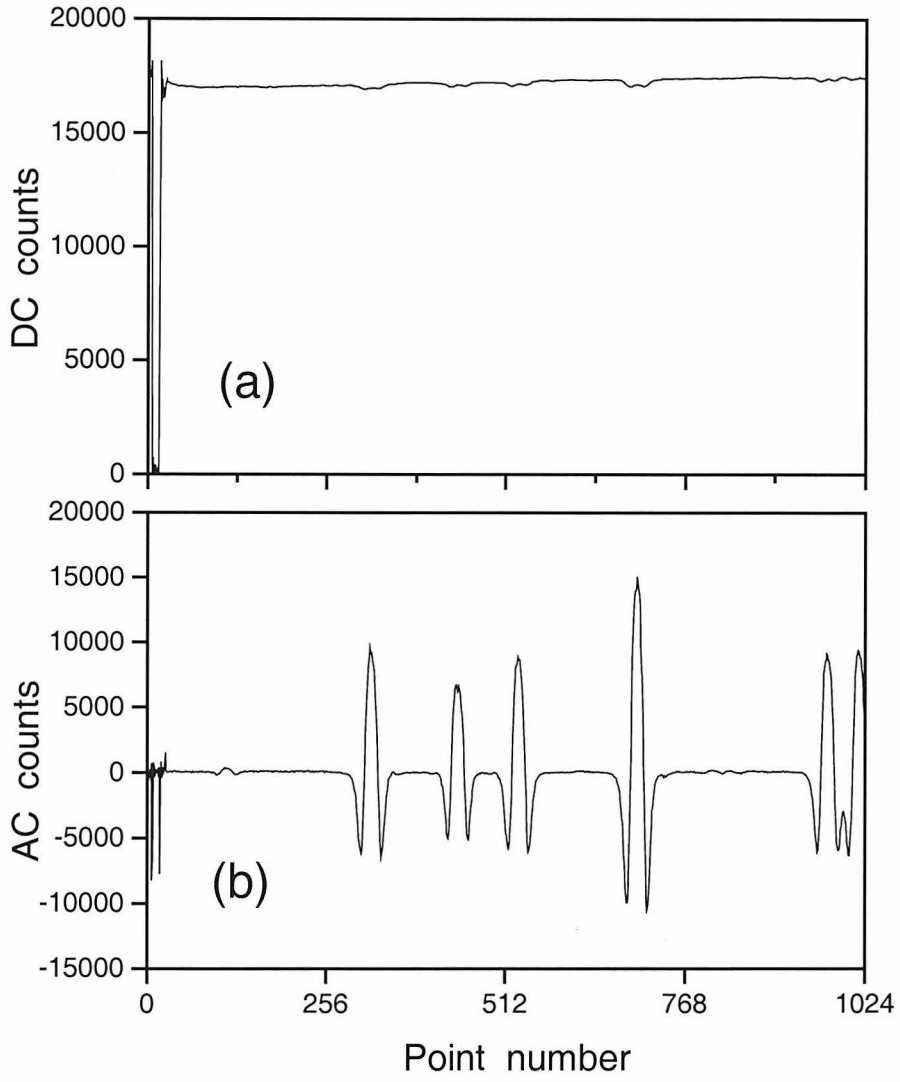

Figure 3. CH_4 spectra recorded by ALIAS II at 43 hPa during the balloon flight of 960921 (yymmdd format): (a) raw TDL power (counts) measured on the DC channel, (b) the corresponding raw 2f spectrum (counts) measured on the AC channel. These spectra are 3-sec averages of ten scans.

is caused by a Doppler shift in the frequency of photons absorbed by molecules in motion. For molecules moving with speed v_z away from the photon source, the actual frequency absorbed by the molecule is

$$\overline{\nu} = \overline{\nu}_0\left(1 - v_z/c\right) \tag{2.3}$$

where c is the speed of light. The Maxwell-Boltzmann distribution of molecular speeds is Gaussian, so by the proportionality in equation 2.3, the Doppler-broadened absorption line has a Gaussian lineshape. From Webster et al. [1988], the normalized shape function of a Doppler-broadened line is given by

$$g_D\left(\overline{\nu} - \overline{\nu}_0\right) = \left(1/\gamma_D\right)\left(\ln 2/\pi\right)^{1/2} \exp\left[-\left(\overline{\nu} - \overline{\nu}_0\right)^2 \ln 2/\gamma_D{}^2\right] \tag{2.4}$$

The half-width at half-maximum (HWHM) is the Doppler linewidth

$$\gamma_D = \left(\overline{\nu}_0/c\right)\left(2kT \ln 2/m\right)^{1/2} \tag{2.5}$$

where k is Boltzmann's constant, T is temperature, and m is molecular mass. For typical mid-infrared absorption lines, $\gamma_D \approx 60$ MHz ($2\text{x}10^{-3}$ cm^{-1}). This is much larger than natural (or radiative) line broadening in the mid-infrared (~10 kHz), but comparable to the laser linewidth. Laser linewidths of the TDLs used in ALIAS II have been experimentally measured to ±5% (1 st. dev.) using pure gases at low pressure (<1 hPa). The direct absorption spectra are well-approximated by Gaussian lineshapes with HWHM ≈ 80 MHz. The laser

linewidth must be convolved with the spectral linewidth, as described below in the Instrument Calibration section.

Pressure broadening occurs if the frequency of molecular collisions is high enough to perturb molecular energy levels. At pressures of several hundred hPa, the broadened lineshape is well-approximated by the Lorentzian shape function [Webster et al., 1988]:

$$g_L(\overline{\nu} - \overline{\nu}_0) = (\gamma_L/\pi)\Big/\left[(\overline{\nu} - \overline{\nu}_0)^2 + \gamma_L^2\right] \tag{2.6}$$

where the linewidth γ_L is a function of pressure and temperature:

$$\gamma_L(P,T) = \gamma_L^0(P/P_0)(T_0/T)^s \tag{2.7}$$

and the exponent *s* of the temperature dependence is empirically found to be approximately 0.75. The accuracy of this value is unknown for the extreme range of temperatures encountered in the stratosphere. The spectroscopic parameters used in this study are listed in Table 1 below.

Throughout the entire troposphere and lower stratosphere, the mid-infrared absorption lineshapes are intermediate between Gaussian and Lorentzian shapes. These lineshapes are described mathematically by the Voigt profile. A molecule in motion has linecenter absorption at the Doppler-shifted wavenumber $\overline{\nu}^* \neq \overline{\nu}_0$ (see equation 2.3). Pressure broadening creates a Lorentzian distribution of absorbed frequencies centered around $\overline{\nu}^*$ (see equation 2.6). However, there is a Gaussian distribution of molecular speeds,

	N_2O	CH_4	CH_4	CH_4	CH_4	accuracy
linecenter wavenumber (cm^{-1})	2207.6204	2947.66785	2947.81081	2947.91211	2948.10781	<0.0010
intensity S (cm^{-1}/molecule cm^2)	9.10E-19	5.20E-20	3.40E-20	5.10E-20	8.50E-20	1-2%
transition probability^2 (Debye^2)	2.993E-02	2.328E-03	4.642E-03	2.309E-03	2.303E-03	unknown
air-broadened halfwidth (cm^{-1}/atm)	0.0757	0.0571	0.0485	0.0632	0.0599	CH4: 2-3% N2O: 5-10%
self-broadened halfwidth (cm^{-1}/atm)	0.0000	0.0760	0.0680	0.0840	0.0820	CH4: 2-3%
lower state energy E" (cm^{-1})	143.2811	293.1784	293.1699	293.1643	293.1540	unknown
temperature dependence s	0.76	0.75	0.75	0.75	0.75	unknown
v (upper), nu3 fundamental	1	1	1	1	1	
v (lower)	0	0	0	0	0	
J' (upper)	17	6	6	6	6	
J" (lower)	18	7	7	7	7	
point group (upper)		F2	E	F1	A1	
point group (lower)		F1	E	F2	A2	

Table 1. Spectral parameters for the N_2O and CH_4 vibrational-rotational lines used by ALIAS II.

so the actual spectral absorption profile is a convolution of Gaussian and Lorentzian distributions [Webster et al., 1988]:

$$g_V(\overline{\nu}) = \int_{-\infty}^{+\infty} g_D(\overline{\nu}^* - \overline{\nu}_0) g_L(\overline{\nu} - \overline{\nu}^*) d\overline{\nu}^* \tag{2.8}$$

which is equivalent to:

$$g_V(\overline{\nu}) = \sqrt{\ln 2/\pi}(1/\gamma_D)\int_{-\infty}^{+\infty}\left\{ye^{-t^2}\Big/\left[y^2 + (x-t)^2\right]\pi\right\}dt \tag{2.9}$$

The integrand in equation 2.9 is called the Voigt function, which we evaluate numerically by Humlicek's method [May and Webster, 1993; Humlicek, 1982].

In the stratosphere, trace gases have relatively low concentrations and thus weak linecenter absorptions. To increase instrument sensitivity, a high frequency modulation (f = 12 or 14 kHz) is applied to the laser current ramp and the amplified, filtered signal from the detectors is analyzed by second-harmonic spectroscopy. Consider a laser scanning over an absorption line with linecenter frequency $\overline{\nu}_0$ and superimpose a sinusoidal modulation onto the sawtooth pattern of the laser current. For a small-amplitude modulation, the laser frequency will be directly proportional to the applied current and will also be sinusoidal:

$$\overline{\nu}(\mathrm{t}) = \overline{\nu}_0 + \overline{\nu}_{scan} + a\cos(2\pi \mathrm{ft}) \tag{2.10}$$

where a is the half-amplitude of the modulation. The time-varying signal can be detected at frequency 2f and filtered by a narrow band-pass filter to eliminate background. This signal is given by the second Fourier component of the Fourier series of $\bar{v}(t)$ [May and Webster, 1993]:

$$H_2 = C\int_0^{\pi} g\cos(2\theta)d\theta \tag{2.11}$$

where g is the absorption lineshape and C is a constant. Figure 3 shows typical modulated direct and 2f harmonic spectra for the 2948 cm^{-1} CH_4 group. Note the amplification of the 2f spectrum relative to the direct absorption spectrum. Webster et al. [1988] gives analytical expressions for H_2 in the cases of Doppler-broadened lineshapes, pressure-broadened lineshapes, and Voigt lineshapes.

Using synthetic spectra generated from the HITRAN database [Rothman et al., 1992], the expected 2f signal size $H_2(calc)$ is calculated for a given pressure, temperature, and mixing ratio $\chi(calc)$. A FORTRAN computer program developed by R. D. May generates a matrix of $H_2(calc)$ for the range of pressures and temperatures expected during flight. On the balloon, pressures and temperatures range from 5 to 500 hPa and 180 to 300 K, respectively. We do not reduce data for pressures greater than 500 hPa because of low sensitivity due to large pressure broadened linewidths. With the data processing software [May and Webster, 1993], a polynomial filter is applied to the 1024-point 2f spectra and the peak-to-peak 2f signal size y is measured.

This signal is converted from raw counts to spectroscopic units by the following expression [May and Webster, 1993]:

$$H_2(obs) = y\left(\frac{1}{RP'}\right)\left(\frac{DC_g}{AC_g}\right) \tag{2.12}$$

where R is the response number of the instrument obtained from calibration (see the Instrument Calibration section), P' is the return laser power, DC_g is the laser power gain (1 to 128), and AC_g is the 2f amplifier gain (1 to 4096). The observed volume mixing ratio $\chi(obs)$ is then given by:

$$\chi(obs) = \frac{H_2(obs)}{H_2(calc)}\chi(calc) \tag{2.13}$$

because for small absorptions, χ is proportional to H_2.

2.3 Mechanical Design

There were many challenges to meet in the mechanical design of ALIAS II. The instrument had to be lightweight enough to allow flights to high altitudes, but rugged enough to withstand rough landings; insulated and heated sufficiently to operate over a large temperature range, but equipped with a radiator panel and reflective surfaces to prevent overheating. This section describes our solutions to these and other engineering problems.

We minimized the mass and volume of ALIAS II because these physical properties become critical at higher altitudes. On the Perseus-A unmanned aircraft, mass reductions meant the aircraft could attain higher altitudes. On the balloon payload, mass and volume reductions allowed us to use a smaller gondola and a considerably smaller balloon volume. Both factors increased the likelihood that meteorological conditions (mainly wind shear and velocity) would be acceptable for a balloon launch and greatly simplified the launch. Using an open-path cell helped us reduce the mass of the instrument: the sample cell consists simply of two mounted mirrors (15.24 cm diameter) separated by three 75 cm invar spacing rods (Figure 1b). In contrast, a closed sample cell would be much heavier because it would require an inlet tube, electric pump, and airtight chamber. Most structural members of the instrument are made of aluminum to be lightweight. The liquid nitrogen Dewar was designed by the author and engineers from Kadel Corporation to be especially lightweight. It is composed of aluminum and G10 fiberglass. The main structural mounting plates of the instrument are Hexcell® aircraft aluminum honeycomb, a remarkably lightweight yet strong material.

Balloon payloads have to withstand large decelerations during parachute deployment and landings, so there are stringent requirements on the mechanical strength of ALIAS II: the instrument must be able to withstand decelerations of 10g vertically, or 5g at 45° off-axis, where g is the acceleration of gravity. We chose a safety factor of 2.5 to ensure the survival of the instrument. With the help of R. L. Norton at JPL, we designed support beams and brackets that met these requirements. Aluminum and aluminum

honeycomb were chosen for the support structures because they are both strong and lightweight. The only dense materials used were the invar support rods of the open-path cell, chosen for low thermal expansion (see the Optical Design section).

During flight, most of the instrument is maintained at temperatures close to 25°C by regulated electrical strip heaters (Minco, Incorporated), 2.54 cm-thick styrofoam, and Nomex® aramid fiber cloth insulation. Although more heaters could have been added to stabilize temperatures further, the additional mass due to extra batteries was prohibitive. The most important components to keep warm are the optics (see the Optical Design section) and the hard disk, which is operationally rated down to only 0°C. Most heat loss occurs when the balloon passes through the tropopause region (pressure ≈ 100 hPa) due to extremely low temperatures and efficient conductive heat loss. Exposed parts of the instrument and critical optical supports are kept warm by heaters, but given the limited availability of battery power, the key to thermal stability is insulation.

At 30 km altitude (10 hPa), the instrument has a tendency to overheat because the dominant heat loss mechanism is radiation, not conduction. At this altitude, a 298 K blackbody fully illuminated by the Sun absorbs about 1365 W/m^2 but emits only about 450 W/m^2. In the absence of conduction or convection, the blackbody would become hot. To minimize absorption of solar radiation, instrument reflectivity is increased by encasing parts in white styrofoam or aluminum painted white. Heat-generating electronic components are sandwiched between layers of thermally conductive foam in physical

contact with an aluminum radiator panel. The radiator panel is recessed inside the gondola to shade it from the Sun. Figure 4 shows ambient pressure, ambient temperature, and temperatures of various parts of the instrument recorded during a balloon flight. Despite ambient temperatures as low as approximately -60°C on this flight, the components remained in the temperature range of -5°C to 30°C.

Two subsystems of ALIAS II contain moving parts. The first is the reference cell mechanism similar to the one found in ALIAS [Webster et al., 1994]. The second one is the optical return mechanism: the entire optical assembly, including the Dewar, forward optics, reference cells, and open-path sample cell, is mounted on a track and spring-loaded to be pulled back inside the gondola. Figure 5 shows the instrument in both deployed and stowed positions. The optical assembly is deployed prior to launch so that the sample cell is entirely outside the gondola structure during data collection, minimizing contamination effects. The mechanism stows the optical assembly inside the gondola near the end of the balloon flight to protect the instrument from sudden decelerations. A linear solenoid, controlled from the ground by telemetry, is activated to release a cable holding the optical assembly. Immediately, a constant-force spring pulls the assembly inside the gondola, two coil springs slow it down, and a latch engages to keep it safely inside the gondola.

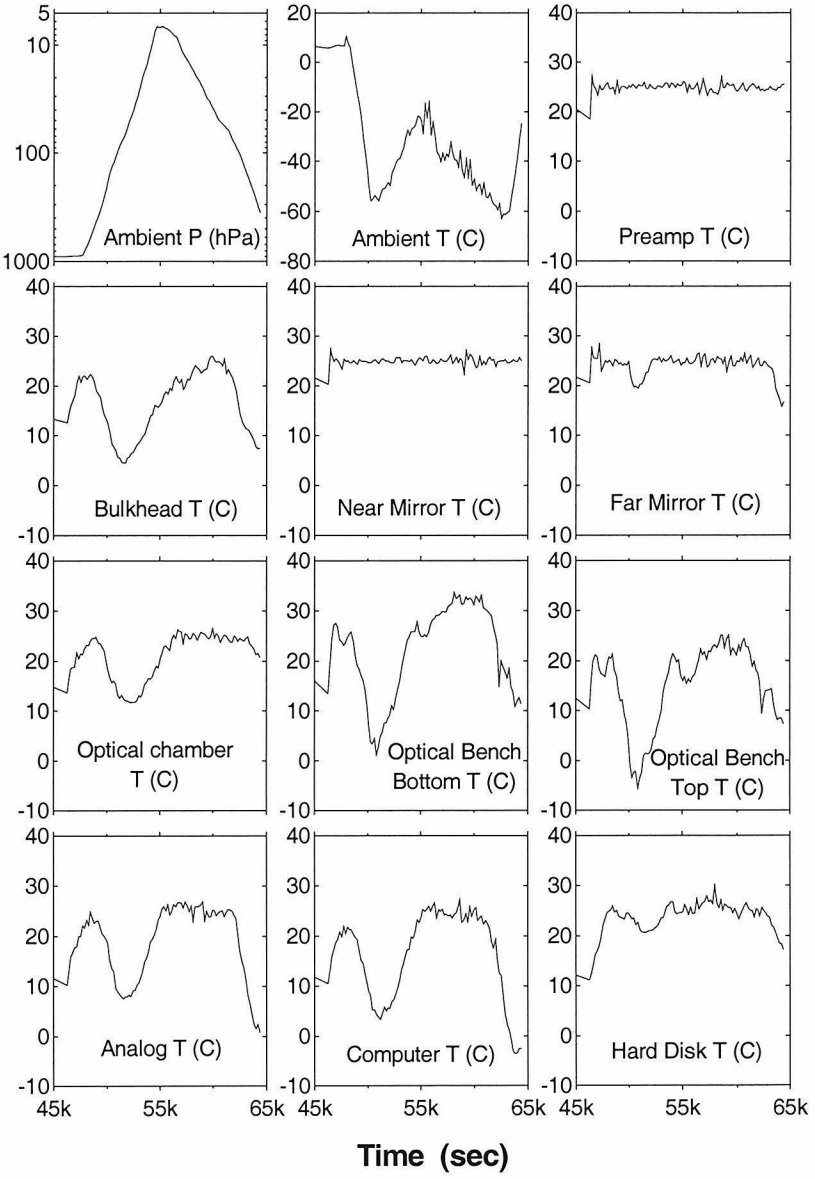

Figure 4. Ambient pressure (hPa), ambient temperature (°C), and engineering temperatures (°C) recorded by ALIAS II during the 960921 balloon flight.

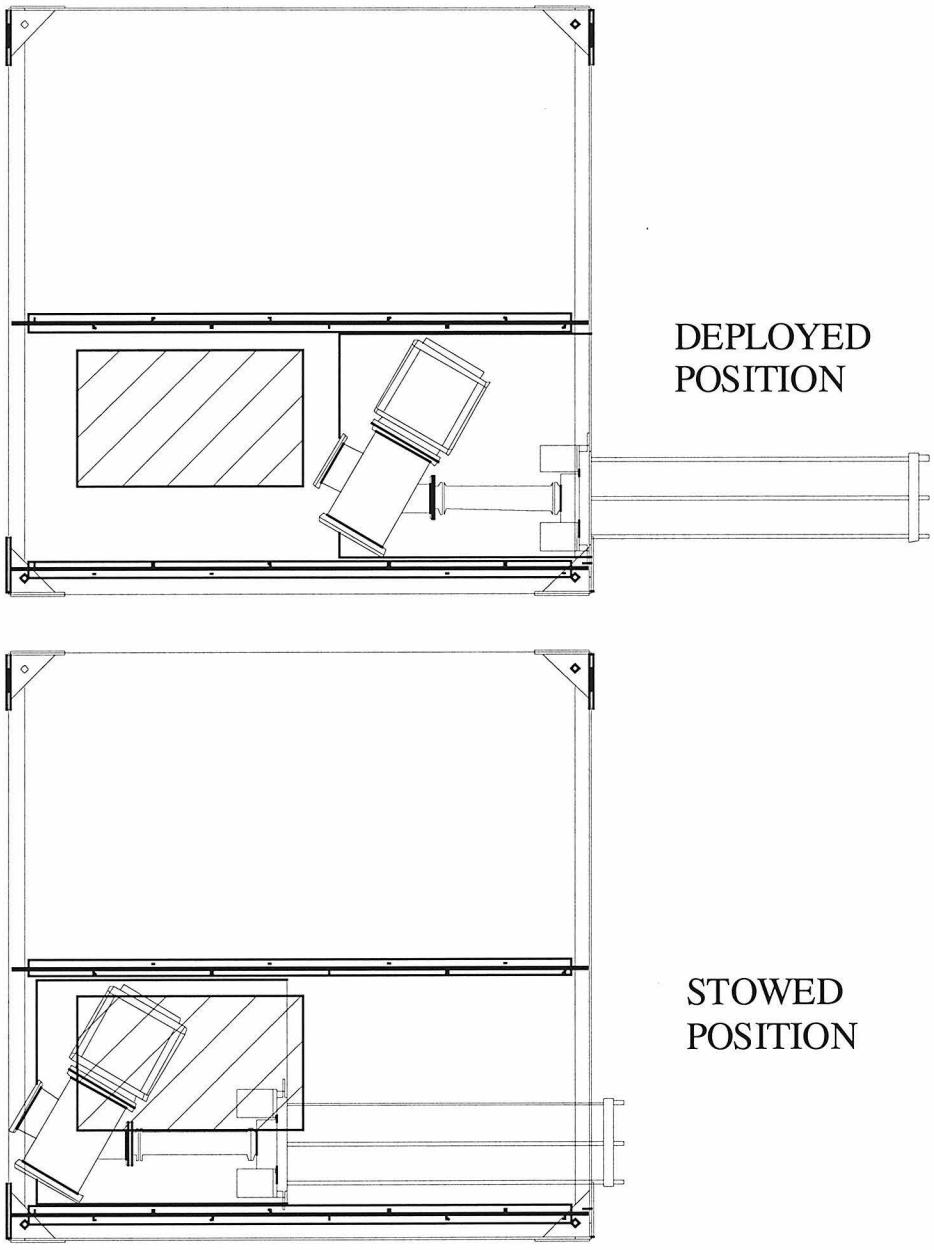

Figure 5. Top view of ALIAS II in the balloon gondola, with the optical assembly shown in both deployed and stowed positions. The hatched area is the ALIAS II electronics, which are mounted above the optical assembly.

2.4 Optical Design

The ALIAS II optical layout was designed by the author to fit into a smaller volume than ALIAS, to seal the forward optics inside a purged chamber, and to expose the open-path sample cell to ambient air flow (see Figure 5). This design was originally driven by an interest in measuring stratospheric H_2O [Webster et al., 1994], which has a volume mixing ratio of only 2 to 7 parts per million and is very easily contaminated by instrument outgassing. For this series of balloon flights, we did not measure H_2O, but the purged optical chamber was still useful in preventing contamination because the N_2O volume mixing ratio at 30 km is typically only 25% of its tropospheric value. The ALIAS II instrument has three optical subsystems: a liquid nitrogen Dewar containing lasers, detectors, and the cold shield; a purged optical chamber containing windows, lenses, steering mirrors, and reference gas cells; and the exposed sample cell with its near and far mirrors. Figure 6 shows a ray trace through the optical system.

Inside the liquid nitrogen Dewar, two lasers and two detectors are mounted on an oxygen-free, high thermal conductivity, copper cold finger. Indium gaskets increase the thermal conductivity between the cold finger and the electronic components. Since the cold finger is in direct contact with a 2-liter reservoir of liquid nitrogen, its temperature is close to the liquid nitrogen boiling point (77 K). Minor temperature adjustment on the TDLs is achieved by heaters mounted on the laser packages. Temperature stability is maintained by two absolute pressure relief valves (Tavco Corporation) mounted in series on the gas venting valve of the Dewar [Webster et al., 1994]. The adjustable

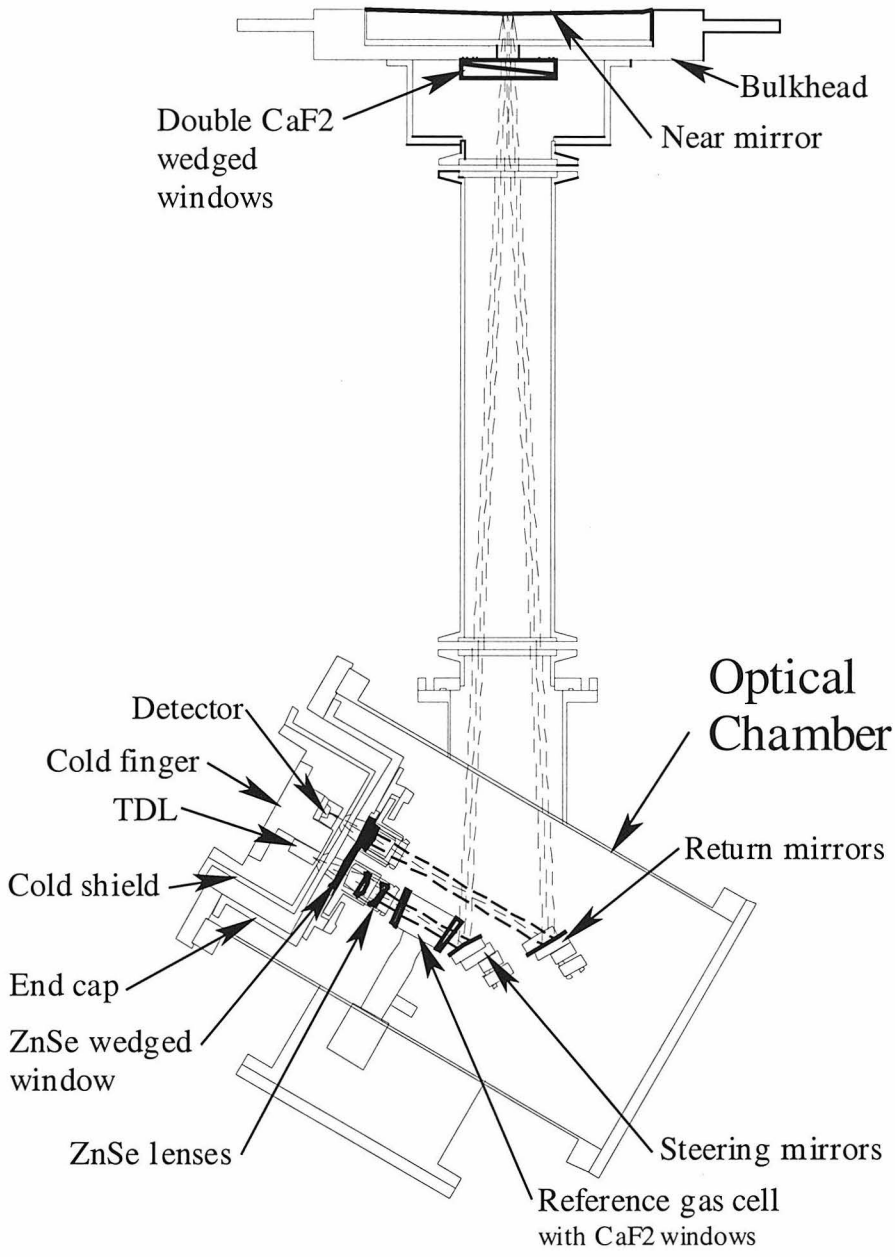

Figure 6. Optical ray trace through ALIAS II. Infrared laser beams are shown as dashed lines. Optical components such as windows, lenses, and mirrors are outlined with thick lines.

relief valves maintain the gas pressure above the liquid nitrogen bath at approximately 18 p.s.i. absolute pressure (1220 hPa) regardless of the atmospheric pressure outside the Dewar. The TDL temperature is not controlled actively by the instrument, but has been verified to be adequately stable throughout a balloon flight. On ALIAS (the aircraft instrument), the biggest causes of temperature shifts are sloshing of the liquid nitrogen during aircraft ascents and descents and low cryogen level near the end of the flight. On ALIAS II, the balloon flight is usually so gentle and short in duration (6 hours) that neither effect is important. The temperatures of the TDLs are monitored by silicon cryodiode sensors mounted on the laser packages. The liquid nitrogen hold time of the ALIAS II Dewar is greater than 26 hours (with no heat load). Thermal radiation inside the Dewar is reduced by a highly reflective, polished aluminum cold shield and multiple layers of insulated, reflective, aluminized mylar. An activated charcoal getter absorbs volatiles to further improve the hold time. Even with a typical heat load (3.7 W), the hold time is at least 14 hours.

The source of mid-infrared radiation for each channel is a lead-salt, semiconductor, tunable diode laser (TDL) custom manufactured by Laser Photonics, Incorporated, to lase at desired frequencies. As mentioned above, the channel 1 TDL lases at 2207 cm^{-1} and the channel 2 TDL lases at 2948 cm^{-1}. These TDLs emit hundreds of μW of power when biased by a small current (hundreds of mA). They have narrow laser linewidths (tens of MHz), have greater than 97% purity of frequency mode at low current, and scan continuously across 2 cm^{-1} when the current is changed by approximately 30

mA. These features are nearly ideal for second-harmonic infrared spectroscopy of low-pressure gas mixtures. Unfortunately, these lasers have disadvantages too: they operate only at temperatures below 100 K, are extremely sensitive to temperature changes, are destroyed by reverse current bias, have poor spatial mode quality (roughly elliptical with several intensity maxima), have beam divergences of 10 to 30 degrees, and change their spectral properties when thermally recycled.

As shown in Figure 6, the divergent laser beams pass through apertures in the cold shield and end cap before entering the optical chamber. The size of these apertures is a tradeoff: small apertures reduce the amount of background radiation that enters the Dewar, but large apertures reduce backreflections. After passing through the sample cell, the laser beams return to the Dewar through similar apertures in the end cap and cold shield. The 2 mm by 2 mm InSb photovoltaic detectors (EG&G Judson) are housed inside black-anodized boxes with 3.2 mm diameter apertures to further reduce the amount of background radiation that reaches the detectors.

The optical chamber is a welded, vacuum-tight, aluminum structure connected to the Dewar and sample cell by o-ring flanges. It is evacuated to prevent infrared absorption in the optical path between the Dewar and the sample cell. Mechanical strain caused by differential pressure on the optical chamber can affect the optical alignment, so the chamber is backfilled with approximately 500 hPa ultrahigh purity nitrogen gas. The laser beams enter the optical chamber through a rectangular, wedged ZnSe window epoxied to the Dewar end cap. The divergent laser beams are then collimated by broadband,

antireflection-coated, 12.7 mm diameter, 25.4 mm focal length ZnSe positive meniscus lenses, as shown in Figure 6. There is one steering mirror per channel to inject the beam into the sample cell, and one return mirror per channel to collect the return beam. This optical design was chosen to minimize instrument volume, but required careful machining of parts (±0.003 in. tolerance) to ensure that the instrument optics could be aligned. At the bulkhead, the laser beams are injected into the Herriott cell through a pair of 50.8 mm diameter, wedged CaF_2 windows. These windows isolate the purged forward optics from the atmosphere. After passing multiple times through the sample cell, the return beams are focused onto the detectors with lenses identical to the laser collimation lenses.

Within the ALIAS II sample cell, the two infrared beams are reflected 86 times between a pair of Au-Cr coated, spherical Zerodur® mirrors in a Herriott cell optical configuration [Herriott et al, 1964; Altmann et al., 1981]. Folding the laser beam in this way allows the relatively small cell (0.71859 m length) to contain a much longer optical path of 61.799 m. Reflection losses are minimized by the Au overcoat, which has an infrared reflectivity greater than 99%. Appendix 1 contains a general description of the optical properties of Herriott cells and a derivation of the relevant equations. In short, the entrance and exit beams pass through the same hole in the near mirror, provided the Herriott cell mirror separation is correct (±1 mm) and the entrance ray is roughly in the right direction. This makes the optical system very resistant to misalignment for three reasons. First, the final beam will exit the cell through the entrance hole even if the mirrors are not perfectly level. The author has

experimentally verified that the far mirror can sag by several cm perpendicular to the cell without losing signal or even changing the number of reflections within the cell. Second, the forward optics were designed to be in the correct geometry such that if the laser beam passes through the mirror hole, the return beam will automatically hit the return mirror because the slopes of the entrance and exit rays are symmetric. Third, the lever rule applies to the exit beam. The distance from the near Herriott cell mirror to the detector is smaller than the length of the Herriott cell, so even if the instrument flexes and changes the pointing of the beams onto the far mirror, the beam shift at the detector is smaller.

The most useful property of Herriott cells is that for given entrance and exit beam slopes, the number of reflections depends only on the separation of the two mirrors and their focal length f. If the spacing between mirrors is changed by several mm, the Herriott cell beam pattern shifts to a different number of reflections, but the exit beam still points in the same direction. There are different symmetries to the beam patterns depending on whether the mirror separation d is $\leq f$, $\geq f$, $\leq 2f$, or $\geq 2f$. The particular set of solutions used in ALIAS II was derived by the author. For mirror separation $d < f$, the number of allowed Herriott cell passes n obeys the equation

$$n = 6\mu + 2\,, \quad \text{for } \mu = 1,2,3,\ldots \tag{2.14}$$

To achieve n passes, the required mirror separation

$$d = 2f\left[1 - \cos\left(\frac{n-2}{3n}\right)\pi\right] \tag{2.15}$$

Table 2 in Appendix I is a list of possible solutions to (2.15) for the 0.750 m focal length mirrors of ALIAS II. Currently, the Herriott cell is set at 86 passes for a total pathlength of 61.799 m. The spot patterns made by the laser beams on the near and far mirrors in this configuration are shown in Figures 7a and 7b, respectively.

Thermal stability of the instrument is critical to the stability of the optics. By the Beer-Lambert Law (equation 2.2), small infrared absorptions are directly proportional to the optical pathlength through the absorbing gas. Therefore, it is essential to maintain the Herriott cell at a constant length. This is achieved by using invar rods to separate the cell mirrors and define the cell length. Invar is a special Fe-Ni alloy with a very small thermal expansion coefficient of 1.3×10^{-6} $°C^{-1}$, so even a temperature change of 100°C will change the optical pathlength by only 0.013%. This is a negligible contribution to the uncertainty in the calculated volume mixing ratio.

Thermal stability is also important in maintaining alignment of the optics. Outside the Dewar, all the rigid support structures of the forward optics are aluminum, so thermal expansion is very nearly isotropic. Hence, temperature shifts will cause changes of scale, but will not affect the pointing of the forward optics. Since no infrared absorption occurs in the purged forward optics between the Dewar and the Herriott cell, scale changes are unimportant. Thermal expansion of the Dewar does not affect alignment because its outer skin is aluminum like the rest of the support structures, and the lasers and

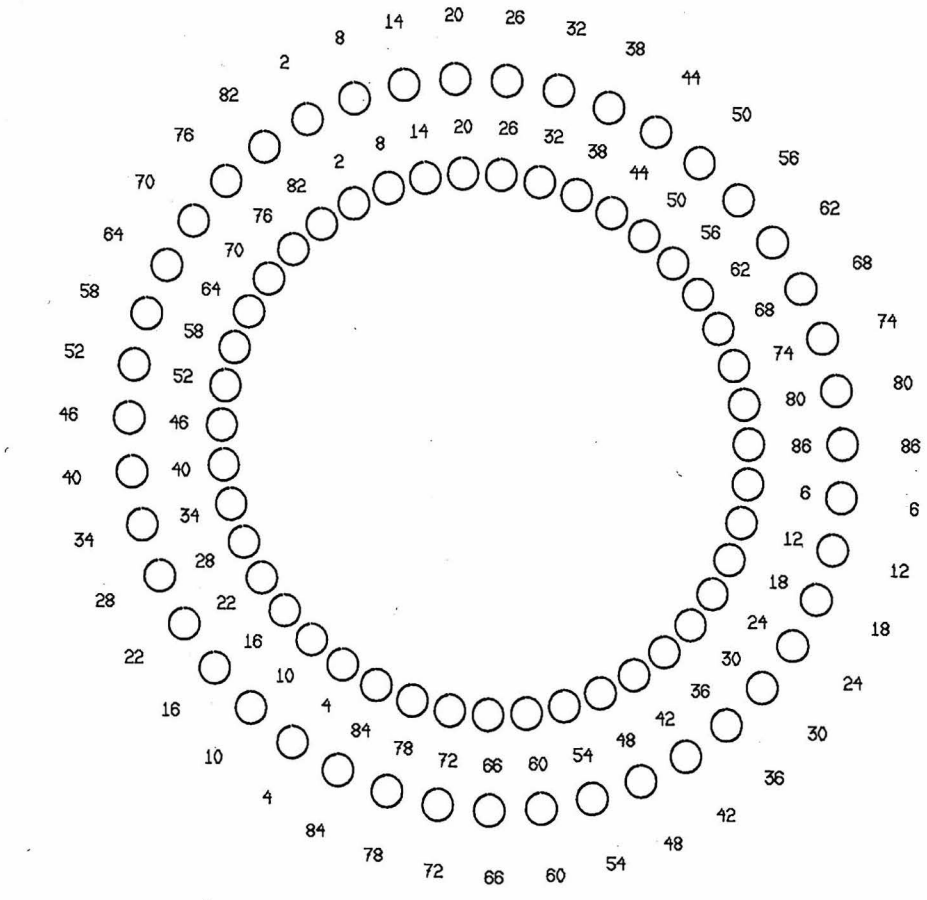

Figure 7a. Near mirror: spot patterns created at the intersection of the infrared beams and the reflective surface of the near mirror of the Herriott cell. The infrared beams enter and exit the Herriott cell through an aperture located at spot number 86. Note: upward orientation is toward the left.

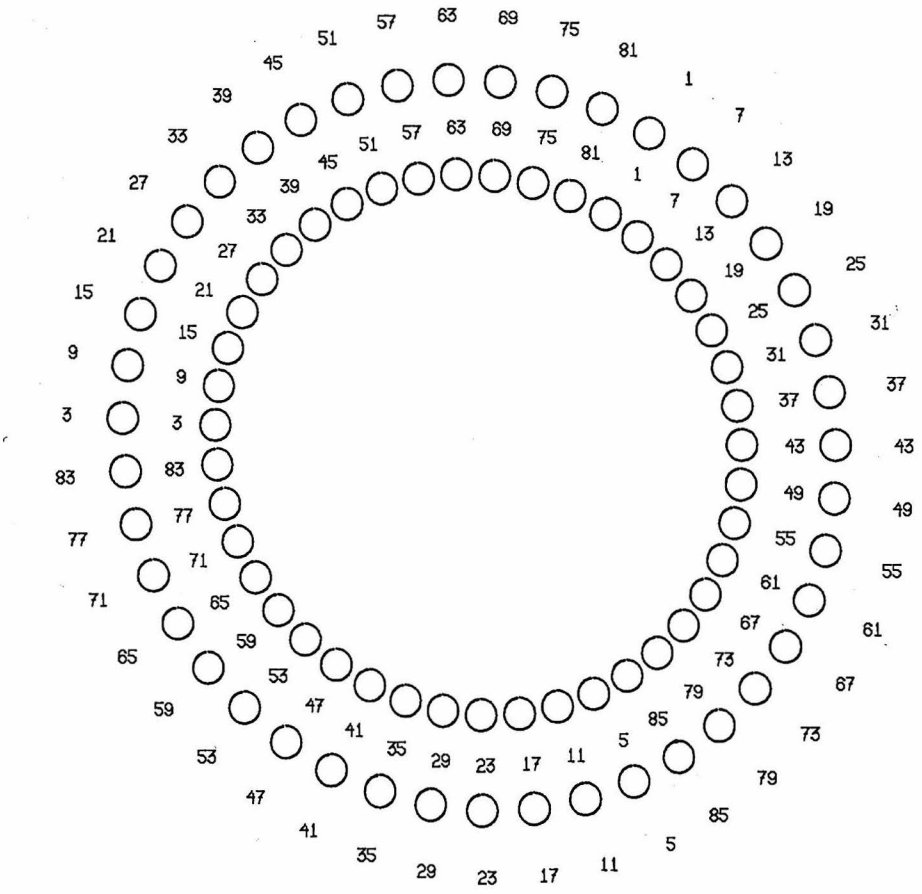

Figure 7b. Far mirror spot patterns. With 86 passes, C_{43v} is the symmetry point group of the beams in the Herriott cell. However, the angle between consecutive spots on the same mirror is almost 120°, so the point group is almost C_{3v}.

detectors inside the Dewar are maintained at a near-constant temperature. There are second-order thermal effects that change the optical alignment, but we have verified during the flights of ALIAS II that even though some exposed portions of the instrument changed temperature by as much as 30°C (see Figure 4), return laser power was reduced by only 30%. This change does not significantly affect the volume mixing ratio because the spectroscopic signal is normalized to return power, as given by (2.12).

2.5 Data Acquisition

For ALIAS and ALIAS II, data acquisition is controlled by a 90 MHz computer with a 80586 processor (Diversified Technology Model 3010). The operating program controls laser scans, data acquisition, heaters, and the two solenoids. It runs the instrument in two different modes: one for setup and calibration on the ground, and the other for data collection during flight. A library of low-level graphics routines are used to display the 2f harmonic spectra, return laser power, ambient pressure and temperature, and component temperatures. Commands can be entered at the keyboard to set laser scan range, modulation amplitude, laser heater current, and gain settings.

The laser current controller scans each TDL across an absorption line at a 10 Hz repetition rate [Webster et al., 1994]. Each TDL is turned off for 1 msec at the beginning of each 100 msec period to provide an accurate auto-zero trace for the null circuit and an accurate zero absorption reference. At 0.1 msec after the beginning of this brief TDL-off period, a trigger is sent to the custom 16-bit

signal averager to begin data acquisition. Thirty individual 100 msec spectra are acquired from the AC (2f harmonic spectra) and DC (return laser power) channels for each laser, and are averaged to produce spectra every 3 sec. The averaged spectra are transferred to the main control program once every 3 sec. Because the signal averager operates independently of the main 80586 processor, the software control of engineering parameters is carried on simultaneously with data acquisition during the 3 sec that are available while the spectra are being averaged.

2.6 Data Processing

Flight data are retrieved and processed in two stages. During the balloon flight, a limited subset of ALIAS II data is transmitted to the ground by telemetry every 3 sec and approximate volume mixing ratios are calculated. Telemetry is essential because of the relatively high risk of crash landings of stratospheric balloon payloads. It is also useful as a real time indicator of volume mixing ratios, pressure, and temperature. Once the payload has been recovered, the complete flight data are downloaded from the 540 Mbyte flight hard disk and processed in the same manner as ALIAS [Webster et al., 1994; May and Webster, 1993].

Telemetered data are received by engineers of the National Scientific Balloon Facility who closely monitor the balloon flight. ALIAS II sends a data downlink through an RS-232 cable to a constant bandwidth voltage controlled oscillator (VCO) aboard the balloon gondola. The VCO transmits the data at a

frequency of 1.5 GHz to a ground receiving station. There, the signals of the six different instruments aboard the balloon gondola are separated from each other by an electronic discriminator, and are converted to a bipolar electrical signal sent by RS-232 directly into the ground computers. The data sequence downlinked by telemetry from ALIAS II is as follows:

hours
minutes
seconds
pressure (raw counts)
temperature (raw counts)
x_1 (channel 1)
y_1 (channel 1)
x_0 (channel 1)
x_2 (channel 1)
y_2 (channel 1)
left lobe minimum (channel 1)
2f peak (channel 1)
right lobe minimum (channel 1)
x_1 (channel 2)
y_1 (channel 2)
x_0 (channel 2)
x_2 (channel 2)
y_2 (channel 2)
left lobe minimum (channel 2)
2f peak (channel 2)
right lobe minimum (channel 2)

(the x and y coordinates are shown graphically in Figure 8). From these data, the 2f peak-to-peak signal and the laser return power are calculated. Mixing ratios are calculated using software developed by R. D. May, based on his original software for BLISS, the Balloon-borne Laser In Situ Sensor [Webster et al., 1987]. In principle, mixing ratios derived from telemetered data should be close to the mixing ratios derived from the full dataset. However, they are

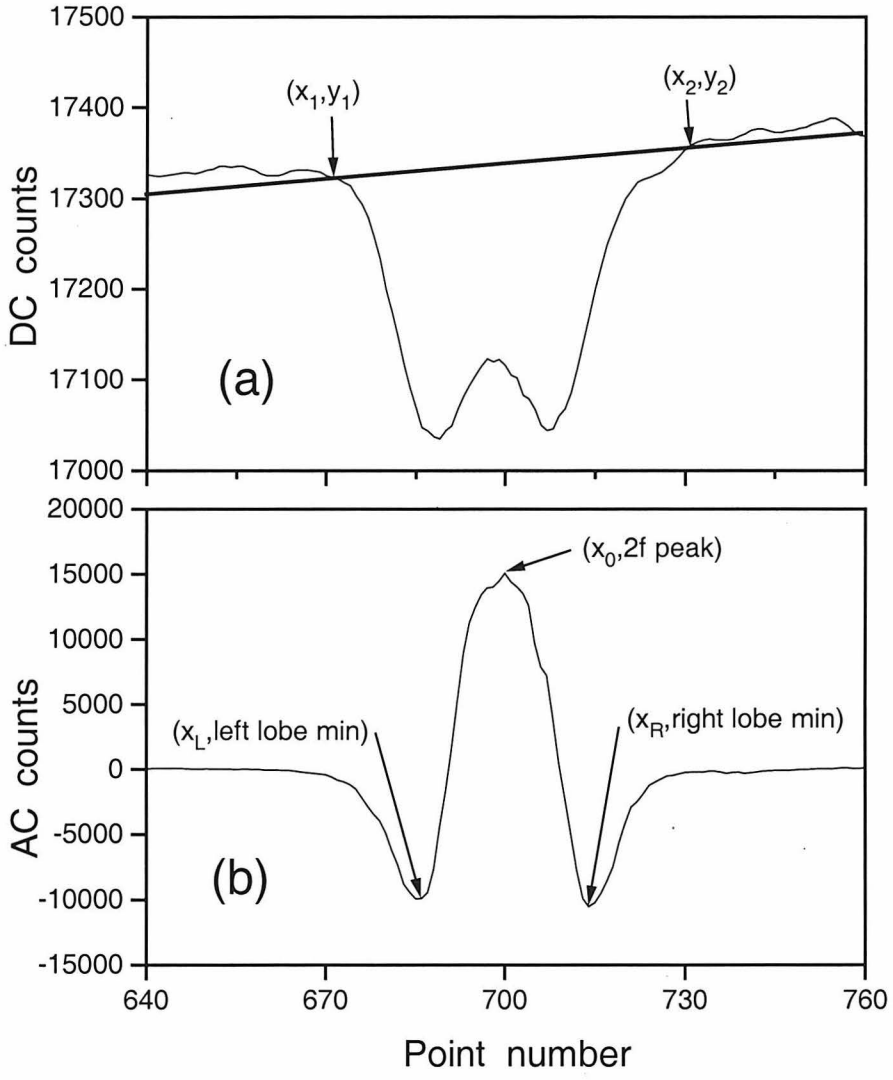

Figure 8. CH_4 spectra measured by ALIAS II (same as in Figure 3) showing the coordinates that are transmitted to the ground by telemetry every 3 sec during balloon flight. Points x_1 and x_2 are twice as far from linecenter x_0 as the lobe minima.

less precise because the telemetered data only contain the maximum amplitude of the 2f signal, not the entire 1024-bit spectrum. In addition, the telemetry signal occasionally has transmission dropouts. It is thus highly desirable to recover the instrument hard disk after the flight to reduce the full spectra.

After landing and recovery of the gondola, flight files are transferred from the instrument hard disk to a DIGITAL Vax Station 4000 by file transfer protocol (ftp). On the vax, the data reduction software is essentially the same as for ALIAS [Webster et al., 1994; May and Webster, 1993]. To reduce processing time, a matrix containing calculated peak-to-peak 2f signal sizes $H_2(calc)$ is generated for each desired absorption line, for a fixed mixing ratio $\chi(calc)$, and for a broad temperature and pressure range (see Spectroscopic Theory section). For each flight file, the first and last 2f spectra are displayed on the vax monitor, and the computer mouse is used to select the desired absorption line. As described above, a polynomial filter is applied to the data, the filtered peak-to-peak 2f signal size y is measured, and the observed mixing ratio $\chi(obs)$ is calculated using equations (2.12) and (2.13). The polynomial filter results in a more precise estimate of y than in the telemetered data processing. To further improve the precision for CH_4, the author reduces all four resolved CH_4 lines (see Figure 3) and then averages the calculated mixing ratios. The final N_2O and CH_4 dataset is the one reduced with the vax using the full spectra and the best estimate of temperatures during flight (see discussion of temperature in the next section).

2.7 Instrument Calibration

To calibrate ALIAS II, one needs to know accurately the temperature, pressure, laser properties, spectral line parameters, and instrument response function (i.e., the conversion factor between 2f peak-to-peak amplitude and volume mixing ratio). The calibration procedure is similar to that for ALIAS [Webster et al., 1994; May and Webster, 1993], except that the range of temperatures and pressures is much greater. On ALIAS, the air is heated to 298 K before entering the closed-path Herriott Cell, and the lowest pressure ever encountered by the ER-2 aircraft is 50 hPa. In contrast, the open-path Herriott Cell of ALIAS II is exposed to ambient temperatures (180 to 300 K) and pressures as low as 9 hPa. Hence, the accuracy of the temperature and pressure measurements is critical.

Temperature is measured with a fast-response thermistor (Thermometrics, Inc.) by comparing its resistance with that of a precision resistor. The resistance of the thermistor increases as the temperature drops, according to the following relationship:

$$T^{-1} = 0.002841 - 1.79133 \cdot 10^{-4} \ln R_{thermistor} + 5.08283 \cdot 10^{-5} \left(\ln R_{thermistor}\right)^2 - 1.58017 \cdot 10^{-6} \left(\ln R_{thermistor}\right)^3 \quad (2.16)$$

The thermistor resistance was calibrated in a cooled methanol bath over the temperature range 233 K < T < 283 K, and in a dry ice-acetone slurry at 195 K. The author calculated (2.16) with a least squares fit of a third-order polynomial to the data. Although the thermistor temperature can be determined accurately

(±0.5 K), this temperature is not necessarily the same as the air temperature. When the thermistor is exposed to direct sunlight, it becomes 10 to 20 K warmer than the background air. To minimize the solar exposure of the thermistor during balloon flights, we suspended it 1 m below the base of the gondola. Even in the shade, though, the thermistor does not record an accurate air temperature unless it is well-ventilated. Figure 9 shows the temperature profiles recorded by four different instruments during the 970630 (yymmdd format) flight. Rapid oscillations in temperature are caused by a combination of solar heating and poor ventilation (the vertical velocity of the balloon was not constant and sometimes went to zero). On ascent, even the minimum temperatures recorded by ALIAS II are 10 K too warm because of poor ventilation. On descent, the thermistor is better ventilated, so the minimum ALIAS II temperatures are at most 2 K warmer than the best temperature estimate. The best temperature measurement is the lowest one since it is very easy for a thermistor to be hotter than its surroundings, but nearly impossible for it to be colder (background temperature fluctuations along the balloon flight path are much slower than the response time of the thermistor). It is apparent from Figure 9 that compared to a well-ventilated, simultaneously launched Vaisala radiosonde (the "free-flyer"), the best temperature measurements on the gondola are accurate to only ±2 K.

Pressure is measured aboard ALIAS II with an MKS baratron (1333 hPa full scale). It is periodically calibrated by the Physical Measurement Standards Laboratory at JPL. The manufacturer claims an accuracy of ±0.15% when

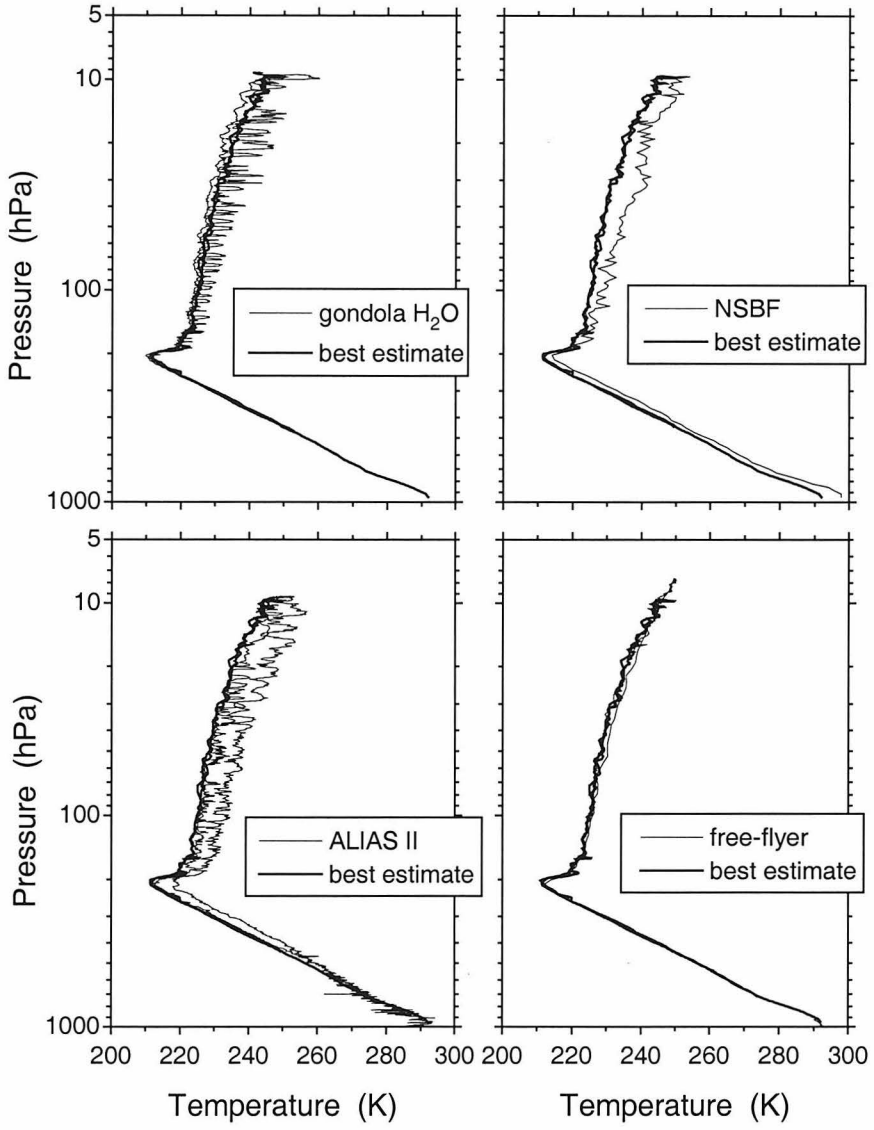

Figure 9. Ambient temperature measurements made during the OMS balloon flight of 970630. The instruments that measure temperature are gondola H_2O, NSBF, ALIAS II, and a Vaisala radiosonde ("free-flyer") that is launched separately.

properly calibrated and mounted in a stable laboratory environment. However, this level of accuracy is not observed during balloon flights because the baratron is subject to large temperature changes. The realistic flight accuracy of the baratron is ±1.5% for pressures between 13 and 100 hPa, determined from comparisons with higher resolution baratrons from the JPL O_3 instrument on the same balloon payload. This accuracy does not include linear offsets of the baratron. However, pumpdown calibrations (described below) compensate for a linear offset provided it does not change between calibration and flight (typically one to two weeks later). We have verified this by comparing mixing ratios calculated during calibration with model mixing ratios, assuming a linear offset estimated from the subsequent balloon flight. As shown in Figure 10, these mixing ratios generally agree to within 5% (see further discussion at the end of this section).

The laser physical properties that must be measured during calibration include linewidth, frequency mode quality, tuning rate, and modulation. TDLs maintain constant physical properties while continually cooled to < 100 K, but thermal recycling sometimes changes them. However, the author has observed only small changes in the properties of the ALIAS II lasers even after being recycled three times.

Laser linewidth is important because it significantly contributes to the width of low-pressure, narrow absorption lines. It is determined by measuring the absorption spectrum of a pair of Doppler-broadened lines with known linecenter frequencies and known temperature. The Doppler-broadened

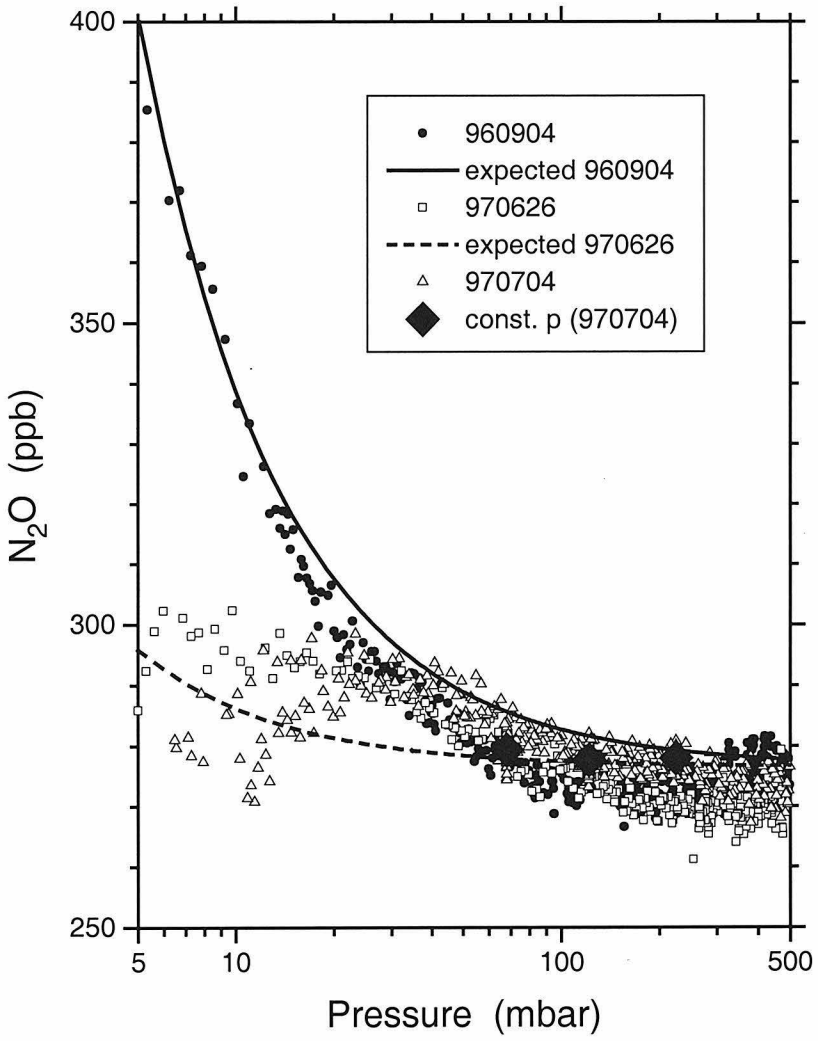

Figure 10. ALIAS II N_2O mixing ratios measured during pumpdown calibrations (points) and modeled assuming that pressure readings have the same linear offset as during flight.

linewidth γ_D is a function only of frequency, temperature, and molecular mass (see equation 2.5). We have verified that for both ALIAS II lasers, low-pressure spectra are well-approximated by Gaussian lineshapes (HWHM = γ). The convolution of two Gaussians with the same linecenter is still Gaussian, so it is reasonable to assume that the laser contribution to the linewidth is Gaussian. In this case, the laser linewidth γ_{laser} is

$$\gamma_{laser} = \sqrt{\gamma^2 - \gamma_D^2} \tag{2.17}$$

For the N_2O laser, γ_{laser} = 78±2 MHz at 2207 cm^{-1} and for the CH_4 laser, γ_{laser} = 83±5 MHz at 2948.1 cm^{-1}. Even for CH_4, the uncertainty in γ_{laser} introduces an error of less than 1% in the calculated mixing ratio.

TDL frequency modes are typically separated by about 3 cm^{-1}, so adjacent modes do not scan across the same absorption line. Therefore, mixing ratio is directly proportional to the single-mode fraction of the intensity. This fraction, called mode purity, is determined simply by measuring the laser power with and without a mode gas cell in the beam. A mode cell contains enough pure gas to completely absorb the laser beam at linecenter. For both ALIAS II lasers, the mode purity is >98% and can be measured to better than ±0.1% accuracy.

Tuning rate is the conversion between current applied to the laser and the frequency emitted. An acceptable laser has a nearly linear tuning rate and scans continuously across 1 cm^{-1} without jumping to another frequency mode. A 76.2 mm-thick Ge etalon in the beam creates Fabry-Perot interference

fringes regularly spaced in frequency. The fringe spectrum is recorded and the number of fringes per current range yields the tuning rate.

In second-harmonic spectroscopy, it is critical to know the amplitude of the applied laser modulation (see equation 2.10). The conversion between amplitude in current (mA) and amplitude in frequency (cm^{-1}) is approximately the same as tuning rate, but there are small differences possibly due to capacitance losses [May and Webster, 1993]. The conversion is determined by recording second-harmonic spectra over a large range of modulation currents. A FORTRAN program written by R. D. May compares the observed 2f peak-to-peak spectra with theoretical spectra to yield the modulation amplitude conversion factor Ω (cm^{-1}/mA). Another technique to obtain Ω is to reduce pumpdown calibration data (see below) measured over a wide range of pressures [May and Webster, 1993]. If the calculated volume mixing ratio is independent of pressure, then the modulation and all the other laser and spectroscopic parameters are likely to be correct. If the calculated mixing ratio increases with pressure, then the actual modulation is larger than the one used to reduce the data. The opposite is true if the calculated mixing ratio decreases with pressure. By trial and error, the actual modulation (cm^{-1}) and Ω can be determined to $\pm 3\%$ accuracy. In sensitivity studies, the author has found that a 3% uncertainty in modulation corresponds to mixing ratio uncertainties of 3% for pressures greater than 200 hPa and 1.5% for pressures less than 200 hPa.

In principle, mixing ratios can be derived from spectroscopic measurements using only the spectroscopic line parameters [e.g., Rothman et al., 1992]. For reactive gases such as NO_2, HNO_3, or HCl, accurate gas

standards are difficult to make, and we depend on the accuracy of the line parameters. However, for relatively stable species like N_2O, CH_4, and CO, accuracy is improved by calibrating the instrument with a known gas standard. To ensure high accuracy, we perform a "pumpdown calibration" on ALIAS II before every balloon flight. In a pumpdown calibration, the instrument response function is determined by recording spectra of a gas standard over the entire pressure range of the instrument (500 to 5 hPa) [Webster et al., 1994]. J. W. Elkins of the National Oceanic and Atmospheric Administration (NOAA) Climate Monitoring and Diagnostics Laboratory (CMDL) has provided the following gas standard for ALIAS II calibration:

Cylinder CA-2789
276.5±3 ppb N_2O
1150.9±12 ppb CH_4
193.9±4 ppb CO
remainder: zero air

This gas standard is traceable to original standards of the National Institute of Standards and Technology (NIST). To perform a pumpdown calibration, the instrument is left on and running in flight mode to stabilize the electronics, baratron, and lasers. An aluminum tube is placed over the Herriott cell, sealed with an o-ring flange, evacuated, and flushed with dry N_2 to purge the chamber of any residual room air. Then, the chamber is backfilled with 500 hPa of the gas standard. Spectra are written to file using the same laser parameters as during flight. After one minute, the pressure is reduced by approximately 25 hPa to record another set of spectra. At pressures less than 100 hPa, the step size is reduced to 10 hPa. In this stepwise fashion, the instrument records spectra over the entire pressure range for a constant volume mixing ratio. The

pumpdown data as a function of pressure are fitted with a polynomial curve, and the calibration correction curve is simply the ratio of the known mixing ratio to the polynomial. In this way, we can correct for systematic errors in spectral linestrength, instrument response, or pressure measurement.

The data from three typical pumpdown calibrations are shown in Figure 10. The first one, recorded on 960904 (yymmdd format), show large deviations at low pressure. During the 960921 balloon flight, we noted a -2.5 hPa linear offset in the ALIAS II pressure readings. The solid line in Figure 10 represents the mixing ratios expected for this pressure offset. It is apparent that a linear offset can explain most of the deviation. In contrast, the pumpdowns of 970626 and 970704 cannot be explained by the corresponding offset (-0.34 hPa) observed during the 970630 balloon flight. For pressures greater than 20 hPa, these two pumpdowns yield consistent mean mixing ratios within 3% of each other even though ALIAS II had a flight between the pumpdowns. The three large diamonds in Figure 10 indicate that consistent mixing ratios are also retrieved during three long calibration runs at constant pressure. We assume that for pressures greater than 20 hPa, the residual offset is caused by nonlinearities in the system that do not change between calibration and flight.

2.8 Accuracy and Precision

The flight environment is harsher than the laboratory environment, so the accuracy of ALIAS II is assessed by comparison with other N_2O and CH_4 instruments. These instruments generally agree to within ±5%, although the

accuracy is somewhat worse at pressures less than 30 hPa (see Chapter 4 for an extended discussion). This is not surprising considering the variations seen at low pressures during pumpdown calibrations (see Figure 10). At pressures less than 20 hPa, the accuracy is roughly ±10% assuming that the baratron offset does not change between pumpdown calibration and flight. There is a discrepancy in the CH_4 measurements of the two balloon instruments, but most independent measurements of stratospheric CH_4 are in good agreement with the ALIAS II data (see Chapter 4). Accuracies of ±5% over the pressure range of 30 hPa to 500 hPa represent an improvement over previous *in situ* measurements of N_2O and CH_4 [e.g., Goldan et al., 1981; Fabian et al., 1981].

The laboratory precision of ALIAS II is estimated to be ±1% over a wide range of pressures. However, flight precision is ±3% because the optical alignment degrades during flight. In addition, there is a mixing ratio asymmetry between balloon ascent and descent of approximately 5 to 10 ppb N_2O and 40 to 50 ppb CH_4. Considering that balloon flights are only six hours in duration, and the horizontal transport of the balloon is typically less than 100 km, long-lived trace gases such as N_2O and CH_4 should not be significantly different on ascent and descent. Furthermore, in a plot of CH_4 *vs.* N_2O, ascent and descent data should be indistinguishable according to the theory of Plumb and Ko [1992] (see Chapter 5). Since the CH_4 *vs.* N_2O plot shows the same difference between ascent and descent, it is likely an instrumental artifact. The most likely cause of this asymmetry is temperature drift of the electronics.

2.9 Suggestions for future improvements

ALIAS II has worked on all six of its balloon flights, returning data of high scientific quality which will be interpreted in Chapter 5. However, there are many ways in which the performance of ALIAS II could be improved. It is clear from the six balloon flights that this instrument would benefit from greater stability and better precision and accuracy. For instance, in plots of ALIAS II N_2O *vs.* Harvard CO_2 (see Chapter 4), most of the scatter is due to instrumental noise in the ALIAS II measurements. As described below, improvements in one area generally help other aspects of the instrument.

The precision of the ALIAS II flight data is often limited by optical stability. As the pressure changes during a flight, differential stresses on the instrument cause slow changes in the alignment of the optics. This usually manifests itself as a decrease in return laser power during ascent. In addition, vibrations of the Herriott cell cause rapid fluctuations in the alignment. Both phenomena introduce noise into the spectra, but could be reduced using more rigid structural members. In addition, vibration-isolation mounts could be used to dampen vibrations set up by other instruments' pumps on the balloon gondola.

Other ways to improve precision include lower electronic noise and new data processing techniques. Through careful inspection of connections and components, it should be possible to identify and fix the sources of electronic noise. Precision might be improved by fitting the entire second-harmonic spectra instead of merely measuring the peak-to-peak amplitude. However,

this approach requires either a constant laser tuning rate or some way to calibrate the wavelength scale across the width of the spectral feature (perhaps by using a temperature-stabilized etalon).

The accuracy of ALIAS II is limited by the accuracies of instrument response, calibration, pressure, and temperature. Instrument response should, in principle, be constant. However, thermal drifts cause the response to change, particularly for the detector preamps. This problem could be alleviated by insulating the instrument better to improve its thermal stability. Thermal stability could also be improved by repackaging the electronics and improving the layout of the forward optics. In this way, ALIAS II could be more compact and thus easier to insulate. The electronics could be miniaturized by converting the old 34 cm-long circuit boards to 10 cm x 10 cm PC104 boards. Caution is urged, however, when upgrading the processor. The current processor has adequate speed to average and record spectra, but a faster one might overheat more easily at low pressures.

In-flight calibration is the only way to ensure that the instrument response is known accurately. There are reference cells aboard ALIAS II filled with gas standards, but when the cells are inserted into the laser beams, there is absorption from both the reference cells and the Herriott cell. We originally planned to install mirrors to bypass the Herriott cell during reference scans, but this feature has not yet been implemented. In the future, there should be independent calibration, mode, and Doppler (i.e., low pressure) reference cells aboard ALIAS II to better constrain the instrument response and the laser physical properties.

There is a long history of improving pressure and temperature measurements in the stratosphere. As stated above, baratron pressure gauges have a flight accuracy of ±1.5% and a linear offset of typically 0.4 hPa. A better pressure sensor would improve instrument accuracy, particularly at low pressures. One possibility is piezoelectric pressure transducers manufactured by Paroscientific, Inc.

Temperature is a more difficult problem because thermistors are often warmer than the environment. Thermistors mounted within the Herriott cell may be subject to solar heating. Walls to block the sunlight cause poor ventilation of the thermistor. The only ways to ensure no solar illumination are to fly at night or to orient the payload with the same side toward the Sun, as is done with the JPL MkIV interferometer [Toon, 1991]. ALIAS II has a unique problem because we want to determine the air temperature within the open-path Herriott cell, which may not necessarily be the same as the background temperature. Better ventilation from faster balloon ascent and descent might improve the temperature measurements.

The ALIAS II instrument has made six successful balloon flights to greater than 30 km altitudes, measuring N_2O and CH_4 mixing ratios. As described in Chapter 5, these measurements are used to infer important time scales of stratospheric circulation. Future improvements to this instrument promise to make it even more valuable for making stratospheric measurements. In particular, its open-path cell is ideal for *in situ* measurements of reactive species such as HCl, NO_2, or HNO_3 on balloon descent. ALIAS II is small enough to fit on a balloon payload with other instruments, allowing

simultaneous measurements of related species, such as ClO [Toohey et al., 1993], at altitudes unattainable by any aircraft. In this way, ALIAS II could contribute to photochemical studies of stratospheric O_3 loss at middle and high latitudes.

BIBLIOGRAPHY

Altmann, J., R. Baumgart, and C. Weitkamp, Two-mirror multipass absorption cell, *Appl. Optics, 20,* 995-9, 1981.

Fabian, P., R. Borchers, G. Flentje, W. A. Matthews, W. Seiler, H. Giehl, K. Bunse, F. Müller, U. Schmidt, A. Volz, A. Khedim, and F. J. Johnen, The Vertical Distribution of Stable Trace Gases at Mid-latitudes, *J. Geophys. Res., 86,* 5179-84, 1981.

Goldan, P. D., W. C. Kuster, A. L. Schmeltekopf, F. C. Fehsenfeld, and D. L. Albritton, Correction of Atmospheric N_2O Mixing-Ratio Data, *J. Geophys. Res.*, 86, 5385-6, 1981.

Herriott, D., H. Kogelnik, and R. Kompfner, Off-Axis Paths in Spherical Mirror Interferometers, *Appl. Optics, 3,* 523-6, 1964.

Humlicek, J., Optimized computation of the Voigt and complex probability functions, *J. Quant. Spectrosc. Radiat. Transfer, 27,* 437, 1982.

May, R. D., and C. R. Webster, Data processing and calibration for tunable diode laser harmonic absorption spectrometers, *J. Quant. Spectrosc. Radiat. Transfer, 49,* 335-47, 1993.

Monastersky, R., Voyage into unknown skies, *Sci. News, 139,* 136-7, 1991.

Plumb, R. A., and M. K. W. Ko, Interrelationships between mixing ratios of long-lived stratospheric constituents, *J. Geophys. Res., 97,* 10,145-56, 1992.

Rothman, L. S., R. R. Gamache, R. H. Tipping, C. P. Rinsland, M. A. H. Smith, D. Chris Benner, V. Malathy Devi, J.-M. Flaud, C. Camy-Peyret, A. Perrin, A. Goldman, S. T. Massie, L. R. Brown, and R. A. Toth, The HITRAN molecular database editions of 1991 and 1992, *J. Quant. Spectrosc. Radiat. Transfer, 48,* 469-507, 1992.

Schiff, H. I., G. I. Mackay, and J. Bechara, The Use of Tunable Diode Laser Absorption Spectroscopy for Atmospheric Measurements, Chapter 5 in *Air Monitoring by Spectroscopic Techniques*, M. W. Sigrist, ed., Wiley, New York, 239-333, 1994.

Toohey, D. W., L. M. Avallone, M. R. Schoeberl, P. A. Newman, L. R. Lait, D. W. Fahey, E. L. Woodbridge, and J. G. Anderson, The seasonal temporal evolution of reactive chlorine in the Northern hemisphere stratosphere, *Science, 261,* 1134-6, 1993.

Toon, G. C., The JPL MkIV interferometer, *Optics and Photonics News, 2,* 19-21, 1991.

Webster, C. R., and R. D. May, Simultaneous in situ measurements and diurnal variations of NO, NO_2, O_3, jNO_2, CH_4, H_2O, and CO_2 in the 40- to 26-km region using an open path tunable diode laser spectrometer, *J. Geophys. Res., 92,* 11,931-50, 1987.

Webster, C. R., R. D. May, C. A. Trimble, R. G. Chave, and J. Kendall, Aircraft (ER-2) laser infrared absorption spectrometer (ALIAS) for in situ stratospheric measurement of HCl, N_2O, CH_4, NO_2, and HNO_3, *Appl. Optics, 33,* 454-72, 1994.

Webster, C. R., R. T. Menzies, and E. D. Hinkley, Infrared laser absorption: theory and applications, Chapter 3 in *Laser Remote Chemical Analysis*, R.M. Measures, ed., Wiley, New York, 163-272, 1988.

Chapter 3

Measurements of CO in the Upper Troposphere and Lower Stratosphere

R. L. Herman [1], C. R. Webster [2], R. D. May [2], D. C. Scott [2], H. Hu [2], E. J. Moyer [1], P. O. Wennberg [1], T. F. Hanisco [3], E. J. Lanzendorf [3], R. J. Salawitch [2], Y. L. Yung [1], J. J. Margitan [2], and T. P. Bui [4]

[1]Division of Geological and Planetary Sciences, California Institute of Technology, Pasadena, CA 91125.

[2]Jet Propulsion Laboratory, California Institute of Technology, Pasadena, CA 91109.

[3]Atmospheric Research Project, Harvard University, Cambridge, MA 02138.

[4]NASA Ames Research Center, Moffett Field, CA 94035.

Submitted to *Chemosphere* on April 14, 1998

for the special issue on Atmospheric Carbon Monoxide and its Environmental Effects

Contribution number 5764 from the Division of Geological and Planetary Sciences, California Institute of Technology

Abstract. *In situ* measurements of CO were made in the upper troposphere and lower stratosphere (7 to 21 km altitude) with the JPL Aircraft Laser Infrared Absorption Spectrometer (ALIAS) on 58 flights of the NASA ER-2 aircraft from October 1995 through September 1997, between 90°N and 3°S latitude. Measured upper tropospheric CO was variable and typically ranged between 55 and 120 ppb, except for higher values over Alaska during summer 1997. Tropical stratospheric CO ranged from 58±5 ppb at the tropopause to 12±2 ppb above 20 km, having similar profiles in all seasons of the year. The tropical profile is reproduced by a simple Lagrangian box model of tropical ascent using measured CH_4 and OH concentrations, Cl and $O(^1D)$ concentrations from a photochemical model, and diabatic heating rates from a radiative heating model. At the highest altitudes attained by the ER-2, measured CO was close to the calculated steady-state mixing ratios of 10 to 15 ppb. However, in the lowermost stratosphere, CO was far from photochemical equilibrium. Calculations of photochemical loss of CO indicate that quasi-horizontal mixing between the tropical and mid-latitude lower stratosphere is rapid in the region between 400 K and 450 K potential temperature (altitudes less than 20 km).

3.1 Introduction

Carbon monoxide (CO) plays a central role in atmospheric photochemistry [e.g., Crutzen, 1995]. It has long been recognized that CO is the dominant sink of tropospheric OH, the primary oxidant in the troposphere

[Levy, 1971]. CO also contributes to O_3 production in the troposphere [e.g., Fishman and Crutzen, 1978; Seiler and Fishman, 1981], and potentially in the lowermost stratosphere as well [Bregman et al., 1997]. In the troposphere, the dominant sources of CO are oxidation of CH_4 and other hydrocarbons, biomass burning, and direct anthropogenic emissions [e.g., Logan et al., 1981]. In the lowermost stratosphere, the dominant source of CO is transport from the CO-rich boundary layer [e.g., Harriss et al., 1992, 1994], but at higher altitudes the dominant source is local production from CH_4 oxidation [e.g., Logan et al., 1981; Pinto et al., 1983]. CO is the longest-lived intermediate in the oxidation pathway from CH_4 to CO_2, which is initiated by:

$$CH_4 + X \rightarrow CH_3 + HX \quad (X = OH, O(^1D), \text{ or Cl; } X = OH \text{ dominant}) \quad (3.1)$$

Reaction (3.1) is the rate-limiting step in CO production from CH_4, and has a strong temperature-dependence for X = OH or Cl. Subsequent photochemical reactions rapidly produce CH_2O, which is photolyzed to CO.

The lifetime of CO with respect to photochemical loss is controlled by reaction with OH [Pressman and Warneck, 1970; Logan et al., 1981]:

$$CO + OH \rightarrow CO_2 + H \quad (3.2)$$

In the lower stratosphere, the CO mixing ratio is much greater than its steady-state value due to transport across the tropopause. As air ascends in the tropical stratosphere, CO decreases exponentially due to reaction (3.2) until photochemical steady-state is reached. Hence, in the lower stratosphere,

elevated CO can be used as a tracer of air that recently came from the troposphere.

Aircraft *in situ* measurements of atmospheric CO have the potential to improve our understanding of stratosphere-troposphere exchange and transport within the lower stratosphere because CO has a sharp gradient across the tropopause and a photochemical lifetime of only a few months. Aircraft measurements have excellent vertical resolution of the near-tropopause region compared to remote sensing observations [e.g., Gunson et al., 1996], yet have wide enough spatial coverage to carry out studies on regional to hemispheric scales. There have been many aircraft studies of CO up to 12.5 km altitude [e.g., Hoor et al., 1998; Waibel et al., 1998; Lelieveld et al., 1997; Ridley et al., 1997; Harriss et al., 1994; Anderson et al., 1993; Harriss et al., 1992], but the NASA ER-2 aircraft has made possible *in situ* measurements up to 21 km altitude. The ER-2 database is unique in the large number of trace gases that are measured simultaneously with particle concentration, solar irradiance, and meteorological variables [e.g., Tuck et al., 1997]. Aboard the ER-2, the Aircraft Laser Infrared Absorption Spectrometer (ALIAS) of the Jet Propulsion Laboratory (JPL) measures CO, N_2O, CH_4, and HCl concentrations with high precision and accuracy (see below) and a rapid 3-sec response time [Webster et al., 1994]. In 1995-7, ALIAS collected data on 58 flights of the ER-2 during two NASA campaigns: Stratospheric TRacers of Atmospheric Transport (STRAT) in 1995-6 and Photochemistry of Ozone Loss in the Arctic Region In Summer (POLARIS) in 1997. This paper describes the spatial distribution of upper tropospheric and lower stratospheric CO measured by ALIAS on those

campaigns. In addition, a simple model is used to constrain the CO photochemical lifetime, evaluate our understanding of ascent in the tropical lower stratosphere, and estimate quasi-horizontal mixing time scales in the lower stratosphere.

3.2 Aircraft Instruments

ALIAS is a high-resolution, scanning, mid-infrared absorption spectrometer that uses four tunable diode lasers (TDLs) to simultaneously measure CO, N_2O, CH_4, and HCl concentrations [May and Webster, 1993; Webster et al., 1994]. Harmonic spectroscopy enables ALIAS to achieve high sensitivity: absorptions as small as 1 part in 10^5 can be detected in a 3-sec integration period. The signal is amplified, filtered, and demodulated at twice the laser modulation frequency to yield second-harmonic spectra. Each of the four channels has an InSb or HgCdTe detector mounted inside the same liquid nitrogen Dewar as the TDLs. Thirty spectral scans are averaged together and written to a hard disk every 3 sec along with engineering data such as laser power, detector zero level, pressure, gas temperature, component temperatures, and heater powers.

The instrument is mounted in a pod on the right wing of the ER-2. Air is sampled through a heated inlet probe in front of the wing pod and flows through a 1-m absorption cell with a flush time of 1 to 2 sec. The 3-sec instrument response time allows measurements with high spatial resolution

along the flight path of the aircraft (approximately 600-m horizontal resolution, 50-m vertical resolution). Within the absorption cell, the infrared laser beams are reflected 80 times between two Au-coated spherical aluminum mirrors in a Herriott cell multipass optical configuration to achieve an 80-m optical pathlength. For CO, the instrument precision (±1 st. dev.) is ±0.7 parts per billion by volume (ppb) for 3-sec average data. For ground calibration, we use gas standards provided by the National Oceanic and Atmospheric Administration (NOAA) Climate Monitoring and Diagnostics Laboratory (CMDL). The gas standards are introduced into the absorption cell and spectra are taken over the range of pressures expected during flight. The estimated instrument accuracy (±1 st. dev.) is ±5% relative to these calibration standards.

In the following analysis, we use simultaneous measurements of CO, CH_4, OH, H_2O, and O_3 concentrations, temperature, pressure, and tropopause height obtained aboard the ER-2. The Harvard HO_x instrument uses laser-induced fluorescence to measure OH concentrations [Wennberg et al., 1994]. H_2O concentrations are measured by the Harvard H_2O instrument with Lyman-α photofragment fluorescence [Weinstock et al., 1994] and also by the JPL H_2O instrument using near-infrared TDL spectroscopy [May, 1998]. The NOAA O_3 instrument measures O_3 concentrations by ultraviolet absorption spectroscopy [Proffitt and McLaughlin, 1983]. Temperature and pressure are measured by the ER-2 Meteorological Measurement System (MMS) [Scott et al., 1990]. The JPL Microwave Temperature Profiler (MTP) is a passive microwave radiometer that measures O_2 thermal emission to calculate

temperature profiles, thereby determining the local tropopause height [Denning et al., 1989].

3.3 CO Distribution

ALIAS has measured CO in the upper troposphere (above 7 km) during the STRAT and POLARIS campaigns in 1995-7. In the upper troposphere, the abundance of CO varies considerably on daily to seasonal time scales [e.g., Logan et al., 1981]. Figure 1 shows monthly distributions of upper tropospheric CO measured at three latitudes: 65°N near Fairbanks, Alaska (11 flights); 37°N near NASA Ames Research Center, Moffett Field, California (17 flights); and 21°N near Barber's Point, Hawaii (20 flights). Data included in this figure are only for altitudes between 7 km and the local tropopause minus 1 km. Tropopause heights are determined from temperature profiles measured by the MTP and MMS instruments aboard the ER-2 [B. L. Gary, pers. comm.]. Generally, lower CO mixing ratios are found in the upper troposphere than at surface stations because most of the CO production occurs in the boundary layer [Logan et al., 1981]. Since the instrument precision is ±0.7 ppb CO, the scatter within each month of data reflects true atmospheric variability. Figure 1 indicates that upper tropospheric CO mixing ratios are generally greater at higher latitudes in the Northern Hemisphere, similar to previous observations [e.g., Robinson et al., 1984, and references therein].

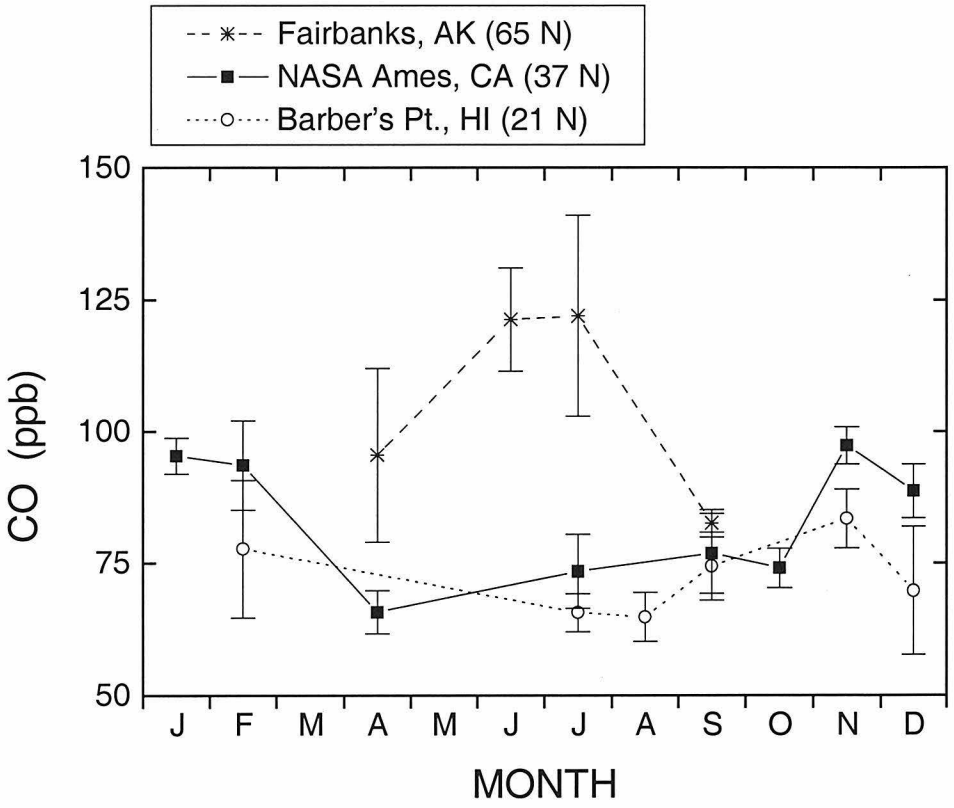

Figure 1. Upper tropospheric CO measured by ALIAS between 7 km altitude and the local tropopause minus 1 km. Symbols are monthly means (±1 st. dev.). Instrument precision is ±0.7 ppb, so the observed scatter within each monthly bin is evidence of atmospheric variability. These tropospheric data are from 11 flights at 65°N, 17 flights at 37°N, and 20 flights at 21°N.

The striking summer maximum of tropospheric CO over Alaska (Figure 1) is likely due to forest fires, which efficiently loft material to the upper troposphere [e.g., Waibel et al., 1998; Harriss et al., 1992, 1994]. The June and July data are similar to column CO measurements made from Fairbanks in the summer of 1995 [L. N. Yurganov, pers. comm.]. Such high mixing ratios of CO may lead to significant O_3 production in the upper troposphere [Fishman and Crutzen, 1978]. However, there is considerably less CO in the upper troposphere during April and September than during summer, possibly due to weaker convection at those times [Yurganov, 1997]. Thunderstorms and forest fires are associated with convection and are more likely to occur in summer.

At mid-latitudes (37°N, California), upper tropospheric CO has an annual maximum of 85 to 100 ppb in late autumn and winter, and a minimum of 60 to 70 ppb in spring (Figure 1). In the subtropics (21°N, Hawaii), upper tropospheric CO has a similar seasonal cycle with an annual maximum of 80 to 90 ppb and a minimum of 60 to 70 ppb. Note that the greatest variability in subtropical CO is seen in late autumn to winter (December and February). At both latitudes, synoptic-scale dynamics and stratosphere-troposphere exchange produce variability in CO on time scales of days to weeks.

The relationship between CO and O_3 is a useful indicator of transport between the stratosphere and troposphere [e.g., Hipskind et al., 1987; Lelieveld et al., 1997] because mixing ratios of these gases are strongly anticorrelated in the stratosphere [e.g., Hipskind et al., 1987; Murphy et al, 1993]. Figure 2 shows vertical profiles of temperature, CO, and O_3 measured during the 961208 (yymmdd format) subtropical flight of the ER-2 over Hawaii. In this

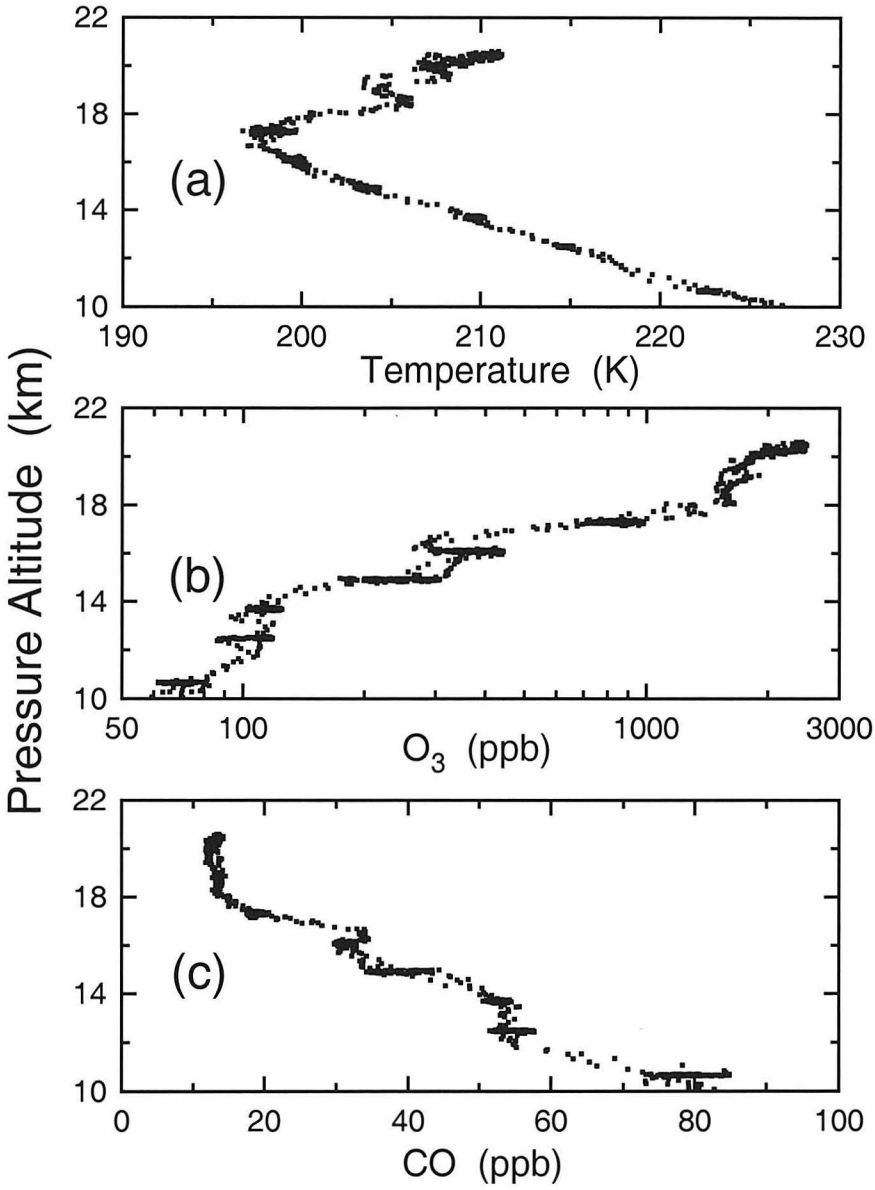

Figure 2. Subtropical profiles of (a) temperature (K), (b) O_3 (ppb), and (c) CO (ppb) measured during the 961208 (yymmdd format) flight of the ER-2 over Hawaii. The tropopause height is 16.5±0.1 km (θ = 387±2 K). Between 14 and 16 km altitude, tropospheric O_3 is unusually high and CO is low. Both aircraft ascent and descent are shown, although most of the data are clustered along constant-altitude legs.

flight, the ER-2 flew for approximately 30 minutes at each constant altitude leg in the upper troposphere and lower stratosphere. Air parcels of stratospheric origin are easily identified in the upper troposphere with a correlation plot of O_3 *vs.* CO (Figure 3a). The O_3 mixing ratio at the tropopause is typically 100 to 150 ppb over Hawaii in November, 1995, and December, 1996. More than 1 km below the local tropopause, measured O_3 and CO are not strongly correlated except during the flights of 961208 and 961209 (Figure 3a). In these two flights, the O_3 *vs.* CO relationship in the upper troposphere is very similar to the stratospheric anticorrelation found on all flights during November, 1995, and December, 1996 (Figure 3b). This suggests that the air recently came from the stratosphere. Upper tropospheric H_2O mixing ratios on 961208 were extremely low (4 to 5 parts per million), confirming the stratospheric origin of this air. Pollution and biomass burning are typically associated with elevated O_3 and CO [e.g., Harriss et al., 1992, 1994; Andreae et al., 1994], while the background troposphere has relatively low O_3 and CO mixing ratios, so high O_3 (> 150 ppb) and low CO (< 40 ppb) uniquely identify recent intrusions of stratospheric air into the upper troposphere.

Tropical CO profiles have been measured by ALIAS on five flights over the central Pacific Ocean (10°N to 3°S, 150 to 160°W), as shown in Figure 4. The aircraft typically descends from its cruise altitude of 21 km to a minimum altitude of 15 km, and then climbs back to 21 km, obtaining vertical profiles of CO in the tropical lower stratosphere and upper troposphere. We find that CO is less variable in the tropics than at higher latitudes in the Northern Hemisphere. Over the central tropical Pacific, the upper tropospheric CO

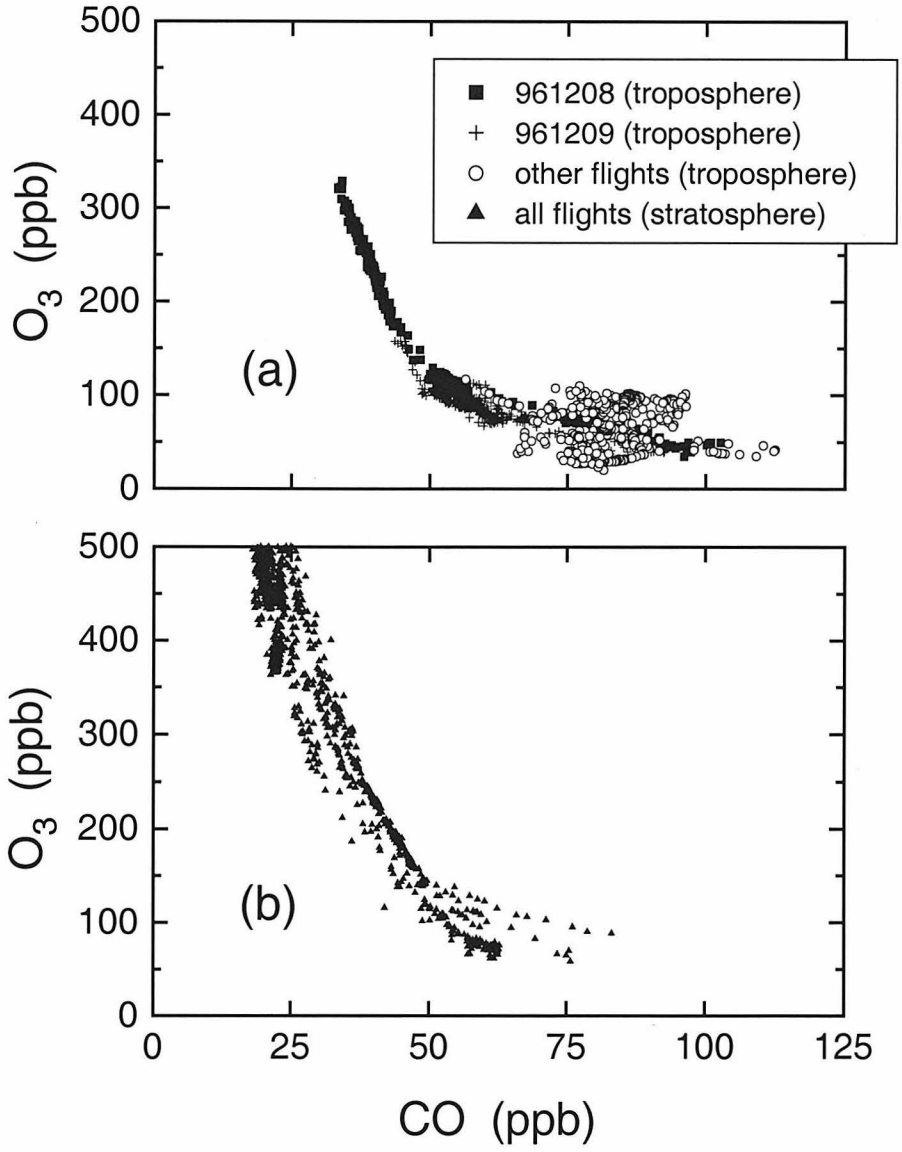

Figure 3. Subtropical O_3 *vs.* CO measured over Hawaii (21°N) during nine flights in November, 1995, and December, 1996. (a) Tropospheric data more than 1 km below the local tropopause: no correlation is apparent except for the flights of 961208 and 961209 (yymmdd format). On these two days, O_3 and CO are strongly anticorrelated, similar to the stratospheric data from all nine flights, shown in (b). This anticorrelation indicates that stratospheric air intruded into the upper troposphere recently before 961208. Further evidence is low H_2O mixing ratios of 4-5 parts per million.

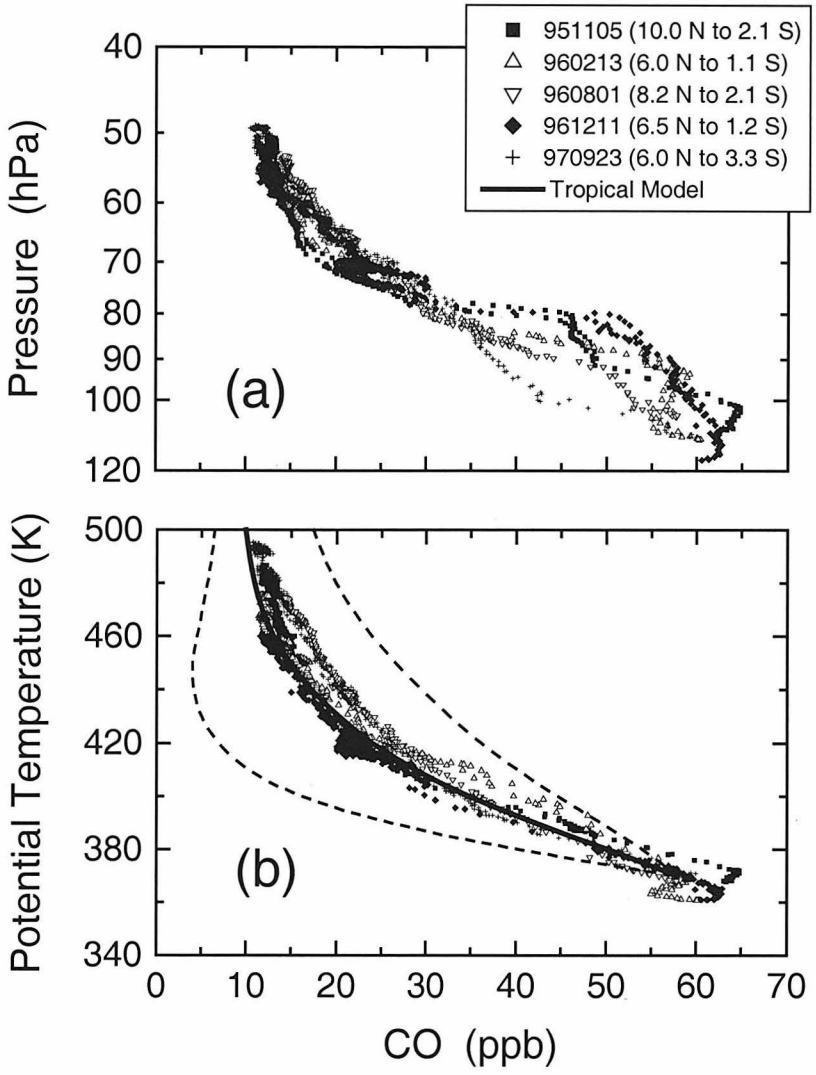

Figure 4. Tropical CO profiles measured by ALIAS on five flights over the central Pacific Ocean (150° to 160°W). (a) CO fluctuates as a function of pressure, depending on the height of the tropopause. (b) As a function of potential temperature, θ, CO has the same vertical profile throughout the year, with a tropical tropopause at 370±10 K. Solid line is tropical model CO and dashed lines represent total uncertainty (±1 st. dev.), including ±25% uncertainty in OH concentrations, ±30% uncertainties in reaction rate coefficients, and ±60% uncertainty in diabatic heating rates.

mixing ratio is 60±5 ppb with no apparent seasonal variation. These mixing ratios are typical of the background tropical troposphere uncontaminated by biomass burning plumes [P. Novelli, pers. comm.].

In the tropical lower stratosphere, the CO mixing ratio decays with altitude due to photochemical loss. The vertical profile of CO is strongly affected by seasonal variations in tropopause height (Figure 4a). However, the potential temperature of the tropical tropopause varies less than the altitude of the tropopause [Reid and Gage, 1996] (potential temperature is defined as the temperature of an air parcel adiabatically compressed or expanded to 1000 hPa). Potential temperature, θ, is a tracer of adiabatic motion and is conserved on time scales of approximately two weeks. The CO profile in the tropics varies little with season if θ is used as the vertical coordinate (Figure 4b). CO and θ are strongly anticorrelated in the tropical lower stratosphere because diabatic heating increases θ while photochemistry decreases the CO mixing ratio. The mean tropical tropopause for these five flights is at $\theta \approx 370 \pm 10$ K (altitudes ranging from 15.5 to 17.2 km) with a corresponding CO mixing ratio of 58±5 ppb. By $\theta = 390$ K, tropical air has CO abundances of only 45±5 ppb. The lowest mixing ratios of CO measured by ALIAS in the tropics are 12±2 ppb at altitudes above 20 km ($\theta > 470$ K). Weinstock et al. [1998] has used the functional relationship between CO and θ as a photochemical clock to infer the stratospheric age of air parcels. In the Analysis section below, we will demonstrate that the loss of tropical CO is consistent with measured concentrations of OH, rate coefficients for (3.1) and (3.2), and calculated heating rates.

The tropical correlation plot of O_3 *vs.* CO measured over the central Pacific Ocean (10°N to 3°S, 150° to 160°W) is shown in Figure 5. Tropical stratospheric O_3 and CO are anticorrelated due to local photochemical production of O_3 and destruction of CO [e.g., Avallone and Prather, 1996]. This correlation is in excellent quantitative agreement with previous measurements made during the Stratospheric Tropospheric Exchange Program (STEP) near Darwin, Australia [Figure 12 of Murphy et al., 1993; Figure 2 of Avallone and Prather, 1996], and appears to be a robust feature of the tropical stratosphere.

ALIAS measured CO in the stratosphere (up to 21 km altitude) on 58 flights between 90°N and 3°S in 1995-7. This database is extensive enough to map the seasonal distributions of CO in the Northern Hemisphere upper troposphere and lower stratosphere, as shown in Figure 6. Each contour plot uses data from at least fifteen flights, binned in increments of 20° latitude, 0.5 km altitude, and 10 K potential temperature. For altitudes below 15 km, data are limited to the vicinities of the landing bases at 21°N, 37°N, and 65°N. Figures 6a, 6c, and 6e use pressure altitude as the vertical coordinate. In the stratosphere, isopleths of constant CO mixing ratio slope downward toward the pole. There is typically 50 to 70 ppb CO at the mid-latitude tropopause, although sometimes less due to stratosphere-troposphere exchange.

To remove transient motions that produce no net vertical transport, potential temperature is used as the vertical coordinate in Figures 6b, 6d, and 6f. It is immediately apparent that the isopleths are flatter in θ than in altitude. The stratosphere can be divided into two layers: the "overworld" ($\theta > 380$ K),

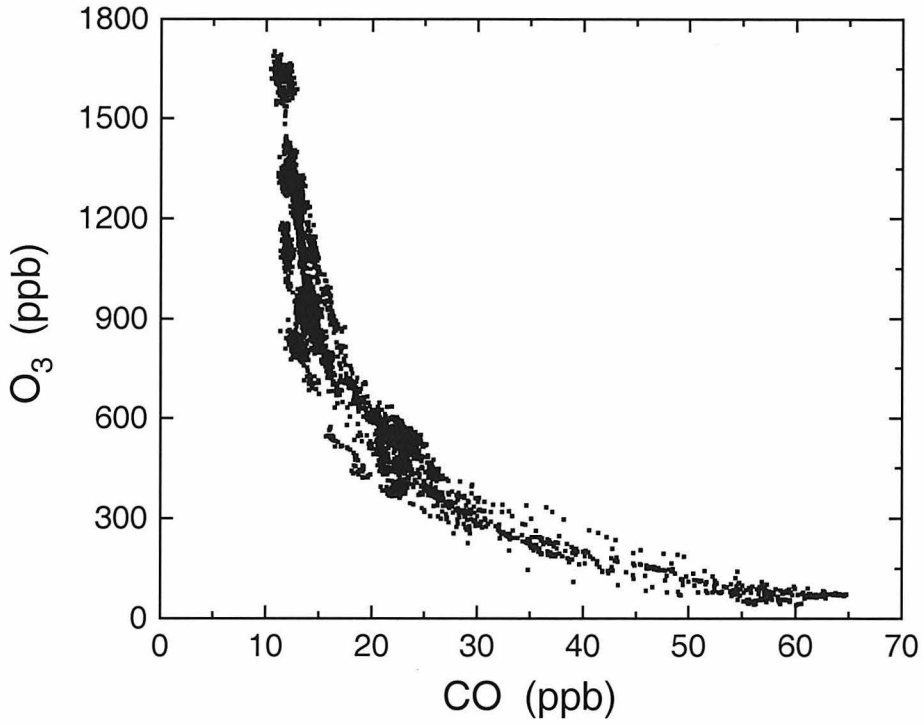

Figure 5. Tropical O_3 *vs.* CO measured over the central Pacific Ocean (flight dates and latitude ranges are the same as in Figure 4). This relationship is very similar to that observed during the Stratospheric Tropospheric Exchange Program (STEP) near Darwin, Australia [Figure 12 of *Murphy et al.*, 1993; Figure 2 of *Avallone and Prather*, 1996].

Figure 6. (on following pages) ALIAS CO distribution (ppb) in the upper troposphere and lower stratosphere of the Northern Hemisphere. These plots represent seasonal averages created by binning the data every 20° latitude and 0.5 km altitude (or 10 K potential temperature): (a) winter 1996 and spring 1997 altitude *vs.* latitude (15 flights), (b) winter 1996 and spring 1997 potential temperature *vs.* latitude (15 flights), (c) summer 1996 and 1997 altitude *vs.* latitude (21 flights), (d) summer 1996 and 1997 potential temperature *vs.* latitude (21 flights), (e) autumn 1995, 1996, and 1997 altitude *vs.* latitude (21 flights), (f) autumn 1995, 1996, and 1997 altitude *vs.* latitude (21 flights).

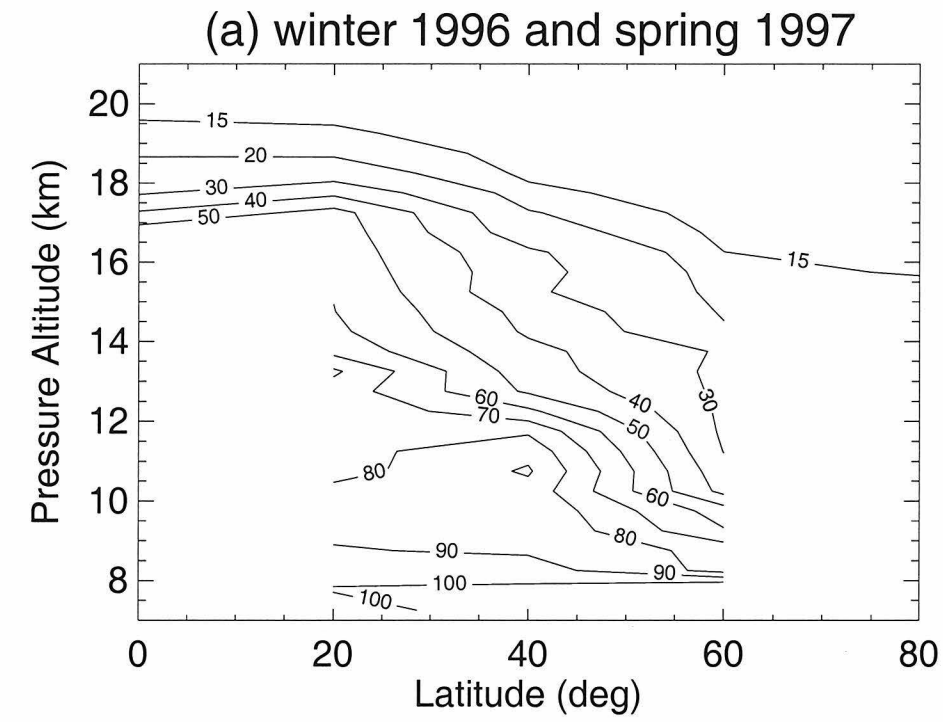
(a) winter 1996 and spring 1997
Pressure Altitude (km)
Latitude (deg)
20
18
16
14
12
10
8
0
20
40
60
80
15
20
30
40
50
60
70
80
90
100

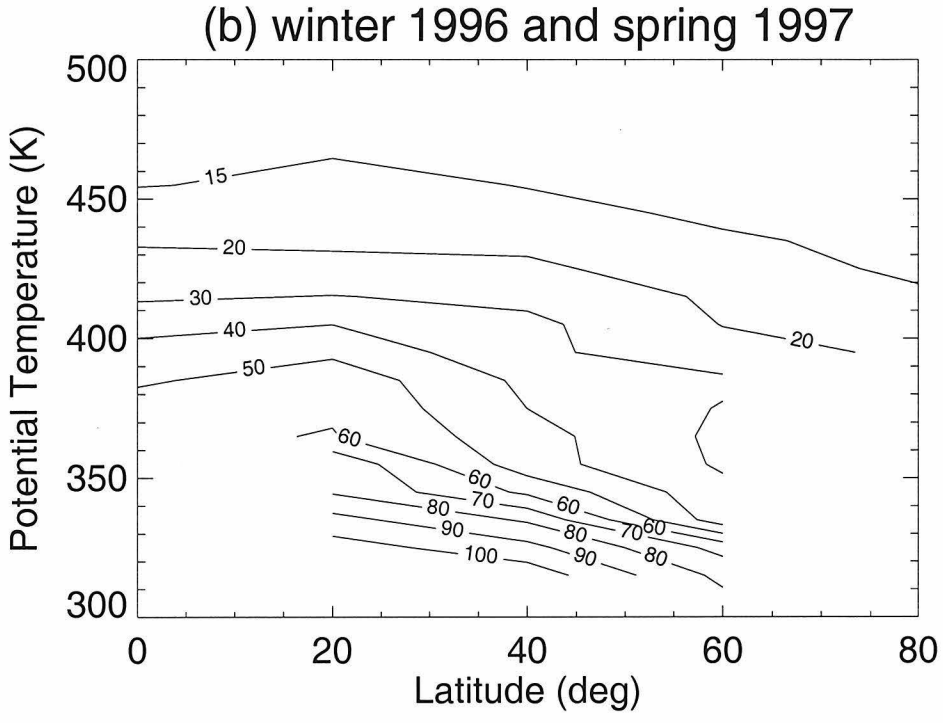
(b) winter 1996 and spring 1997
Potential Temperature (K)
Latitude (deg)
500
450
400
350
300
0
20
40
60
80
15
20
30
40
50
60
70
80
90
100

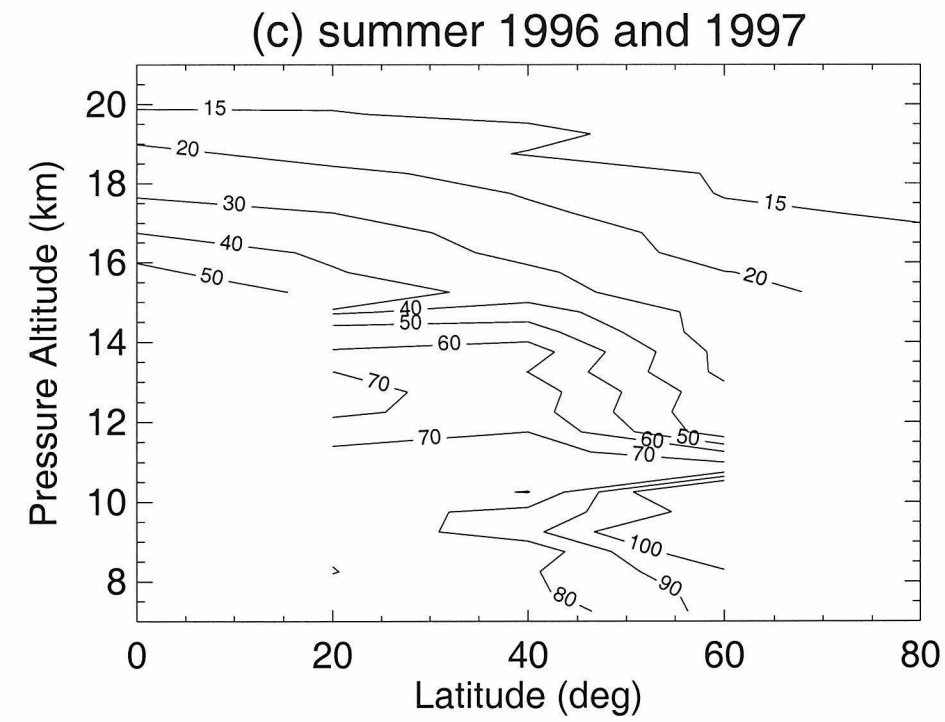
(c) summer 1996 and 1997
Pressure Altitude (km)
20
18
16
14
12
10
8
0
20
40
60
80
Latitude (deg)
15
20
30
40
50
60
70
80
90
100

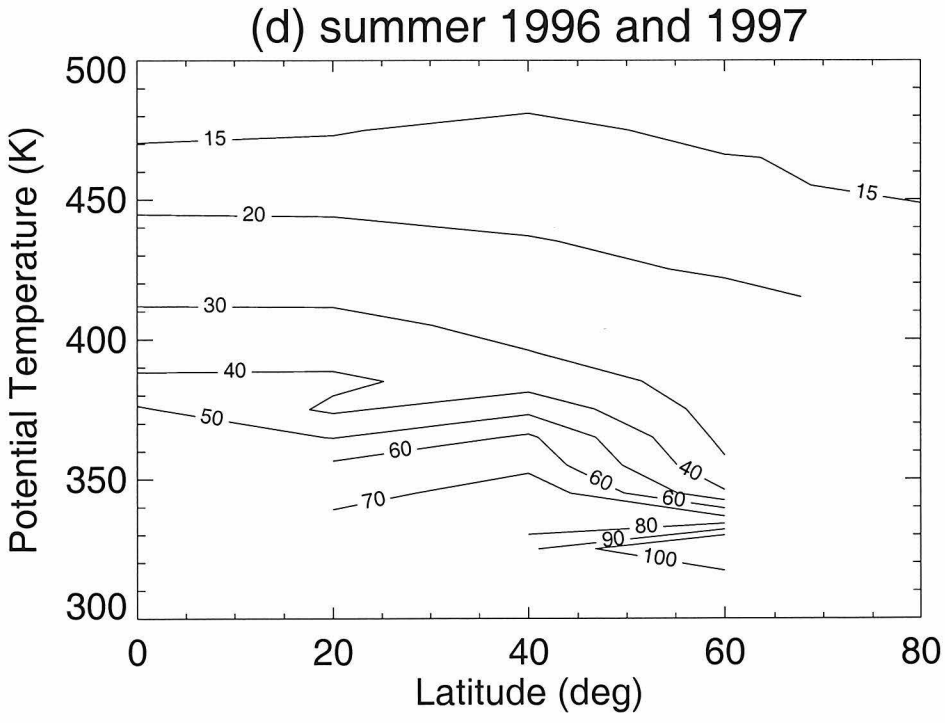
(d) summer 1996 and 1997
Potential Temperature (K)
500
450
400
350
300
0
20
40
60
80
Latitude (deg)
15
20
30
40
50
60
70
80
90
100

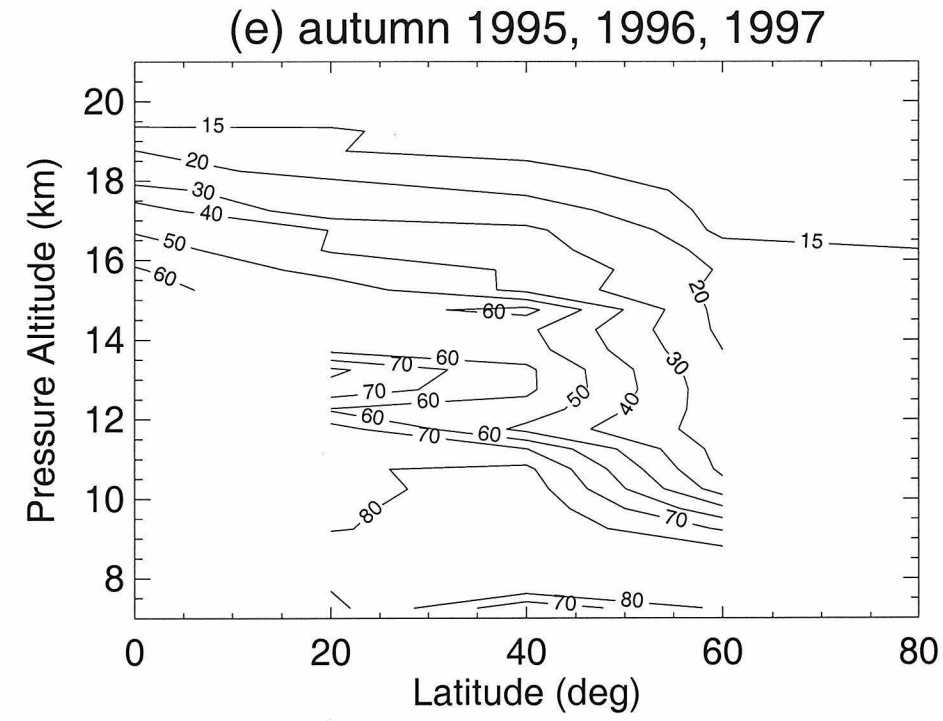
(e) autumn 1995, 1996, 1997
Pressure Altitude (km)
20
18
16
14
12
10
8
0
20
40
60
80
Latitude (deg)
15
20
30
40
50
60
70
80
90

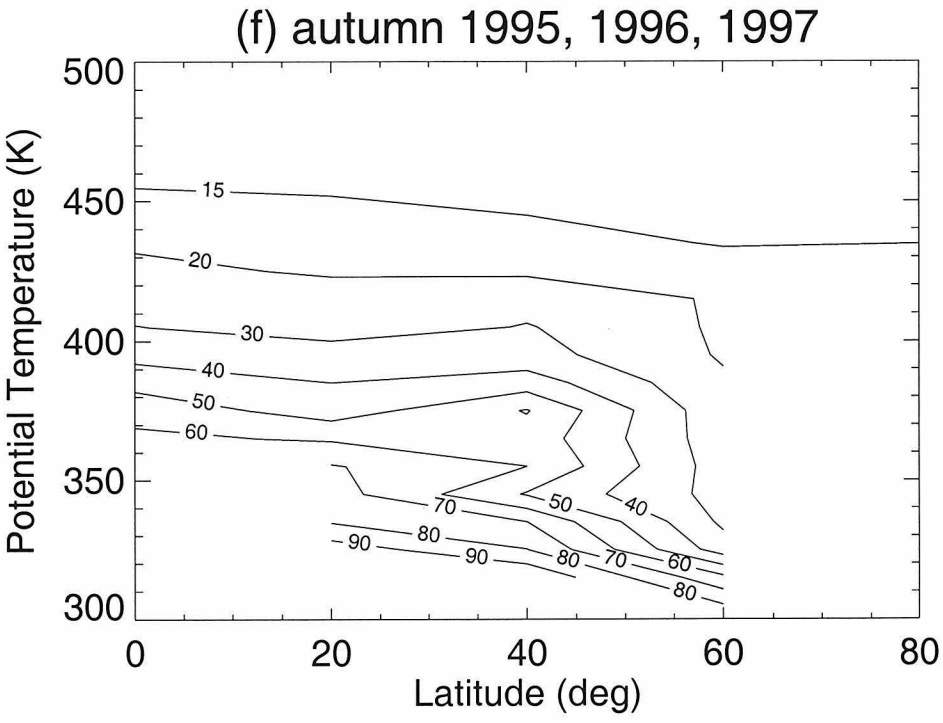
(f) autumn 1995, 1996, 1997
Potential Temperature (K)
500
450
400
350
300
0
20
40
60
80
Latitude (deg)
15
20
30
40
50
60
70
80
90

and the stratospheric "middleworld" (bounded above by the θ = 380 K isentrope and below by the extra-tropical tropopause) [Holton et al., 1995; Hoskins, 1991]. In the stratospheric middleworld, there is considerable variability in CO due to stratosphere-troposphere exchange at a wide range of latitudes, similar to previous observations [e.g., Lelieveld et al., 1997]. At high latitudes in the middleworld, CO isopleths are displaced to lower θ, possibly due to large-scale descent or a lack of upward transport across the tropopause. CO is less variable in the overworld than in the middleworld, although the 15 and 20 ppb isopleths are displaced to higher θ in summer due to greater production from CH_4 oxidation. CO isopleths are flatter in the overworld than in the middleworld, especially for 400 K < θ < 450 K between 0° and 40°N. The flat isopleths imply that quasi-horizontal mixing is fast relative to photochemical loss of CO for 400 K < θ < 450 K (altitudes below 20 km).

3.4 Analysis

We will first examine the tropical stratosphere. The stratospheric budget of CO is constrained by calculating the rates of reactions (3.1) and (3.2) using measured CO, CH_4, OH, temperature, and pressure, and model Cl and $O(^1D)$. Figure 7 shows tropical profiles of OH concentrations measured by the Harvard HO_x instrument on the ER-2. It is apparent that in the tropical stratosphere, the OH concentration is not strongly dependent on altitude. However, it is strongly dependent on solar zenith angle [e.g., Salawitch et al., 1994]. A quadratic fit of tropical OH data to solar zenith angle is used here to

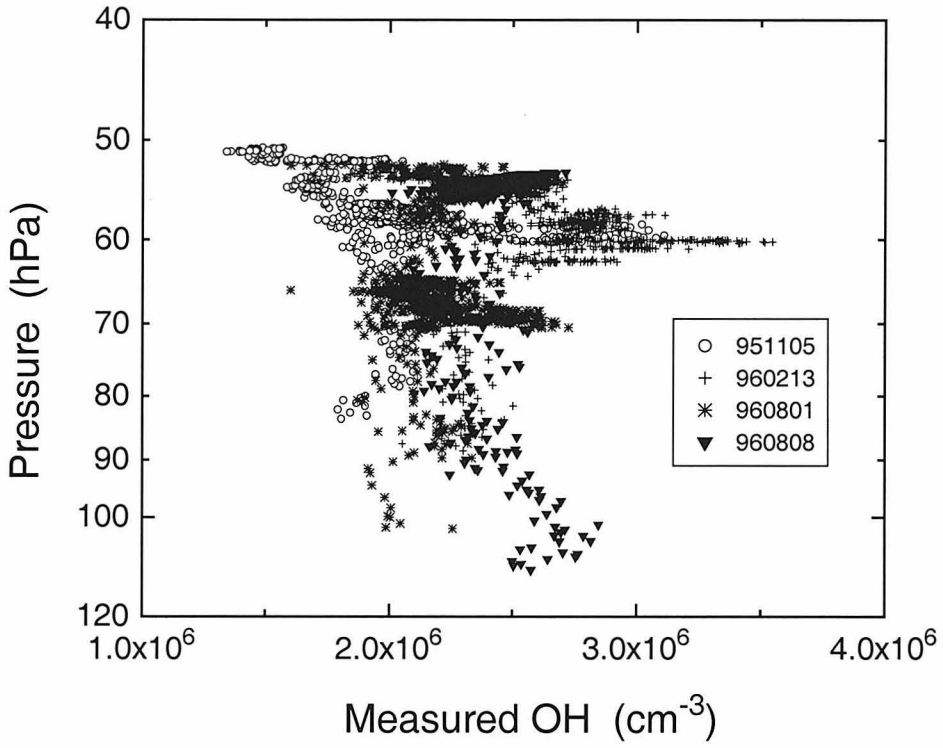

Figure 7. Tropical stratospheric OH measured by the Harvard HO_x instrument aboard the ER-2. Flight dates and latitude ranges are the same as in Figure 4.

calculate a 24-hour mean OH concentration of $8\pm3x10^5$ cm^{-3} in the tropical lower stratosphere. The lifetime of CO with respect to photochemical loss, τ, is inversely proportional to the concentration of OH:

$$\tau = 1/k_2[OH] \tag{3.3}$$

and is calculated to be approximately 100±35 days in the tropical lower stratosphere. Error bars are due to uncertainties of ±25% in the OH concentration and ±30% in k_2, the rate coefficient of (3.2) [W. B. DeMore, pers. comm.].

Twenty four-hour mean rates of CO production (3.1) and loss (3.2) in the tropics are shown in Figure 8. These rates were calculated from measured CO and CH_4, an OH concentration of $8x10^5$ cm^{-3}, 24-hour mean concentrations of Cl and $O(^1D)$ from a photochemical model [Salawitch et al., 1994], and rate coefficients from DeMore et al. [1997]. The photochemical model constrains H_2O, CH_4, O_3, NO_y, and Cl_y concentrations and particle surface area to tropical measurements by the ER-2, balloons, and satellites [e.g., Herman et al., 1998]. Modeled reaction rates (Figure 8) imply that the dominant chemical source of lower stratospheric CO is the CH_4 + OH reaction. Reactions of CH_4 with $O(^1D)$ and Cl increase in importance at higher altitudes. At 50 hPa, the measured CO mixing ratio is typically 10 to 15 ppb, close to the modeled steady-state balance between reactions (3.1) and (3.2). The steady-state mixing ratio increases with temperature due to the temperature-dependence of reaction (3.1).

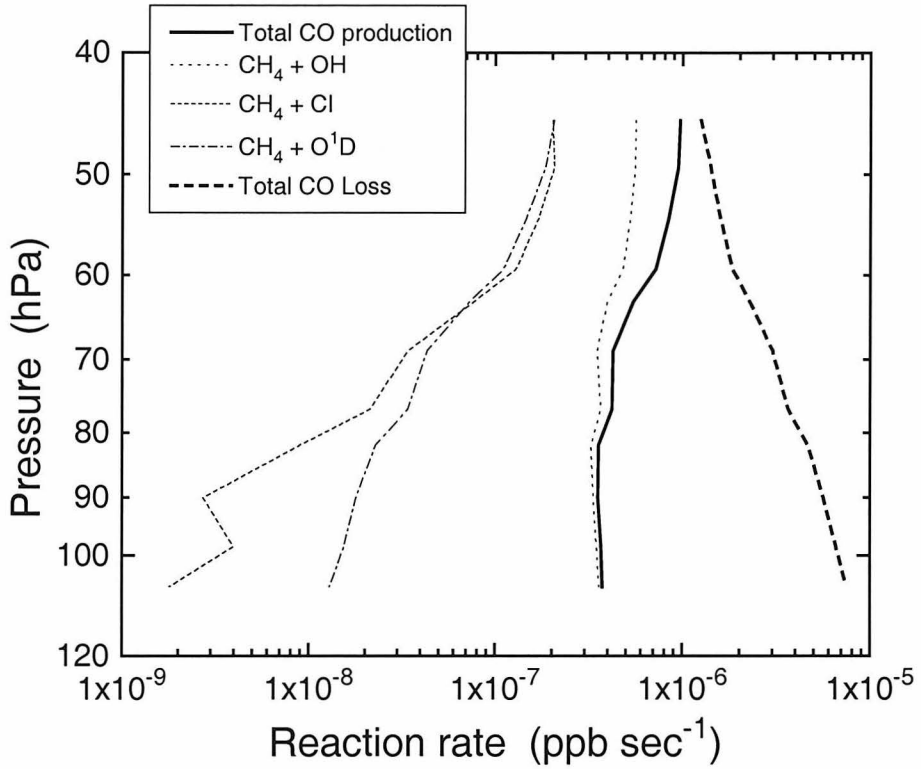

Figure 8. Annual average CO production and loss rates in the tropics. The rates were calculated from mean measured profiles of CO and CH_4, 24-hour mean profiles of Cl and $O(^1D)$ from a photochemical model [*Salawitch et al.*, 1994], and 24-hour mean OH concentration ($8x10^5$ cm^{-3}) inferred from an empirical relationship between measured OH and solar zenith angle.

We use a simple Lagrangian photochemical box model of tropical ascent to test the consistency of the measured concentrations of CO and OH, rate coefficients, and calculated ascent rates. The model includes diabatic heating and photochemical production and loss of CO:

$$Q\frac{\partial \chi}{\partial \theta} = -L\chi + P \tag{3.4}$$

where Q is the diabatic heating rate (equivalent to ascent rate in isentropic coordinates), χ is the CO concentration, loss L is $1/\tau$, production P is the rate of (3.1), and each term is parameterized as a function of θ (using the annual mean tropical relationship between θ and pressure). Q is the mass-balanced, annual mean tropical heating rate calculated from a radiative heating model, with typical uncertainties of ±60% at pressures greater than 50 hPa [Rosenlof, 1995]. Reaction rate coefficients are from DeMore et al. [1997]. In determining the abundance of tropical CO, photochemical loss dominates entrainment of extra-tropical air, so we neglect entrainment (the results are changed less than 5% by this approximation). The solution of (3.4) is superimposed on the tropical CO data in Figure 4b, with a boundary condition of 58 ppb CO at θ = 370 K. The excellent agreement indicates a high level of consistency among measured CO and OH concentrations, rate coefficients for (3.1) and (3.2), and the diabatic heating rates. The dashed lines in Figure 4b represent the total uncertainty in the model calculation (±1 st. dev.), including uncertainties in each term of (3.4) added in quadrature. The level of agreement between modeled and measured CO suggests that the true uncertainties are

considerably smaller. However, we cannot rule out the possibility that errors partially cancel.

As mentioned earlier, the flat isopleths of CO in the overworld suggest rapid quasi-horizontal mixing at altitudes below 20 km. We will now look at this phenomenon in greater detail. During the 960129 mid-latitude flight of the ER-2, there was a constant-altitude flight leg at 14.9 km ($380 < \theta < 385$ K) with H_2O mixing ratios less than 4 parts per million. Air this dry must have entered the stratosphere at the tropical tropopause [Hintsa et al., 1994]. ALIAS measured highly correlated mixing ratios of CO and N_2O on this flight leg, as shown in Figure 9. This CO *vs.* N_2O correlation is very linear and is different from the typical mid-latitude correlation, which suggests that these data form a mixing line. The data with the greatest tropical character have approximately 41 ppb CO and 300 ppb N_2O at $\theta = 381$ K. Extrapolating to the tropical end-member (315 ppb N_2O) yields 52 ppb CO. At 14.9 km altitude, photochemical loss of N_2O is negligible, so this air parcel is a mixture of young tropical air and photochemically aged mid-latitude air which has been transported through the stratosphere by the Brewer-Dobson circulation. The end-member CO mixing ratio (52 ppb) is indistinguishable from tropical CO (49.5±2 ppb) on the 381 K isentropic surface, indicating extremely rapid transport from the tropics to mid-latitudes.

We can generalize about quasi-horizontal mixing by comparing annual and seasonal mean CO profiles at different latitudes. Figure 10 shows mean stratospheric CO profiles in the annual mean, winter, and summer (binned by θ and latitude as in Figure 6). The mid-latitude and tropical profiles are very

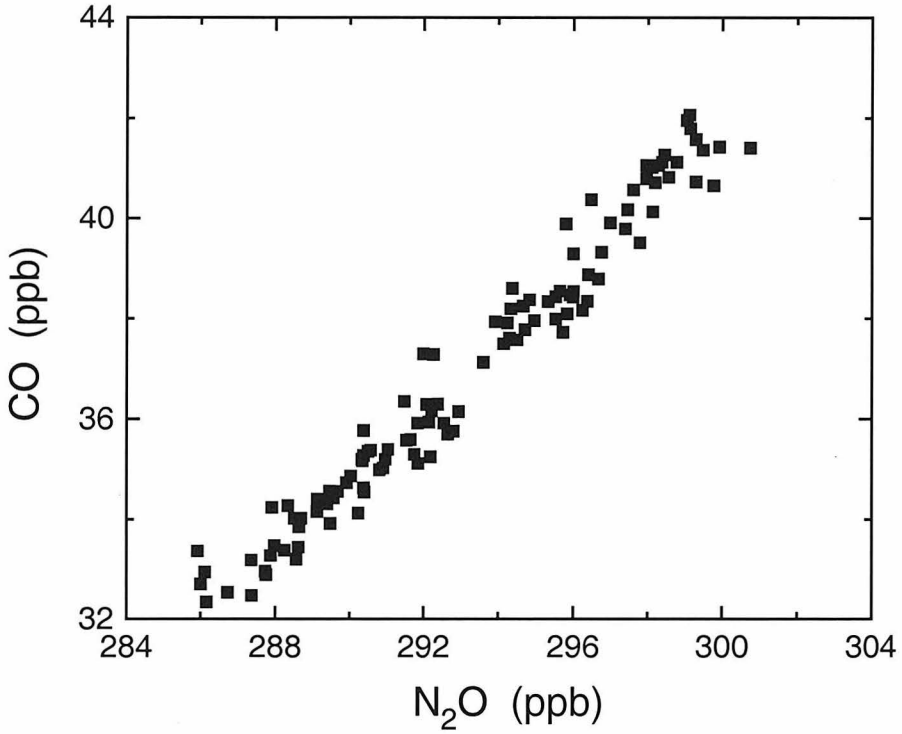

Figure 9. Measured CO *vs.* N_2O from a constant-altitude flight leg (14.9 km, 122-3 hPa, $380 < \theta < 385$ K) during the 960129 mid-latitude flight of the ER-2. This is a mixing line with a tropical end-member of 52 ppb CO and 315 ppb N_2O.

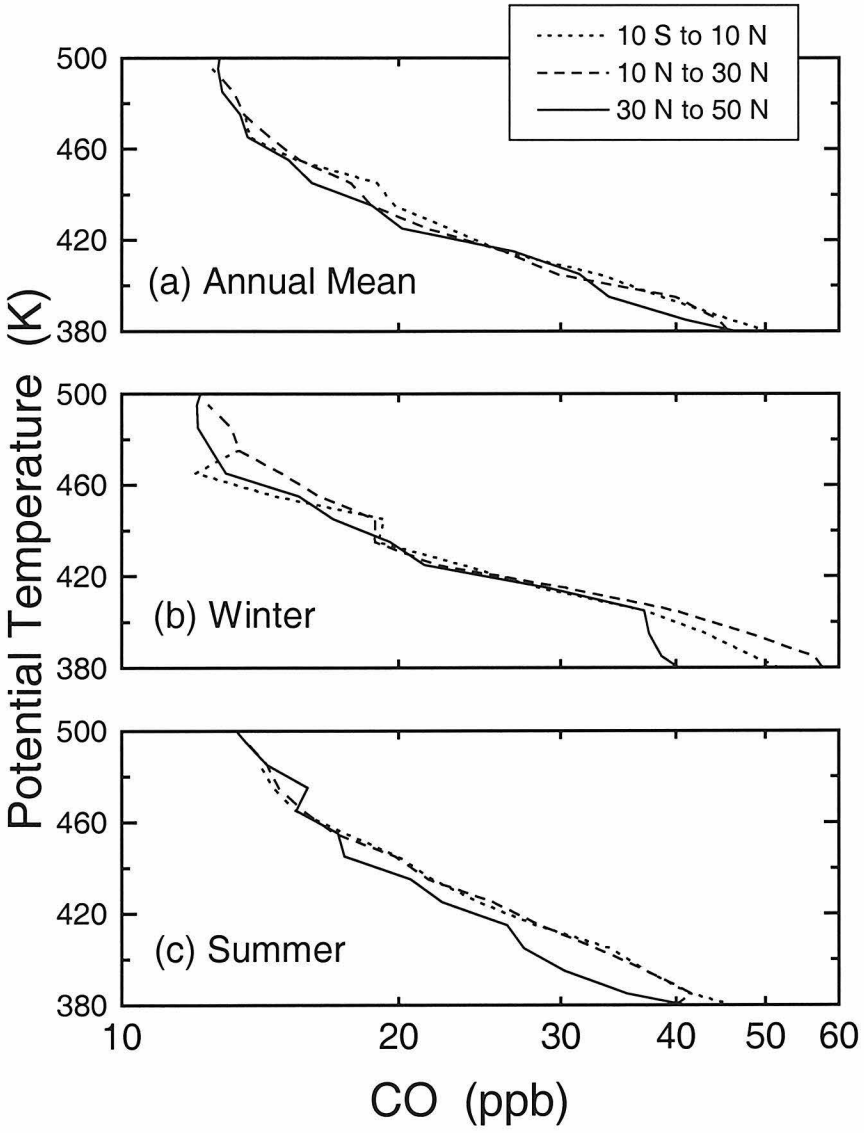

Figure 10. Mean profiles of measured CO in the stratospheric overworld, binned by latitude and potential temperature: (a) annual mean (57 flights), (b) winter (7 flights), (c) summer (21 flights).

similar due to rapid mixing. The annual mean chemical loss time scale corresponding to the difference between mid-latitude and tropical CO at constant θ is less than one month (400 K < θ < 450 K). This time scale is significantly shorter than independent estimates for quasi-horizontal transport from tropics to mid-latitudes [e.g., Boering et al., 1995; Boering et al., 1996; Hintsa et al., 1994], and suggests that not all of the transport is adiabatic. Considering the large vertical gradient of CO, vertical eddy diffusion at mid-latitudes probably plays a significant role. The tropical and mid-latitude CO profiles are more similar in winter than in summer, which is consistent with faster quasi-horizontal mixing in winter [e.g., Chen et al., 1994; Waugh, 1996].

3.5 Summary

In this paper, we have described the distribution of CO in the upper troposphere and lower stratosphere measured by ALIAS from October 1995 through September 1997. In the upper troposphere, CO has a seasonal cycle with a maximum in autumn and winter, and a minimum in spring and summer. During summer in Alaska, however, upper tropospheric CO is elevated due to lofting associated with forest fires. Over the central tropical Pacific Ocean, upper tropospheric CO mixing ratios are 60±5 ppb with little seasonal variation. In the tropical lower stratosphere, CO decreases as potential temperature increases, with little seasonal variation. The tropical stratospheric correlations of CO with θ and with O_3 appear to be robust features of the atmosphere.

A simple Lagrangian box model reproduces the measured tropical profile of CO with a high degree of accuracy, demonstrating a strong level of consistency between tropical ascent rates, measured concentrations of CO and OH, and the rate coefficients for reactions (3.1) and (3.2). Contour plots of CO have flat isopleths at potential temperatures between 400 and 450 K (altitudes below 20 km) due to rapid mixing between the tropical and mid-latitude stratosphere. This mixing transports a large volume of tropical air to the mid-latitude overworld. Since this air has only recently entered the stratosphere, it has relatively large concentrations of CO and potentially other reactive species that could affect mid-latitude stratospheric O_3 abundances.

Acknowledgments

We thank J. P. Pinto and S. C. Wofsy for helpful discussions; B. L. Gary for providing tropopause heights; E. J. Hintsa and E. M. Weinstock for H_2O data; K. H. Rosenlof for providing tropical heating rates; G. J. Flesch, L. Kroll, K. Modarress, and M. Tuchscherer for laboratory and field support of the ALIAS instrument; the ER-2 pilots and crew; and A. E. Kulawik for computational assistance. This work was supported by NASA's Upper Atmospheric Research Program (UARP) and the Atmospheric Effects of Aviation Project (AEAP). Part of the research described in this paper was carried out by the Jet Propulsion Laboratory, California Institute of Technology, under a contract with the National Aeronautics and Space

Administration. Division of Geological and Planetary Sciences, California Institute of Technology, Contribution 5764.

BIBLIOGRAPHY

Anderson, B. E., J. E. Collins, G. W. Sachse, G. W. Whiting, D. R. Blake, and F. S. Rowland, AASE-II Observations of Trace Carbon Species Distributions in the Mid to Upper Troposphere, *Geophys. Res. Lett., 20,* 2539-42, 1993.

Andreae, M. O., et al., Influence of Plumes from Biomass Burning on Atmospheric Chemistry over the Equatorial and Tropical South Atlantic during CITE-3, *J. Geophys. Res., 99,* 12,793-808, 1994.

Avallone, L. M., and M. J. Prather, Photochemical evolution of ozone in the lower tropical stratosphere, *J. Geophys. Res., 101,* 1457-61, 1996.

Boering, K. A., E. J. Hintsa, S. C. Wofsy, J. G. Anderson, B. C. Daube, Jr., A. E. Dessler, M. Loewenstein, M. P. McCormick, J. R. Podolske, E. M. Weinstock, and G. K. Yue, Measurements of stratospheric carbon dioxide and water vapor at northern midlatitudes: Implications for troposphere-to-stratosphere transport, *Geophys. Res. Lett., 22,* 2737-40, 1995.

Boering, K. A., S. C. Wofsy, B. C. Daube, H. R. Schneider, M. Loewenstein, J. R. Podolske, and T. J. Conway, Stratospheric Mean Ages and Transport Rates from Observations of Carbon Dioxide and Nitrous Oxide, *Science, 274,* 1340-3, 1996.

Bregman, A., F. Arnold, V. Bürger, H. Fischer, J. Lelieveld, B. A. Scheeren, J. Schneider, P. C. Siegmund, J. Ström, A. Waibel, and W. M. F. Wauben, In

Situ Trace Gas and Particle Measurements in the Summer Lower Stratosphere during STREAM II: Implications for O_3 Production, *J. Atmos. Chem., 26,* 275-310, 1997.

Chen, P., J. R. Holton, A. O'Neill, and R. Swinbank, Isentropic mass exchange between the tropics and extratropics in the stratosphere, *J. Atmos. Sci., 51,* 3006-18, 1994.

Crutzen, P. J., Ozone in the troposphere, Chapter 10 in *Composition, Chemistry, and Climate of the Atmosphere*, H. B. Singh, ed., 349-93, Van Nostrand Reinhold, New York, 1995.

DeMore, W. B., S. P. Sander, D. M. Golden, R. F. Hampson, M. J. Kurylo, C. J. Howard, A. R. Ravishankara, C. E. Kolb, and M. J. Molina, Chemical Kinetics and Photochemical Data for Use in Stratospheric Modeling, *JPL Publication 97-4,* Jet Propulsion Laboratory, Pasadena, CA, 1997.

Denning, R. F., S. L. Guidero, G. S. Parks, and B. L. Gary, Instrument description of the airborne Microwave Temperature Profiler, *J. Geophys. Res., 94, 16,757-65,* 1989.

Fishman, J., and P. J. Crutzen, The origin of ozone in the troposphere, *Nature, 274,* 855-8, 1978.

Gunson, M. R., M. M. Abbas, M. C. Abrams, M. Allen, L. R. Brown, T. L. Brown, A. Y. Chang, A. Goldman, F. W. Irion, L. L. Lowes, E. Mahieu, G. L. Manney, H. A. Michelsen, M. J. Newchurch, C. P. Rinsland, R. J.

Salawitch, G. P. Stiller, G. C. Toon, Y. L. Yung, and R. Zander, The Atmospheric Trace Molecule Spectroscopy (ATMOS) experiment: Deployment on the ATLAS space shuttle missions, *Geophys. Res. Lett., 23,* 2333-6, 1996.

Harriss, R. C., G. W. Sachse, J. E. Collins, L. Wade, K. B. Bartlett, R. W. Talbot, E. V. Browell, L. A. Barrie, G. F. Hill, and L. G. Burney, Carbon monoxide and methane over Canada: July-August 1990, *J. Geophys. Res., 99,* 1659-69, 1994.

Harriss, R. C., G. W. Sachse, G. F. Hill, L. Wade, K. B. Bartlett, J. E. Collins, L. P. Steele, and P. C. Novelli, Carbon Monoxide and Methane in the North American Arctic and Subarctic: July-August 1988, *J. Geophys. Res., 97,* 16,589-99, 1992.

Herman, R. L., D. C. Scott, C. R. Webster, R. D. May, E. J. Moyer, R. J. Salawitch, Y. L. Yung, G. C. Toon, B. Sen, J. J. Margitan, K. H. Rosenlof, H. A. Michelsen, J. W. Elkins, Tropical Entrainment Time Scales Inferred from Stratospheric N_2O and CH_4 Observations, submitted to *Geophys. Res. Lett.*, 1998.

Hintsa, E. J., E. M. Weinstock, A. E. Dessler, J. G. Anderson, M. Loewenstein, and J. R. Podolske, SPADE H_2O measurements and the seasonal cycle of stratospheric water vapor, *Geophys. Res. Lett., 21,* 2559-62, 1994.

Hipskind, R. S., G. L. Gregory, G. W. Sachse, G. F. Hill, and E. F. Danielson, Correlations Between Ozone and Carbon Monoxide in the Lower

Stratosphere, Folded Tropopause, and Maritime Troposphere, *J. Geophys. Res., 92,* 2121-30, 1987.

Holton, J. R., P. H. Haynes, M. E. McIntyre, A. R. Douglass, R. B. Rood, and L. Pfister, Stratosphere-Troposphere Exchange, *Rev. Geophys., 33,* 403-39, 1995.

Hoor, P., R. Konigstedt, U. Parchtka, F. G. Wienhold, and H. Fischer, Measurements of CO in the Arctic Lower Stratosphere During Winter 1996/7, submitted to *Chemosphere*, 1998.

Hoskins, B. J., Towards a PV-theta view of the general circulation, *Tellus, Ser. A., 43,* 27-35, 1991.

Lelieveld, J., B. Bregman, F. Arnold, V. Bürger, P. J. Crutzen, H. Fischer, A. Waibel, P. Siegmund, P. F. J. van Velthoven, Chemical perturbation of the lowermost stratosphere through exchange with the troposphere, *Geophys. Res. Lett., 24,* 603-6, 1997.

Levy, H. II, Normal atmosphere: Large radical and formaldehyde concentrations predicted, *Science, 173,* 141-3, 1971.

Logan, J. A., M. J. Prather, S. C. Wofsy, and M. B. McElroy, Tropospheric Chemistry: A Global Perspective, *J. Geophys. Res., 86,* 7210-54, 1981.

May, R. D., Open-Path Near-Infrared Tunable Diode Laser Spectrometer for Atmospheric Measurements of H_2O, submitted to *J. Geophys. Res.*, 1998.

May, R. D., and C. R. Webster, Data processing and calibration for tunable diode laser harmonic absorption spectrometers, *J. Quant. Spectrosc. Radiat. Transfer, 49,* 335-347, 1993.

Murphy, D. M., D. W. Fahey, M. H. Proffitt, S. C. Liu, K. R. Chan, E. S. Eubank, S. R. Kawa, and K. K. Kelly, Reactive Nitrogen and Its Correlation With Ozone in the Lower Stratosphere and Upper Troposphere, *J. Geophys. Res., 98,* 8751-73, 1993.

Pinto, J. P., Y. L. Yung, D. Rind, G. L. Russell, J. A. Lerner, J. E. Hansen, and S. Hameed, A General Circulation Model Study of Atmospheric Carbon Monoxide, *J. Geophys. Res., 88,* 3691-702, 1983.

Pressman, J., and P. Warneck, The stratosphere as a chemical sink for carbon monoxide, *J. Atm. Sci., 27,* 155-63, 1970.

Proffitt, M. H., and R. J. McLaughlin, Fast-response dual-beam UV-absorption ozone photometer suitable for use on stratospheric balloons, *Rev. Sci. Instrum., 54,* 1719-28, 1983.

Reid, G. C., and K. S. Gage, The tropical tropopause over the western Pacific: wave driving, convection, and the annual cycle, *J. Geophys. Res., 101,* 21,233-41, 1996.

Ridley, B. A., E. L. Atlas, J. G. Walega, G. L. Kok, T. A. Staffelbach, J. P. Greenberg, F. E. Grahek, P. G. Hess, and D. D. Montzka, Aircraft measurements made during the spring maximum of ozone over Hawaii:

Peroxides, CO, O_3, NO_y, condensation nuclei, selected hydrocarbons, halocarbons, and alkyl nitrates between 0.5 and 9 km altitude, *J. Geophys. Res., 102,* 18,935-61, 1997.

Robinson, E., D. Clark, and W. Seiler, The Latitudinal Distribution of Carbon Monoxide Across the Pacific from California to Antarctica, *J. Atmos. Chem., 1,* 137-49, 1984.

Rosenlof, K. H., Seasonal cycle of the residual mean meridional circulation in the stratosphere, *J. Geophys. Res., 100,* 5173-91, 1995.

Salawitch, R. J., et al., The diurnal variation of hydrogen, nitrogen, and chlorine radicals: implications for the heterogeneous production of HNO_2, *Geophys. Res. Lett., 21*, 2551-4, 1994.

Scott, S. G., T. P. Bui, K. R. Chan, and S. W. Bowen, The Meteorological Measurement System on the NASA ER-2 aircraft, *J. Atmos. and Oceanic Technol., 7,* 525-40, 1990.

Seiler, W., and J. Fishman, The Distribution of Carbon Monoxide and Ozone in the Free Troposphere, *J. Geophys. Res., 86,* 7255-65, 1981.

Tuck, A. F., et al., The Brewer-Dobson circulation in the light of high altitude *in situ* aircraft observations, *Quart. J. Roy. Met. Soc., 123,* 1-69, 1997.

Volk, C. M., J. W. Elkins, D. W. Fahey, R. J. Salawitch, G. S. Dutton, J. M. Gilligan, M. H. Proffit, M. Loewenstein, J. R. Podolske, K. Minschwaner,

J. J. Margitan, and K. R. Chan, Quantifying transport between the tropical and mid-latitude lower stratosphere, *Science, 272,* 1763-8, 1996.

Waibel, A. E., H. Fischer, P. C. Siegmund, B. Lee, F. G. Wienhold, P. J. Crutzen, J. Lelieveld, and J. Strom, Highly elevated carbon monoxide concentrations in the upper troposphere and lowermost stratosphere at northern midlatitudes during STREAM II summer campaign in 1994, submitted to *Chemosphere*, 1998.

Waugh, D. W., Seasonal variation of isentropic transport out of the tropical stratosphere, *J. Geophys. Res., 101,* 4007-23, 1996.

Webster, C. R., R. D. May, C. A. Trimble, R. G. Chave, and J. Kendall, Aircraft (ER-2) laser infrared absorption spectrometer (ALIAS) for *in situ* stratospheric measurements of HCl, N_2O, CH_4, NO_2 and HNO_3, *Appl. Opt., 33,* 454-472, 1994.

Weinstock, E. M., E. J. Hintsa, J. G. Anderson, K. A. Boering, B. C. Daube, S. C. Wofsy, R. L. Herman, R. D. May, C. R. Webster, and T. P. Bui, Evaluation of the seasonal cycle of water vapor in the stratosphere from monthly average tropical tropopause temperatures using a CO photochemical clock, in preparation, 1998.

Weinstock, E. M., E. J. Hintsa, A. E. Dessler, J. F. Oliver, N. L. Hazen, J. N. Demusz, N. T. Allen, L. B. Lapson, and J. G. Anderson, A new fast response photofragment fluorescence hygrometer for use on the NASA

ER-2 and Perseus remotely piloted aircraft, *Rev. Sci. Instrum., 65,* 3544-54, 1994.

Wennberg, P. O., R. C. Cohen, N. L. Hazen, L. B. Lapson, N. T. Allen, T. F. Hanisco, J. F. Oliver, N. W. Lanham, J. N. Demusz, and J. G. Anderson, Aircraft-borne, laser-induced fluorescence instrument for the *in situ* detection of hydroxyl and hydroperoxyl radicals, *Rev. Sci. Instrum., 65,* 1858-76, 1994.

Yurganov, L. N., Seasonal cycles of carbon monoxide over the Arctic and Antarctic - total columns versus surface data, *Atmos. Res., 44,* 223-30, 1997.

Chapter 4

Intercomparisons

4.1 Introduction

The purpose of this chapter is to assess the quality of measurements of N_2O and CH_4 by ALIAS II and of predictions by the Caltech-JPL Two-Dimensional (2D) atmospheric photochemistry model. It is difficult to determine the absolute accuracy of tracer measurements because environmental conditions during flight are harsh compared to those in the laboratory where the instrument is calibrated. Another complication is the natural variability of the atmosphere. Measurements taken at a given time and place may bear little similarity to measurements taken elsewhere. Atmospheric eddies cause considerable variability in vertical profiles of tracers. However, within a region of rapid quasi-horizontal mixing, the relationship between two long-lived species is expected to be nearly constant [Plumb and Ko, 1992]. N_2O and CH_4 are very long-lived relative to horizontal motions in the mid-latitude "surf zone" of the lower stratosphere (see Chapter 1), so their relationship at mid-latitudes is nearly the same regardless of location and has a high degree of statistical correlation (see Chapter 5). Such a relationship is called a "compact correlation" [Plumb and Ko, 1992]. Therefore, we can directly compare correlation plots of ALIAS II CH_4 *vs.* N_2O with measurements taken by other

instruments at different times. In this chapter, we will compare N_2O and CH_4 with other measurements and with model predictions. In both cases, we will first compare tracer profiles with simultaneous measurements and then compare tracer *vs.* tracer relationships.

4.2 Instrument Comparison

ALIAS II has flown six times in the last two years on the Observations from the Middle Stratosphere (OMS) balloon payload. The individual flight dates and locations are shown in Table 3 (Appendix II). On some of these flights, other instruments measured N_2O and CH_4 on the same payload or on the ER-2 aircraft flying nearby. Aboard the OMS balloon payload, there are simultaneous measurements of N_2O and CH_4 by the Argus instrument on 970214 and 970630 (yymmdd). Argus is a tunable diode laser spectrometer similar to ALIAS II, except that it has a closed sample cell connected to a pump [Podolske and Loewenstein, 1993]. On 960921 and 970630, the ER-2 aircraft flew close in space and time to the OMS balloon payload. N_2O is measured aboard the ER-2 by ALIAS [Webster et al., 1994], the Airborne Tunable Laser Absorption Spectrometer (ATLAS) [Podolske and Loewenstein, 1993] and the Airborne Chromatograph for Atmospheric Trace Species (ACATS) [Elkins et al., 1995]. CH_4 is measured aboard the ER-2 by ALIAS, ACATS, and is collected in canisters by the Whole Air Sampler (WAS) [Heidt et al., 1989] for laboratory analysis.

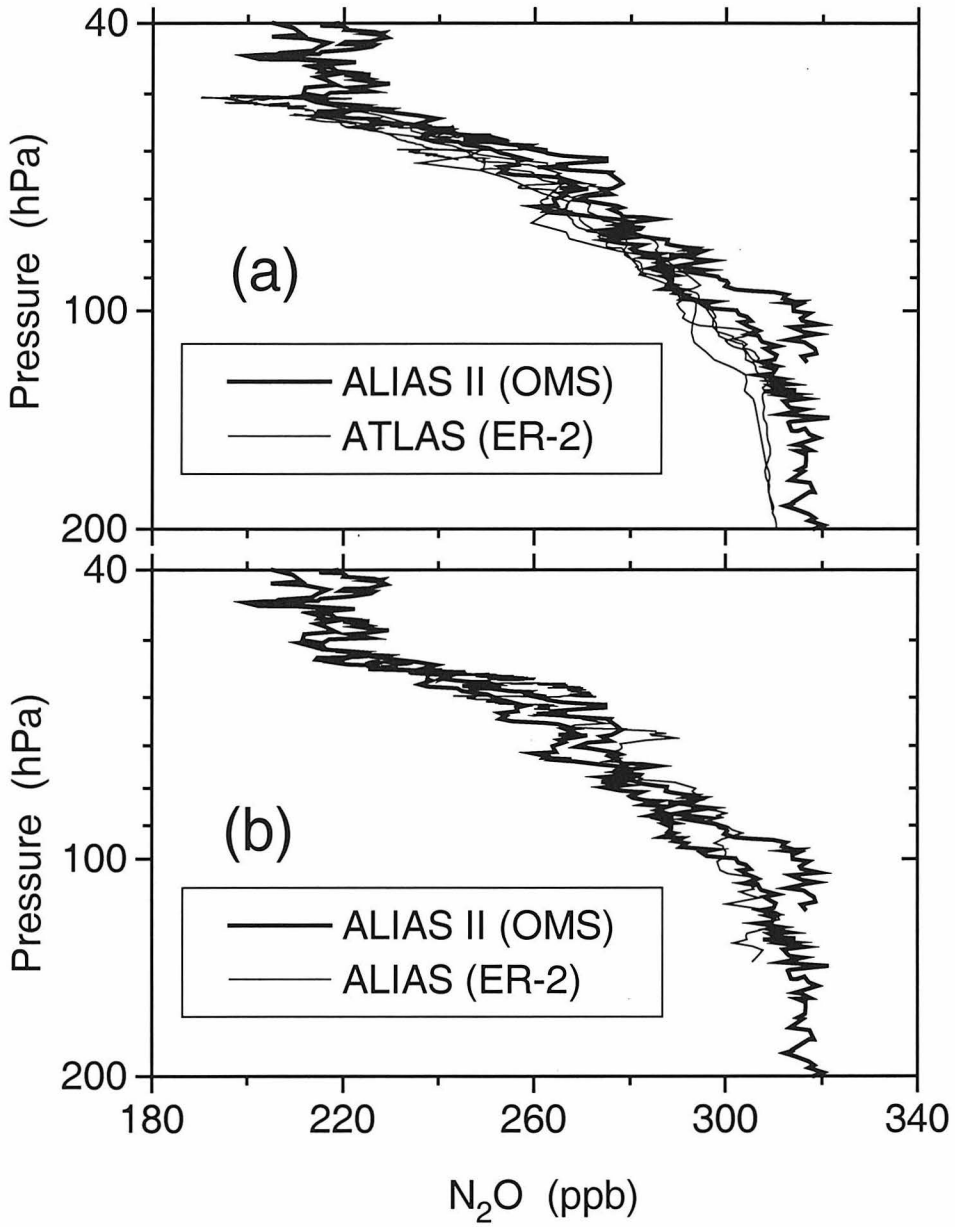

Figure 1. N_2O profiles measured on 960921 (yymmdd format) over New Mexico by balloon (OMS) and aircraft (ER-2) instruments: (a) ALIAS II and ATLAS, (b) ALIAS II and ALIAS.

We now compare vertical profiles of N_2O and CH_4 measured on the same day. Figure 1 shows N_2O profiles measured over New Mexico by ALIAS II, ALIAS, and ATLAS on 960921. Ascent and descent mixing ratios are different by approximately 5 to 10 parts per billion (ppb) in the ALIAS II measurements. The asymmetry between ascent and descent is likely an instrumental artifact due to thermal drifts within the electronics (see discussion of correlation plots below). There are also differences of 5 to 10 ppb between the three instruments: ALIAS N_2O is higher than ALIAS II, and ATLAS N_2O is lower. The differences between instruments suggest that N_2O measurements are accurate to 10 ppb (i.e., 3 to 5%) at best. All three instruments use the same measurement technique and are susceptible to similar systematic errors, but we will show later that measurements made on 970630 are in good agreement with data from two gas chromatographs (ACATS and WAS).

Figure 2 shows CH_4 profiles from the 960921 flight. There are differences between ascent and descent of approximately 40 to 50 ppb. In addition, ALIAS II CH_4 is systematically 100 ppb lower than ALIAS at pressures between 100 and 200 hPa. These pressures are high enough for significant pressure broadening of spectral lines, and temperatures are lowest here, so an inaccuracy in the temperature dependence of pressure broadening could cause this systematic difference (see equation 2.7). We intend to calibrate ALIAS II at low temperatures to see if this is the case.

On 970630, the OMS balloon and the ER-2 both made flights from Fairbanks, Alaska. This intercomparison is better than the previous one because more instruments aboard the ER-2 measured N_2O and CH_4, including

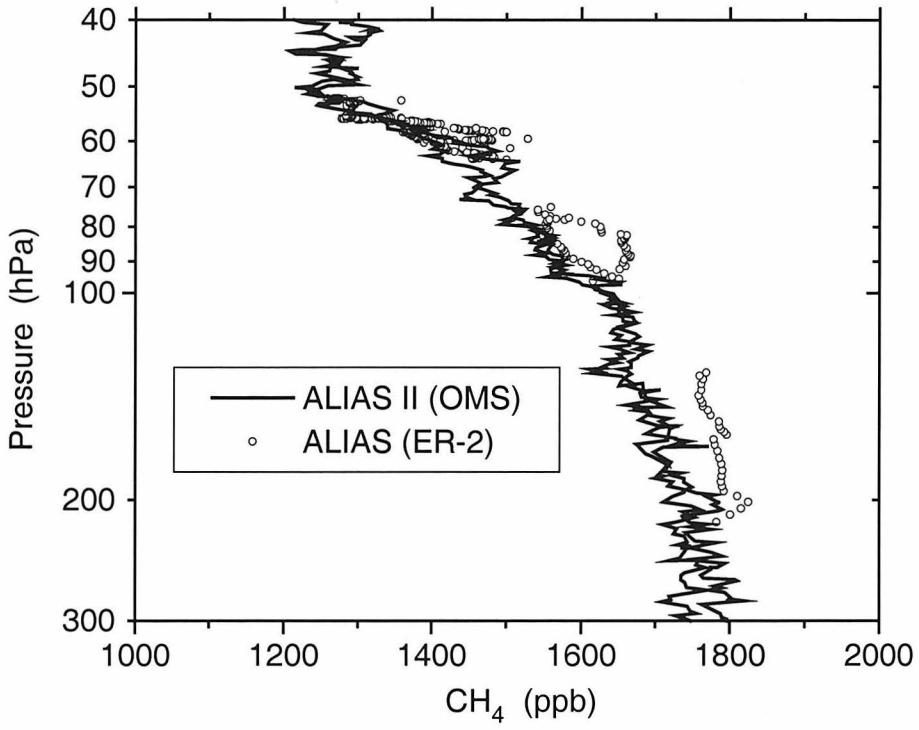

Figure 2. CH_4 profiles measured on 960921 (yymmdd format) over New Mexico by ALIAS II on a balloon payload (OMS) and ALIAS on an aircraft (ER-2).

two instruments that rely on gas chromatography: ACATS and WAS (whole air samples are analyzed for CH_4 in the laboratory using a gas chromatograph with flame ionization detection). Figure 3 shows N_2O profiles measured by ALIAS II, Argus, ALIAS, ATLAS, and ACATS on 970630. There is excellent agreement (to within 10 ppb) over the pressure range of 55 to 100 hPa, which suggests that both spectroscopic and chromatographic techniques are accurate. The ACATS outlier at 60 hPa may be caused by uncertainties in the timing of sample collection. At pressures greater than 100 hPa, ALIAS II data are very noisy. We believe that fluctuations in the optical alignment are the cause of this problem. At low pressures, ALIAS II and Argus are generally in good agreement, although Argus is systematically lower by about 10 ppb.

CH_4 profiles from 970630 are shown in Figure 4. The magnitude of variation between instruments and between ascent and descent is approximately 50 ppb. Both gas chromatographs are in good agreement with the spectroscopic instruments, which suggests again that both techniques are accurate. However, Argus CH_4 is lower than ALIAS II CH_4, and becomes even lower at higher altitudes. The cause of this discrepancy is not known.

As noted above, plots of one long-lived tracer *vs.* another are expected to exhibit a compact correlation within the mid-latitude lower stratosphere [Plumb and Ko, 1992]. We found that CH_4 and N_2O measured over New Mexico on 960921 (Figure 5) indeed show a compact correlation. Figure 5 is a plot of CH_4 *vs.* N_2O simultaneous measured by ALIAS II on the balloon and ALIAS on the ER-2. Figure 5 also shows data from the 960928 balloon flight

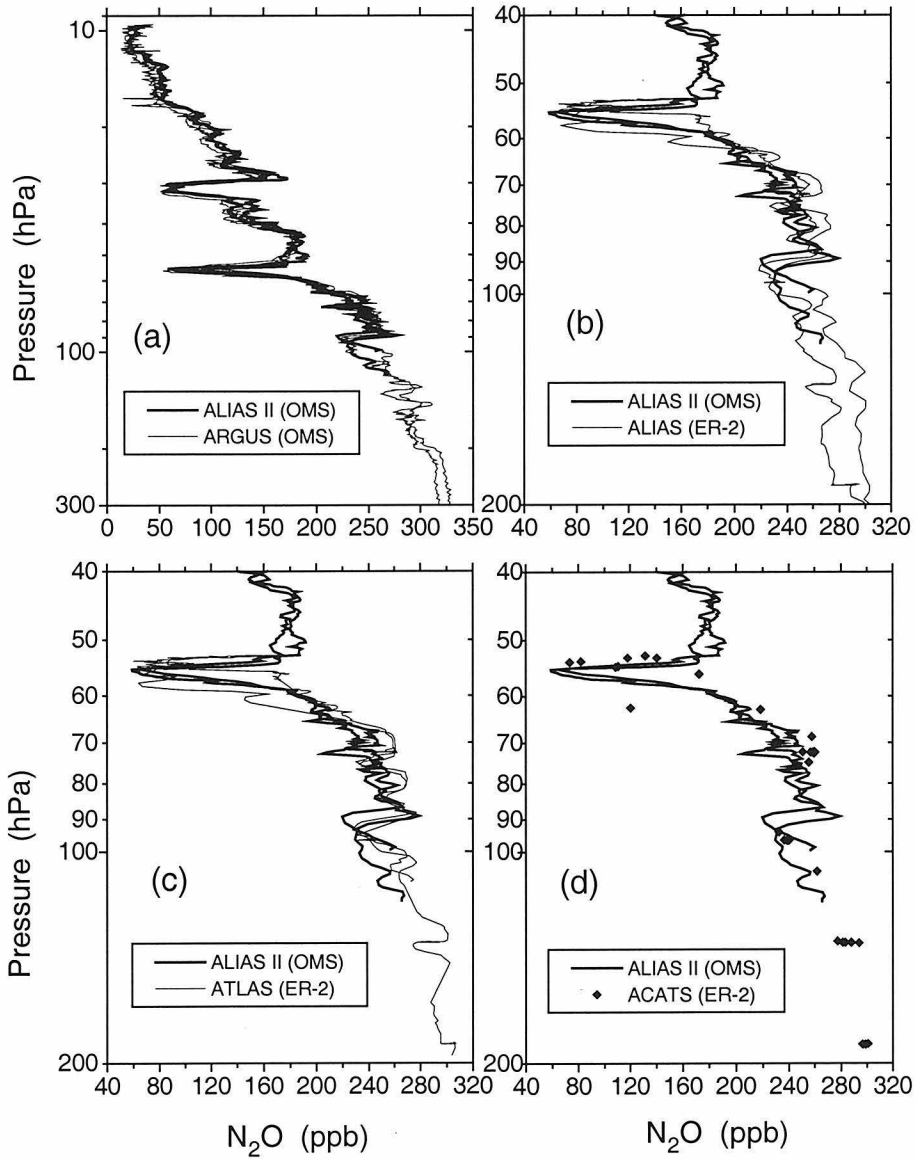

Figure 3. N_2O profiles measured on 970630 over Alaska by balloon (OMS) and aircraft (ER-2) instruments: (a) ALIAS II and Argus, (b) ALIAS II and ALIAS, (c) ALIAS II and ATLAS, (d) ALIAS II and ACATS.

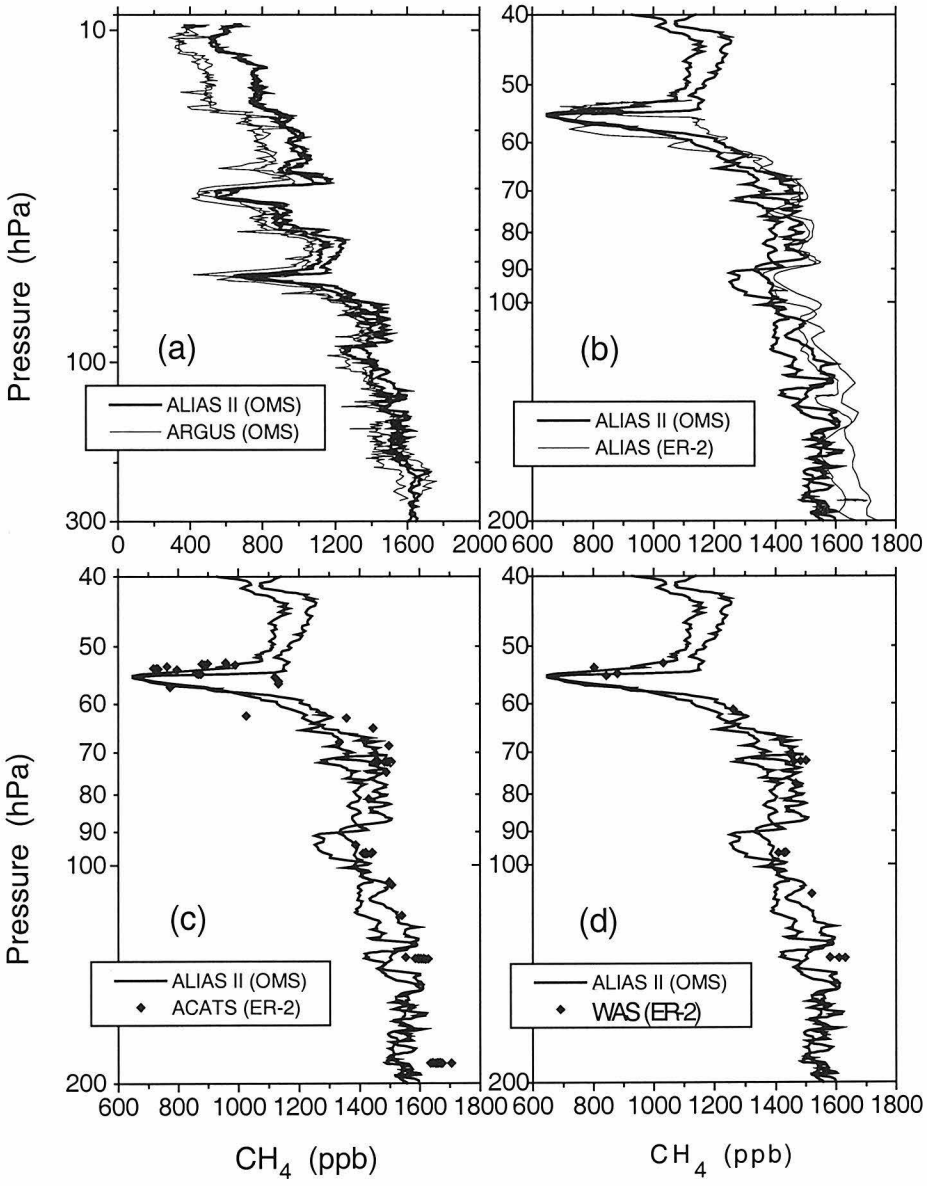

Figure 4. CH_4 profiles measured on 970630 over Alaska by balloon (OMS) and aircraft (ER-2) instruments: (a) ALIAS II and Argus, (b) ALIAS II and ALIAS, (c) ALIAS II and ACATS, (d) ALIAS II and WAS.

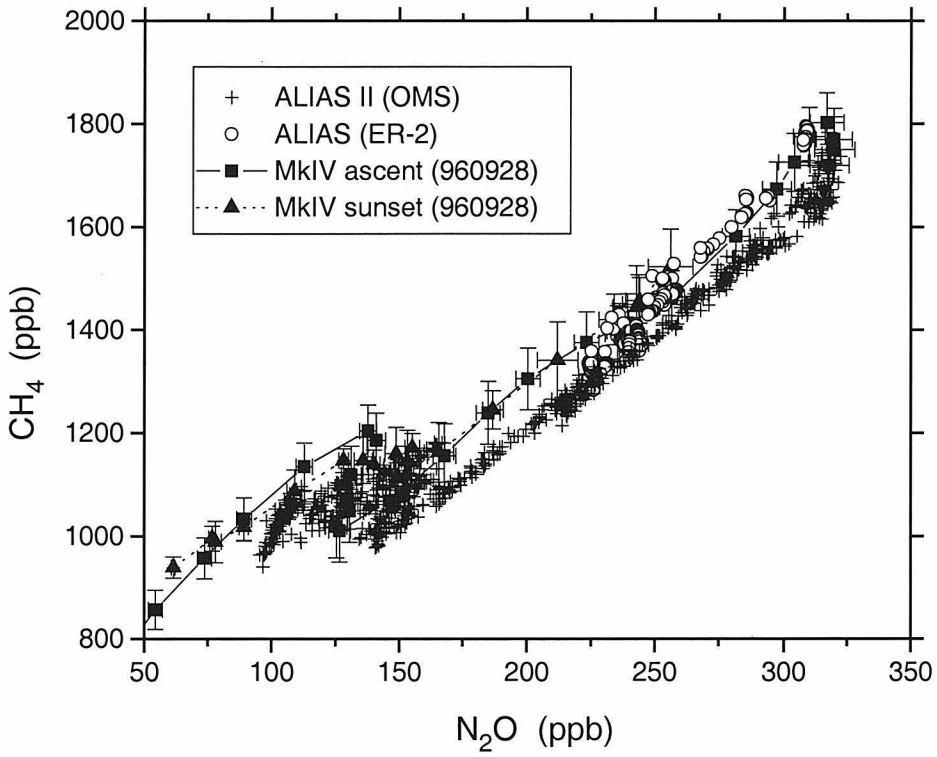

Figure 5. CH_4 *vs.* N_2O correlation plots of data measured over New Mexico: 960921 data from ALIAS II and ALIAS compared with 960928 data from MkIV. The ALIAS II data appear to be systematically different from the other two datasets.

of the MkIV interferometer, a solar occultation Fourier Transform Infrared Spectrometer [Toon, 1991], from the same location. Tropospheric data are found at the upper right corner of these plots (1700 ppb CH_4 and 315 ppb N_2O), and data from the middle stratosphere are at the lower left corners. Tracer mixing ratios do not necessarily show a monotonic decrease with altitude (see Figure 3, for instance). However, air parcels with less CH_4 and N_2O have experienced more photochemistry either through transport to higher altitudes where reaction rates are faster (see Chapter 1, Figures 3 and 5) or by remaining in the stratosphere longer. The compact correlation is the net result of slow photochemical destruction of CH_4 and N_2O and the large-scale circulation of the stratosphere (see Chapter 1).

From Figure 5, it is apparent that ALIAS and MkIV are in excellent agreement but that ALIAS II data are offset by either +10 ppb N_2O or -50 ppb CH_4. However, ALIAS II N_2O is systematically lower than ATLAS and ALIAS N_2O when correlated against another long-lived tracer, CO_2 (Figure 6). CO_2 is measured on both the OMS balloon platform and the ER-2 by nondispersive infrared photometers from Harvard [e.g., Boering et al., 1996]. These photometers measure CO_2 to ± 0.05 parts per million (ppm) precision and ± 0.1 ppm accuracy [A. E. Andrews, pers. comm.], which is less than 0.03% of the mixing ratio. Correlation plots of N_2O *vs.* CO_2 (Figure 6) and CH_4 *vs.* CO_2 (Figure 7) show systematic differences that exceed the uncertainty in the CO_2 measurements (the kink at the top of Figures 6 and 7 is due to the seasonal cycle of CO_2 propagating into the lower stratosphere). Therefore, these differences must be due to error in the N_2O and CH_4 measurements. As

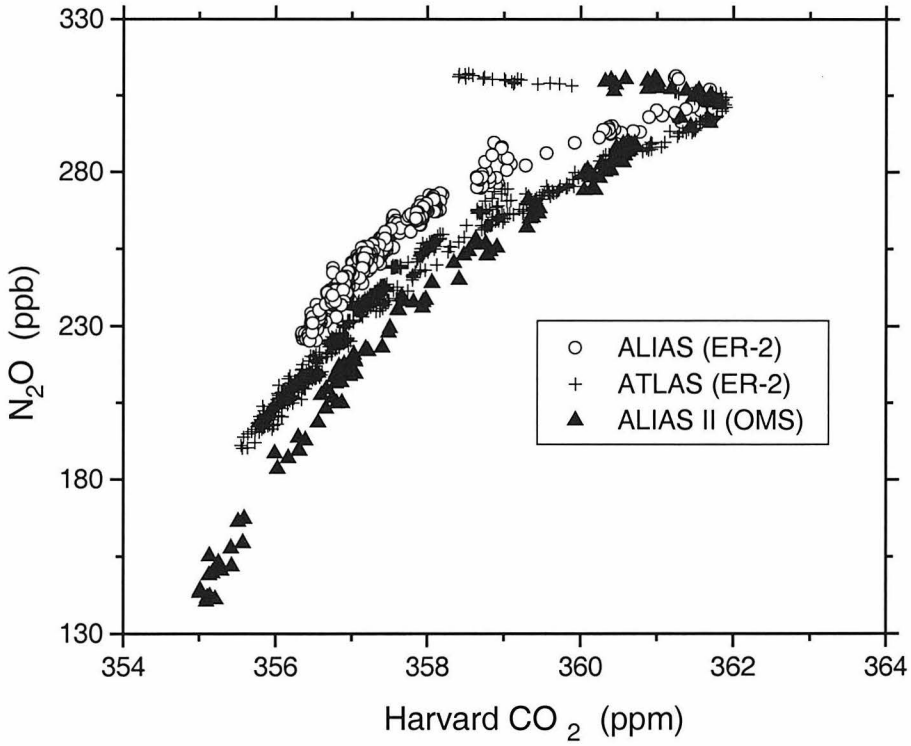

Figure 6. N_2O *vs.* CO_2 correlation plots of data measured over New Mexico on 960921. ALIAS II N_2O is similar to ATLAS N_2O at mixing ratios greater than 260 ppb, but is systematically lower than either ATLAS or ALIAS at mixing ratios less than 260 ppb.

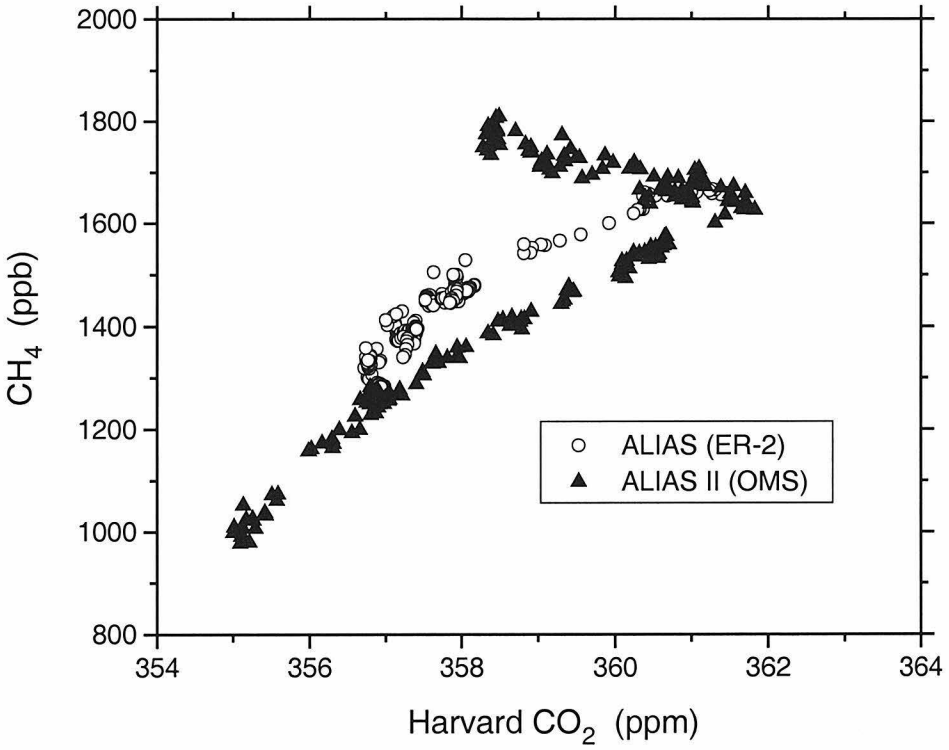

Figure 7. CH_4 *vs.* CO_2 correlation plots of data measured over New Mexico on 960921. The systematic CH_4 offset accounts for most of the difference in Figure 5.

shown in Figure 6, ALIAS II N_2O is in excellent agreement with ATLAS at mixing ratios greater than 260 ppb, but diverges from it at higher altitudes. Thus, N_2O cannot explain the offset in Figure 5. However, Figure 7 shows that ALIAS II CH_4 is systematically 100 to 120 ppb lower than ALIAS. Therefore, the offset in Figure 5 is largely due to systematically low CH_4 measured by ALIAS II.

The flight of 970630 from Fairbanks, Alaska, was particularly interesting because of the large variation in tracer mixing ratios (see Figures 3 and 4). This structure will be explained in detail in Chapter 5, but we now compare the correlation plots from the different instruments. Figure 8 shows the CH_4 *vs.* N_2O plots from 970630 measurements by ALIAS II, ALIAS, ATLAS (N_2O only), ACATS, and WAS (CH_4 only). ALIAS II has large scatter at 230 ppb < N_2O < 280 ppb (Figure 8a). The data close to the dashed line show some scatter, but are actually highly correlated structures that fall along several straight lines parallel to the dashed line. These data correspond to two layers of anomalously low N_2O and CH_4 mixing ratios observed at 55 and 30 hPa on 970630 (Figures 3 and 4). The lowest mixing ratios observed by the ER-2 instruments (ALIAS, ATLAS, ACATS, and WAS) occur in the lower layer at 55 hPa (Figures 3 and 4), and fall directly upon the dashed line in Figure 8. This dashed line represents a fit through observations of polar vortex air at altitudes below 23 km made by the Atmospheric Trace MOlecular Spectroscopy instrument (ATMOS) aboard the space shuttle in April, 1993 [Michelsen et al., 1998]. At 55 hPa, it is apparent that ALIAS has better precision than ALIAS II. However, at lower pressures (50 to 10 hPa),

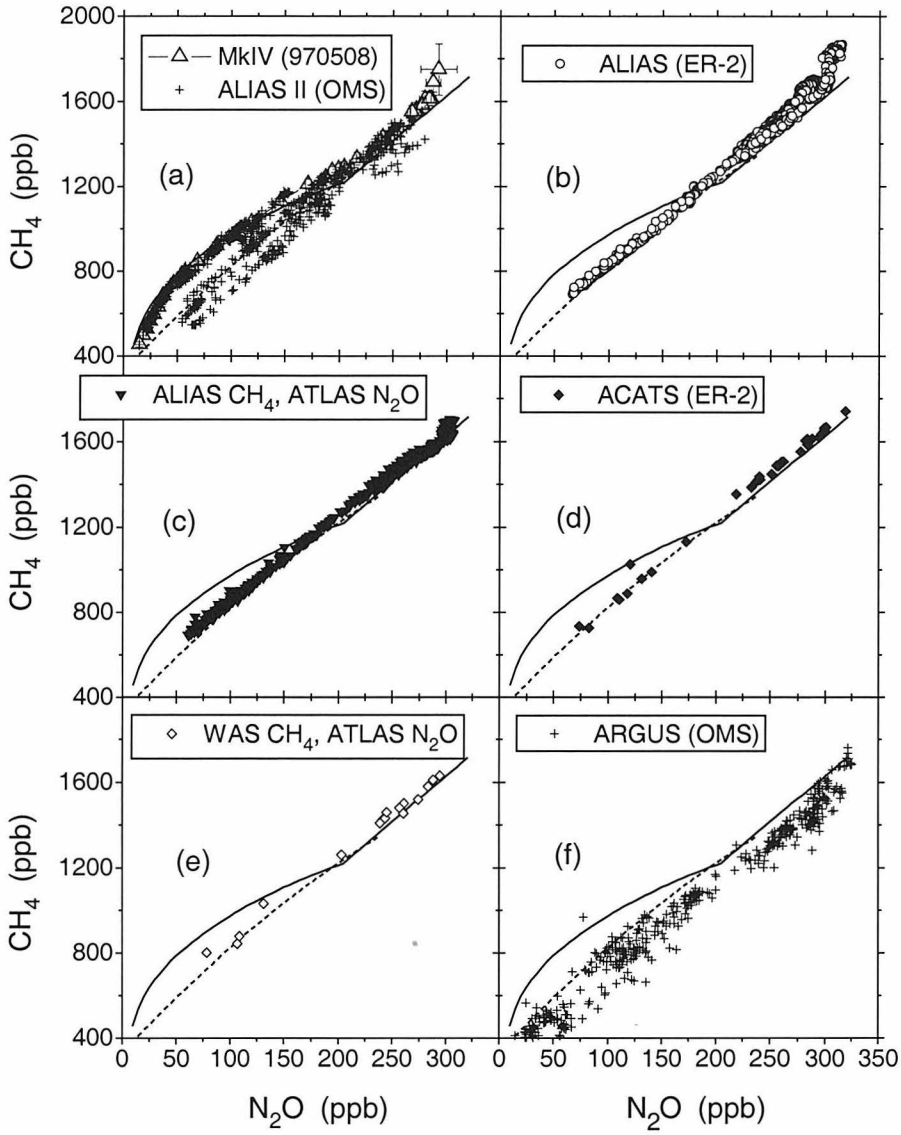

Figure 8. CH_4 *vs.* N_2O correlation plots from the balloon and ER-2 flights of 970630 in Alaska. Open squares with error bars are MkIV data from the 970508 balloon flight from the same location. Solid line is a fit to mid-latitude observations made in Nov., 1994, from the ATMOS instrument on the space shuttle [Michelsen et al., 1998]. Dashed line is a fit to polar vortex observations made in April, 1993, from ATMOS at altitudes below 23 km [ibid.]. This portion of the polar vortex has undergone substantial mixing with air outside the vortex (see Chapter 5).

the ALIAS II data are very compact and in excellent agreement with MkIV high-latitude data (Figure 8a).

To conclude, we have compared measurements of N_2O and CH_4 by ALIAS II with those of various different instruments on balloons, aircraft, and the space shuttle. The quality of ALIAS II data varies from flight to flight, but is best at pressures between 30 and 70 hPa in the middle and lower stratosphere. Over this pressure range, the estimated accuracy of ALIAS II N_2O and CH_4 is ±5%. At lower pressures, the accuracy is less certain, but ALIAS II is in excellent agreement with MkIV, especially for the high latitude flights. ALIAS II N_2O is also in excellent agreement with Argus N_2O, although the CH_4 measurements by these two instruments differ significantly. ALIAS II precision is typically ±3%, but there are differences between balloon ascent and descent that amount to 10 ppb N_2O and 50 ppb CH_4. In addition, there appears to be a systematic offset of -100 ppb CH_4 that affected the 960921 flight and most of the data near the tropopause on all flights. This offset may be related to temperature, and will be investigated in the future. The data analysis in Chapter 5 basically involves the difference between mid-latitude and tropical tracer profiles, so this offset is unimportant assuming that it did not change much between the mid-latitude and tropical flights.

4.3 Comparison with the Caltech-JPL 2D model

Models are the major predictive tools for assessments of future climate change. Thus it is important to compare our measurements of trace gases with

predictions of global atmospheric chemistry models. The Caltech-JPL 2D model is a zonal mean atmospheric model that has been developed to study atmospheric chemistry of the Earth and other planets. It has been applied to numerous terrestrial studies ranging from the impact of anthropogenic chlorine on stratospheric O_3 [Froidevaux et al., 1985] to the radiative and chemical effects of volcanic aerosol [Michelangeli et al., 1992]. The model domain extends from pole to pole in 10° latitude steps with 40 layers between the surface and the mesosphere (80 km). The horizontal coordinate is the arc length $a\theta$, where a is the radius of the Earth and θ is the latitude (radians). The vertical coordinate $z = H*\ln(p_0/p)$, where the scale height H is 7 km, p_0 is 1000 hPa, and p is the pressure. Model transport is a combination of advection by the residual mean circulation and mixing parameterized as eddy diffusion [Shia et al., 1990]. The advection algorithm is the Prather method [Prather, 1986], which conserves higher-order moments. The radiation field calculations are described in Michelangeli et al. [1992]. Chemical rate coefficients and absorption cross-sections are taken from DeMore et al. [1997], except for O_2 and NO photodissociation cross-sections in the O_2 Schumann-Runge bands between 175 and 206 nm [Allen and Frederick, 1982].

To reproduce the tracer fields with the Caltech-JPL 2D model, we started with independent estimates of advection and diffusion rates. Residual advective velocities are from Eluszkiewicz et al. [1996], which calculated the residual circulation based on a radiative transfer model constrained by observations of temperature, O_3, and H_2O by the Microwave Limb Sounder (MLS). Horizontal and vertical diffusion coefficients are from Summers et al.

[1997], which parameterized atmospheric waves in a 2D model of the stratosphere and mesosphere.

CO_2 is a conservative tracer with an infinite lifetime in the lower and middle stratosphere. It is well-mixed in the troposphere except for its seasonal cycle. However, the secular increase of atmospheric CO_2 means that its mixing ratios in the stratosphere depend on the age of the air (older air was at the surface longer ago when tropospheric CO_2 mixing ratios were lower) [Boering et al., 1996, and references therein]. The ability of a 2D model to reproduce stratospheric CO_2 depends only on the model transport, not photochemistry. Given the high precision and accuracy of the Harvard CO_2 measurements aboard the OMS balloon payload, this dataset is an excellent tool for calibration of transport within the Caltech-JPL 2D model.

Figure 9 shows Harvard CO_2 measurements and two model outputs for the tropics and mid-latitudes. The lowest layer of the model is initialized with the average of CO_2 measurements in the marine boundary layer at Mauna Loa, Hawaii (21°N), and American Samoa (14°S) [T. J. Conway, unpubl.], which have been shown to be remarkably similar to CO_2 measured at the tropical tropopause [Boering et al., 1996]. The observed phase lag between CO_2 in the tropical boundary layer and at the tropical tropopause is two months, but we use a phase lag of one month to allow the model one month to transport CO_2 to the tropical tropopause. Excessively high CO_2 mixing ratios in model 1 imply that the air is "too young," which means that the mean circulation is too fast. In model 2, tropical vertical velocities have been reduced by approximately 40% to give a much better fit to the CO_2 observations in the tropics and at mid-

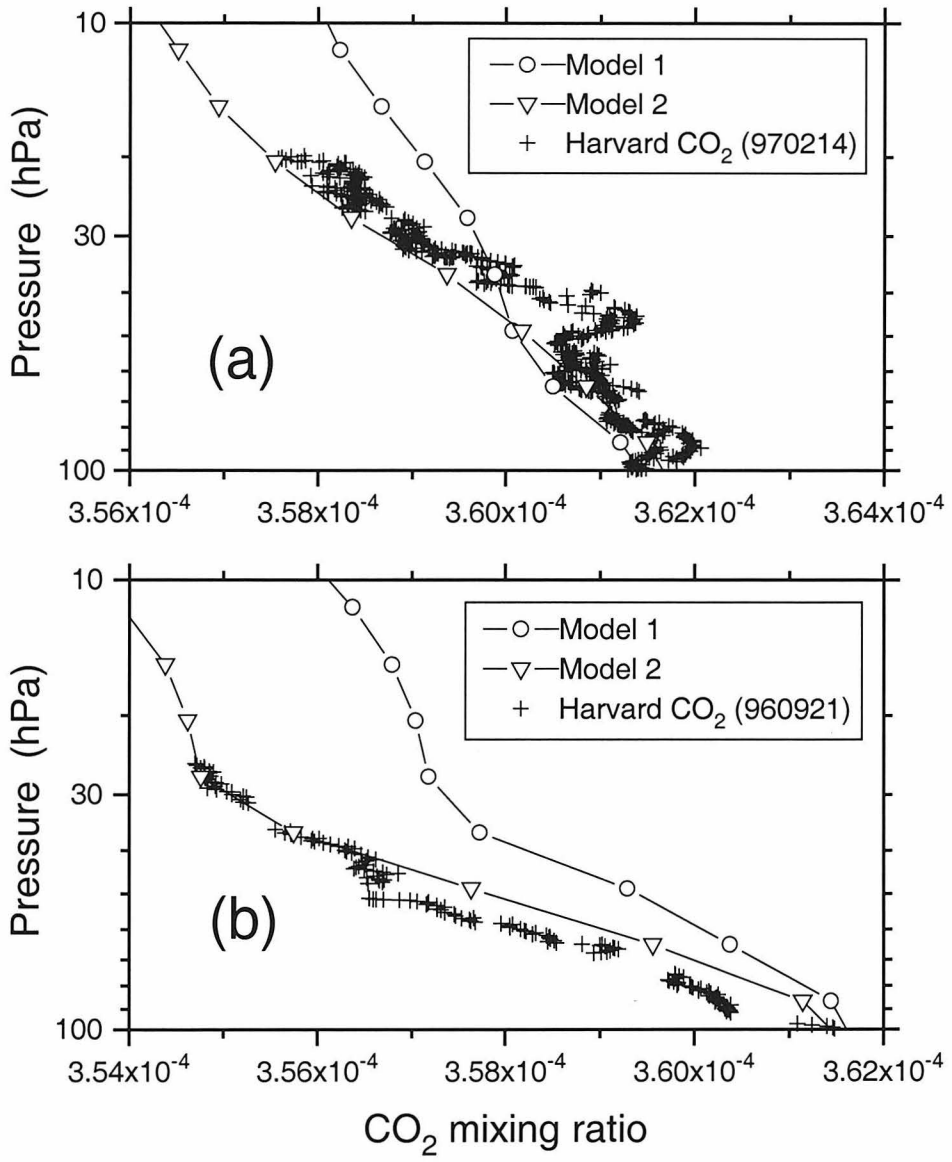

Figure 9. CO_2 profiles from the Caltech-JPL 2D model and Harvard CO_2 measurements aboard the OMS balloon payload: (a) tropical model output for 5°S on February 28, and measurements at 7°S on 970214; (b) mid-latitude model output for 35°N on September 30, and measurements at 34°N on 960921.

latitudes. Model 2 also has faster transport in the troposphere to give slightly higher CO_2 mixing ratios at the tropical tropopause (100 hPa) than in model 1.

With the model mean circulation adjusted to fit the CO_2 data, we next predict N_2O, which has simple loss by photolysis and reaction with $O(^1D)$ (see equations 1.4 and 1.5). Figure 10 shows N_2O profiles from the Caltech-JPL 2D model and measurements by ALIAS II and MkIV. It is apparent that the model consistently overpredicts N_2O at all latitudes. Reducing the model eddy diffusion would decrease N_2O mixing ratios at middle and high latitudes, but the tropical N_2O would still be too high. Decreasing the residual circulation would make CO_2 mixing ratios too low at all latitudes. Thus, the difference between modeled and observed N_2O must be due to photochemical loss rates in the model. N_2O photolysis dominantly occurs at ultraviolet wavelengths of 185 to 210 nm, in a window between the O_2 Schumann-Runge bands and the O_3 Hartley band [Froidevaux and Yung, 1982].

To test the hypothesis that N_2O loss rates may be too small, we next examine CFC-11 (CCl_3F), a chlorofluorocarbon (CFC) that is photodissociated in the same wavelength region. CFC-11 was measured aboard the OMS balloon payload by the Lightweight Airborne Chromatograph Experiment (LACE) [Elkins et al., 1996]. As shown in Figure 11, the model overpredicts CFC-11 at mid-latitudes and in the tropics. CH_4 is also overpredicted, as shown in Figure 12, possibly because its loss processes involve radicals which are affected by transmission in the same wavelength region (see equations 1.7-1.9). We conclude that the model radiation field should be reexamined.

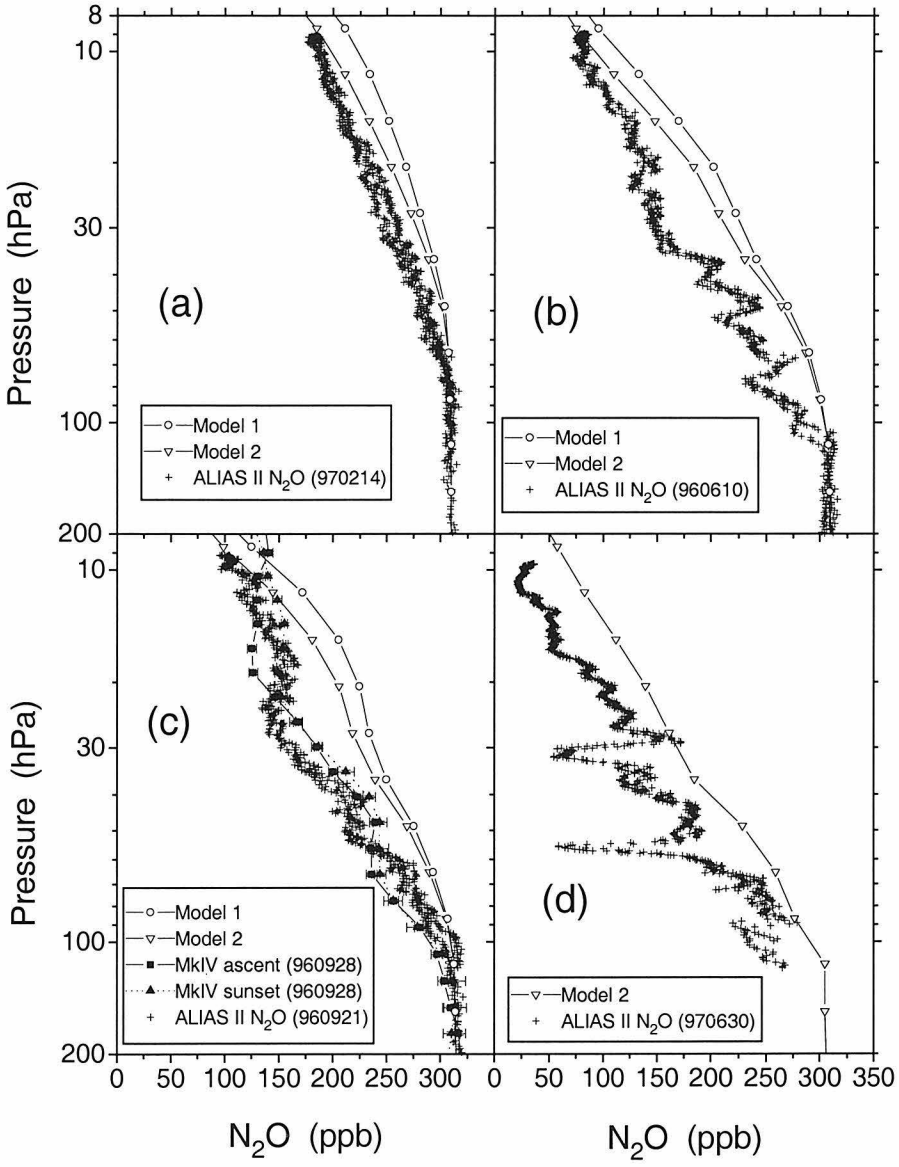

Figure 10. N_2O profiles from the Caltech-JPL 2D model and measurements by ALIAS II and MkIV: (a) tropics in February (same conditions as in Figure 9a), (b) mid-latitude model output for 35°N on June 30 and measurements at 34°N on 960921, (c) mid-latitudes in September (same conditions as in Figure 9b), and (d) high latitude model output for 65°N on June 30 and measurements at 65°N on 970630.

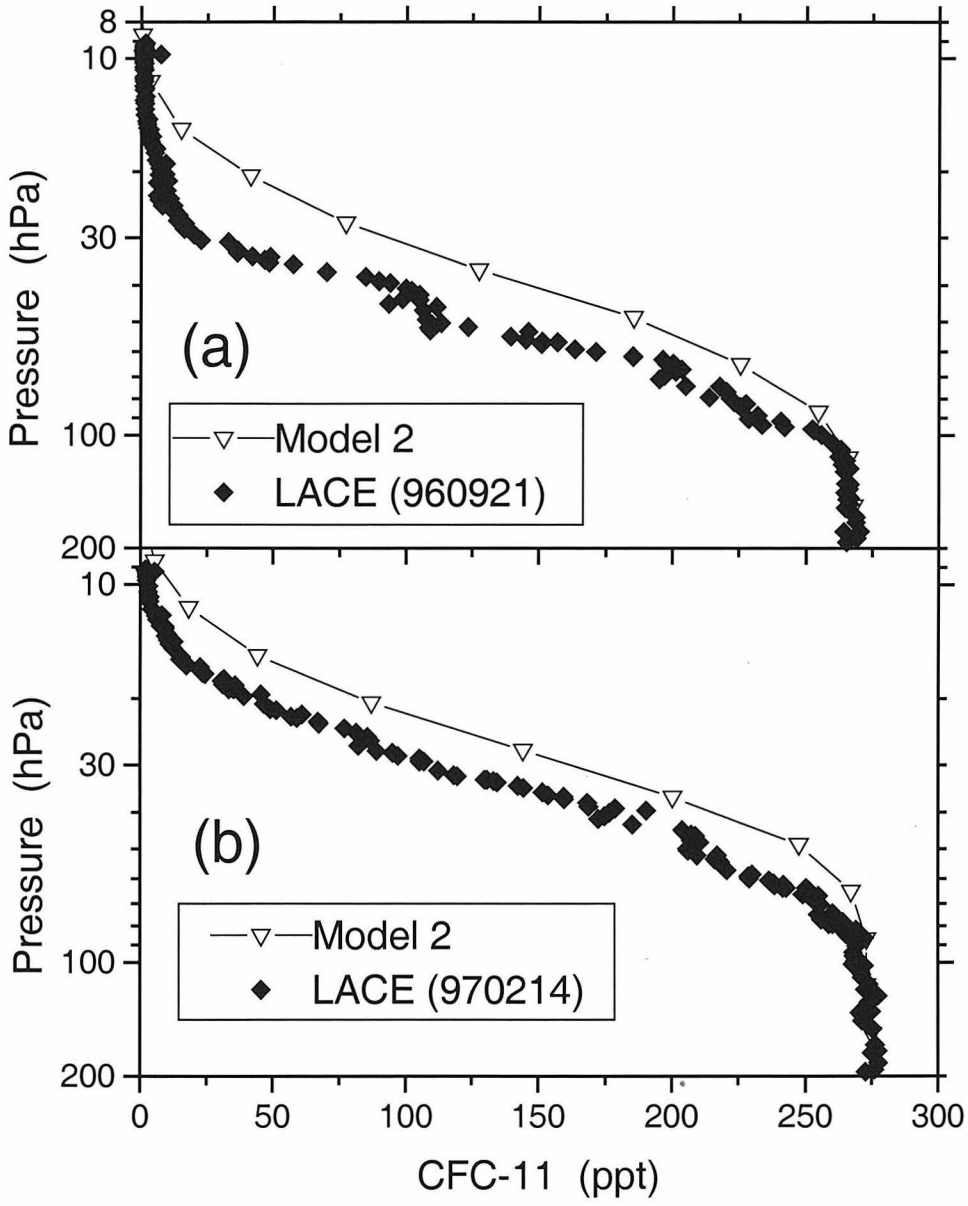

Figure 11. CFC-11 profiles from the Caltech-JPL 2D model and measurements by LACE aboard the OMS balloon payload: (a) mid-latitudes in September (see Figure 9b), (b) tropics in February (see Figure 9a).

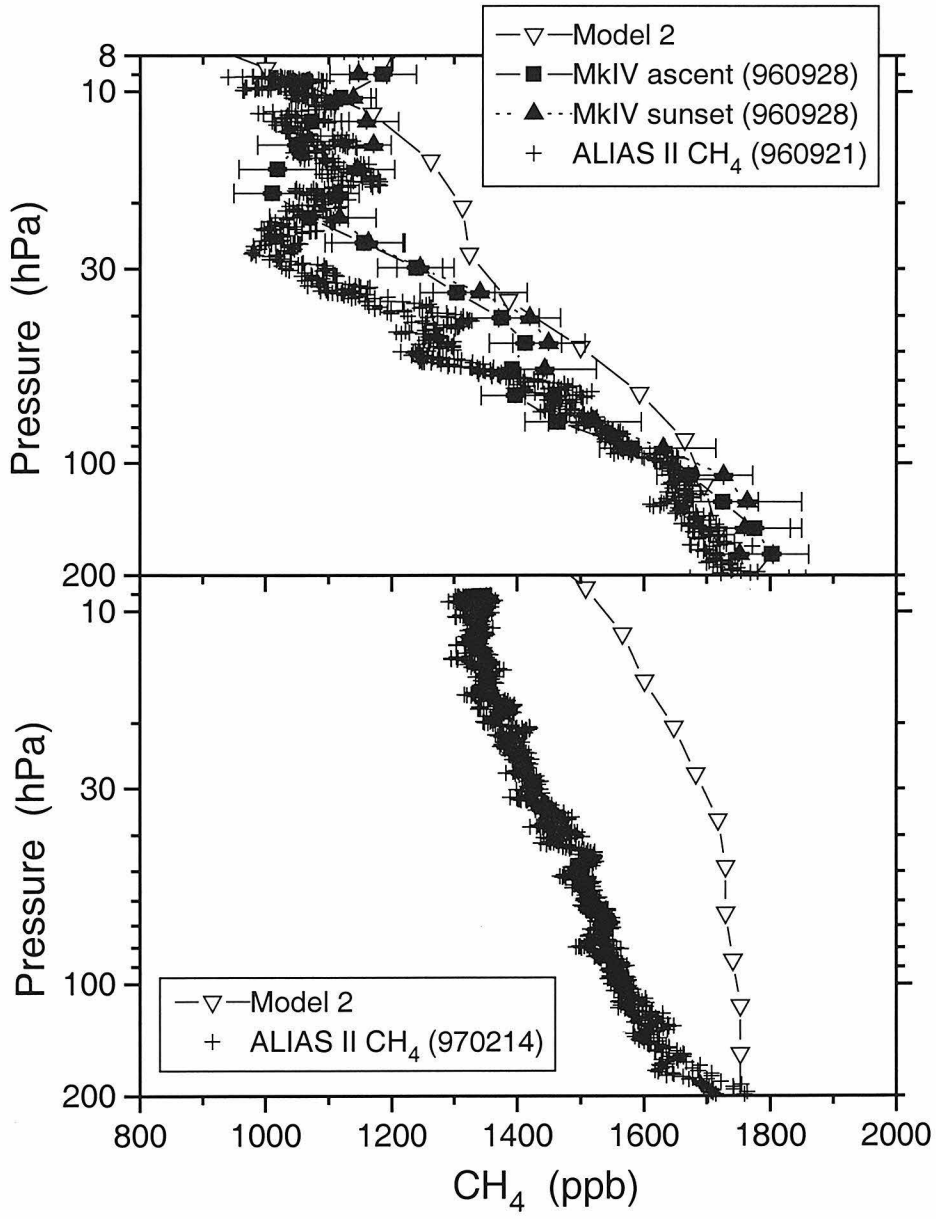

Figure 12. CH_4 profiles from the Caltech-JPL 2D model and measurements by ALIAS II and MkIV: (a) mid-latitudes in September (see Figure 9b), (b) tropics in February (see Figure 9a).

Despite discrepancies between modeled and measured stratospheric tracers, the correlation plots of CH_4 *vs.* N_2O are similar at mid-latitudes (Figure 13). This is misleading because a given point on the correlation plot occurs at a higher altitude in the model than observed in the stratosphere. The tropical model does not reproduce the observations well because CH_4 loss rates are too slow in the model relative to N_2O loss rates. Loss of CH_4 is sensitive to radical concentrations and also temperature (see Chapter 1), and so is harder to model correctly.

To summarize, we have compared tracer measurements with predictions of the Caltech-JPL 2D model. The model mean advective circulation and eddy diffusion are based on model studies of stratospheric circulation [Eluszkiewicz et al., 1996; Summers et al., 1997]. However, advective velocities have been adjusted to match measurements of CO_2 by the Harvard CO_2 instrument aboard the OMS balloon payload. The best model results (model 2) for CO_2 consistently overpredict N_2O, CFC-11, and CH_4 at all latitudes relative to measurements by ALIAS II, MkIV, and LACE. It is suggested that the model flux of solar radiation at 185 to 210 nm in the O_2 Schumann-Runge bands may be too small.

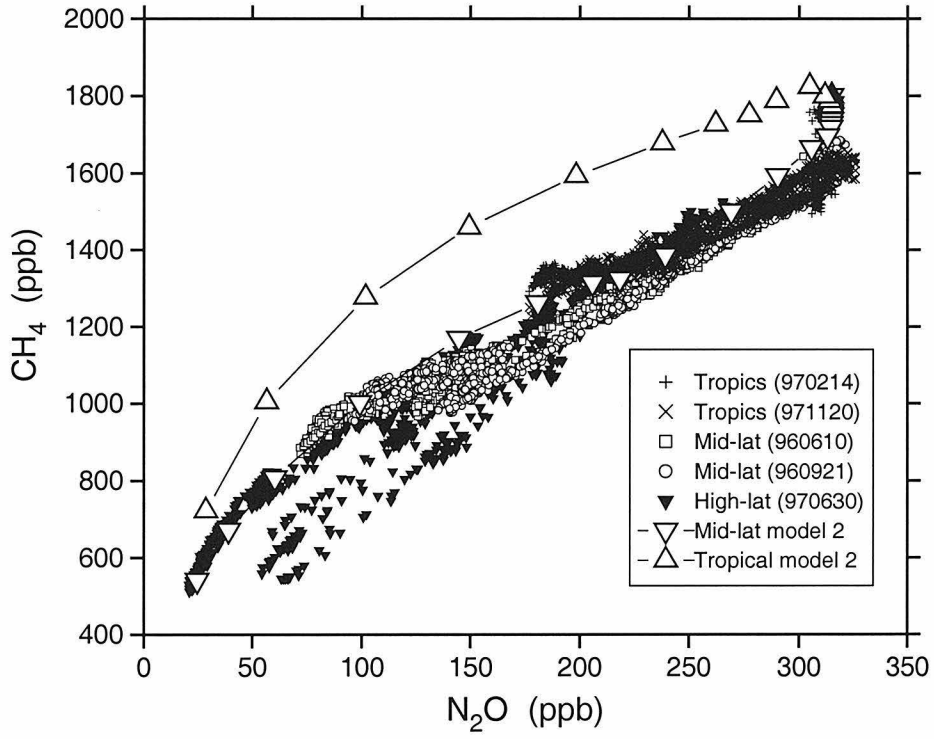

Figure 13. Correlation plot of CH_4 *vs.* N_2O from ALIAS II measurements and the Caltech-JPL 2D model.

BIBLIOGRAPHY

Allen, M., and J. E. Frederick, Effective photodissociation cross sections for molecular oxygen and nitric oxide in the Schumann-Runge bands, *J. Atmos. Sci., 39,* 2066-75, 1982.

Boering, K. A., S. C. Wofsy, B. C. Daube, H. R. Schneider, M. Loewenstein, J. R. Podolske, and T. J. Conway, Stratospheric mean ages and transport rates from observations of carbon dioxide and nitrous oxide, *Science, 274,* 1340-3, 1996.

DeMore, W. B., S. P. Sander, D. M. Golden, R. F. Hampson, M. J. Kurylo, C. J. Howard, A. R. Ravishankara, C. E. Kolb, and M. J. Molina, Chemical Kinetics and Photochemical Data for Use in Stratospheric Modeling, Evaluation No. 12, *JPL Publication 97-4*, 1997.

Elkins, J. W., et al., Airborne gas chromatograph for *in situ* measurements of long-lived species in the upper troposphere and lower stratosphere, *Geophys. Res. Let., 23,* 347-50, 1996.

Eluszkiewicz, J., et al., Residual circulation in the stratosphere and lower mesosphere as diagnosed from Microwave Limb Sounder data, *J. Atmos. Sci., 53,* 217-40, 1996.

Froidevaux, L., M. Allen, and Y. L. Yung, A critical analysis of ClO and O_3 in the mid-latitude stratosphere, *J. Geophys. Res., 90,* 12999-13029, 1985.

Froidevaux, L., and Y. L. Yung, Chemistry in the stratosphere - sensitivity to O_2 absorption cross-sections in the Herzberg Continuum, *Geophys. Res. Let., 9,* 854-7, 1982.

Heidt, L. E., J. F. Vedder, W. H. Pollock, R. A. Lueb, and B. E. Henry, Trace gases in the Antarctic atmosphere, *J. Geophys. Res., 94,* 11599-611, 1989.

Michelangeli, D. V., M. Allen, Y. L. Yung, R.-L. Shia, D. Crisp, and J. Eluszkiewicz, Enhancement of atmospheric radiation by an aerosol layer, *J. Geophys. Res., 97,* 865-74, 1992.

Michelsen, H. A., G. L. Manney, M. R. Gunson, C. P. Rinsland, and R. Zander, Correlations of stratospheric [CH_4] and [N_2O] dervied from ATMOS measurements made during the ATLAS space shuttle missions, submitted to *Geophys. Res. Let.*, 1998.

Plumb, R. A., and M. K. W. Ko, Interrelationships between mixing ratios of long-lived stratospheric constituents, *J. Geophys. Res., 97,* 10145-56, 1992.

Podolske, J. R., and M. Loewenstein, Airborne tunable diode laser spectrometer for trace gas measurements in the lower stratosphere, *Appl. Opt., 32,* 5324-33, 1993.

Prather, M. J., Numerical advection by conservation of second-order moments, *J. Geophys. Res., 91,* 6671-81, 1986.

Shia, R.-L., Y. L. Ha, J.-S. Wen, and Y. L. Yung, Two-Dimensional Atmospheric Transport and Chemistry Model: Numerical Experiments With a New Advection Algorithm, *J. Geophys. Res.*, *95,* 7467-83, 1990.

Summers, M. E., D. E. Siskind, J. T. Bacmeister, R. R. Conway, S. E. Zasadil, and D. F. Strobel, Seasonal variation of middle atmospheric CH_4 and H_2O with a new chemical dynamical model, *J. Geophys. Res.*, *102,* 3503-26, 1997.

Toon, G. C., The JPL MkIV interferometer, *Optics and Photonics News, 2,* 19-21, 1991.

Webster, C. R., R. D. May, C. A. Trimble, R. G. Chave, and J. Kendall, Aircraft (ER-2) laser infrared absorption spectrometer (ALIAS) for in situ stratospheric measurement of HCl, N_2O, CH_4, NO_2, and HNO_3, *Appl. Optics*, *33,* 454-72, 1994.

Chapter 5

Tropical Entrainment Time Scales Inferred from Stratospheric N_2O and CH_4 Observations

R. L. Herman [1], D. C. Scott [2], C. R. Webster [2], R. D. May [2], E. J. Moyer [1], R. J. Salawitch [2], Y. L. Yung [1], G. C. Toon [2], B. Sen [2], J. J. Margitan [2], K. H. Rosenlof [3], H. A. Michelsen [4], J. W. Elkins [5]

[1]Division of Geological and Planetary Sciences, California Institute of Technology, Pasadena, CA 91125.

[2]Jet Propulsion Laboratory, California Institute of Technology, Pasadena, CA 91109.

[3]Aeronomy Laboratory, National Oceanic and Atmospheric Administration, Boulder, CO 80303.

[4]Atmospheric and Environmental Research, Inc., San Ramon, CA 94583.

[5]Climate Monitoring and Diagnostics Laboratory, National Oceanic and Atmospheric Administration, Boulder, CO 80303.

Modified version of a paper

submitted to *Geophysical Research Letters* on March 14, 1998

Contribution number 5762 from the Division of Geological and Planetary Sciences, California Institute of Technology

Abstract. Simultaneous *in situ* measurements of N_2O and CH_4 were made with a tunable diode laser spectrometer (ALIAS II) aboard the Observations from the Middle Stratosphere (OMS) balloon platform from New Mexico, Alaska, and Brazil during 1996 and 1997. We find different compact relationships of CH_4 with N_2O in the tropics and extra-tropics because mixing is slow between these regions. In the extra-tropics, deviations from the normal compact relationship are indicative of transport from the tropics or the polar vortex. We use observed vertical profiles of N_2O and CH_4 and a simple model to calculate the time scale for entrainment of mid-latitude stratospheric air into the tropics. This time scale is estimated to be 7^{+10}_{-7} months for altitudes between the tropical tropopause and 20 km, and 16^{+18}_{-8} months for 20 to 28 km. These results suggest that most of the stratospheric entrainment into the tropics occurs in the lowest portion of the stratosphere.

5.1 Introduction

Historically, long-lived tracers have been used to determine the large-scale circulation of the stratosphere because they are conserved during atmospheric motions that are fast compared to chemical production or loss. Brewer [1949] and Dobson [1956] utilized H_2O and column O_3 as passive tracers to infer that air enters the stratosphere at the tropical tropopause, rises upward in the tropics, moves poleward, and then descends into the troposphere at middle and high latitudes. More recently, stratospheric CH_4 and N_2O have

been studied because of their long photochemical lifetimes, ranging from centuries at the tropopause to 1 year in the middle stratosphere. Both gases are produced at the Earth's surface and are removed in the stratosphere by photochemistry. Early measurements of these gases [e.g., Fabian et al., 1981; Jones and Pyle, 1984] showed stratospheric isopleths sloping downward and poleward, as expected from the Brewer-Dobson model of stratospheric circulation. These measurements also showed temporal and spatial variations that exceeded instrument precision, but the variations were well-correlated for CH_4, N_2O, and other long-lived tracers, implying that they represented only small-scale motions [Ehhalt, 1983]. Therefore, plots of one tracer versus another should remove effects of small-scale dynamics, and can be used to infer larger-scale air motions.

Within a geographic region that has short time scales for quasi-horizontal transport and mixing relative to photochemical time scales for two tracers, those tracers are in "slope equilibrium," which means their functional relationship is independent of location [Plumb and Ko, 1992]. Such tracers are expected to exhibit a compact correlation (i.e., small variance from a well-defined relationship). However, if mixing is slow between two latitudes with different photochemical environments, then the tracer *vs.* tracer relationship will depend on latitude, as observed in the tropical and extra-tropical lower stratosphere [e.g., Murphy et al., 1993; Volk et al., 1996]. Such observations led Plumb [1996] to develop the so-called "tropical pipe" model of stratospheric circulation, in which the tropical stratosphere is isolated from the extra-tropics. However, tracer observations show that the barrier is permeable

to transport between the tropics and mid-latitudes [Avallone and Prather, 1996; Minschwaner et al., 1996; Volk et al., 1996; Schoeberl et al., 1997], sometimes associated with planetary wave activity [e. g., Waugh, 1993].

Tracer observations can be used to infer the time scale for mid-latitude stratospheric air to be transported back into the tropical stratosphere, which we define here as the "entrainment" time scale. Previous studies concluded that the mean entrainment time scale is approximately 12 to 18 months at 20 km and that about 50% of the tropical air at 21 km had been entrained from mid-latitudes [Minschwaner et al., 1996; Volk et al., 1996]. In this paper, we present new, high-precision observations of stratospheric N_2O and CH_4 and use them to quantify the entrainment time scale in the lower and middle stratosphere.

5.2 Balloon Observations of N_2O and CH_4

The Aircraft Laser Infrared Absorption Spectrometer II (ALIAS II) has measured *in situ* N_2O and CH_4 mixing ratios on flights of the Observations from the Middle Stratosphere (OMS) balloon platform from New Mexico (34°N, 104°W), Alaska (65°N, 148°W), and Brazil (7°S, 39°W). ALIAS II uses tunable diode lasers to measure N_2O and CH_4 by infrared absorption spectroscopy [Webster et al., 1994]. During balloon ascent and descent, air flows freely through an open-path multipass cell (61.8 m optical path) suspended outside the gondola. Measurements of both gases have an estimated 5% precision and 5% accuracy relative to calibration standards provided by the

National Oceanic and Atmospheric Administration (NOAA) Climate Monitoring and Diagnostics Laboratory (CMDL). Simultaneous measurements of pressure and temperature were used to calculate potential temperature θ (the temperature of an air parcel adiabatically compressed or expanded to 1000 hPa, which is conserved in adiabatic motion). The following analysis uses data obtained during both ascent and descent, from the upper troposphere (200 hPa) to the middle stratosphere (9 hPa).

CH_4 and N_2O mixing ratios are highly correlated in the ALIAS II observations (Figure 1a). In the lower stratosphere ($230 \leq N_2O \leq 310$ ppb), the CH_4 *vs.* N_2O relation is linear and compact at all latitudes due to the long photochemical lifetime of each species at low altitudes. However, for $N_2O <$ 230 ppb, the tropical CH_4 *vs.* N_2O relation deviates from the extra-tropical relation. A similar separation in CH_4 *vs.* N_2O relationships has been recorded by the Atmospheric Trace MOlecule Spectroscopy (ATMOS) instrument aboard the space shuttle [Michelsen et al., 1998] (Figures 1a and 1b). This separation verifies that there is some degree of a barrier between the tropical and mid-latitude stratosphere, to be quantified in the next section.

At mid-latitudes, ALIAS II CH_4 and N_2O have a compact relationship at all altitudes observed, in agreement with ATMOS. The JPL MkIV interferometer [Toon, 1991] has also measured similar CH_4 and N_2O at mid-latitudes using solar occultation (Figure 1b). However, for $N_2O < 150$ ppb, the mid-latitude MkIV relation of the 960928 (yymmdd) flight lies between the ATMOS mid-latitude and tropical curves, presumably because the air has come from the tropics recently and has not mixed completely with the

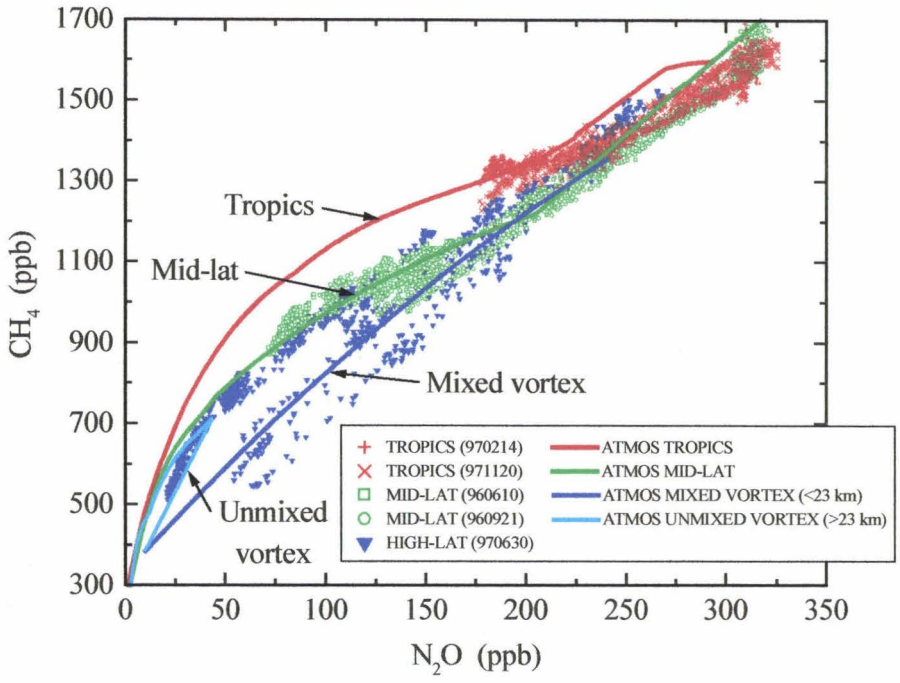

Figure 1a. CH_4 *vs.* N_2O volume mixing ratios. In the lower stratosphere ($230 \leq N_2O \leq 310$ ppb), the CH_4 *vs.* N_2O relation is linear and compact at all latitudes due to the long photochemical lifetime of each species at low altitudes. However, for $N_2O < 230$ ppb, the tropical CH_4 *vs.* N_2O relation deviates from the extra-tropical relation. With the exception of two remnants of the Arctic polar vortex, the high latitude CH_4 *vs.* N_2O relation is essentially the same as the mid-latitude relation due to rapid meridional transport in the extra-tropical "surf zone." Symbols: ALIAS II (red: tropics, green: mid-latitudes, blue: high latitudes); thick lines: curve fits to ATMOS data [Michelsen et al., 1998].

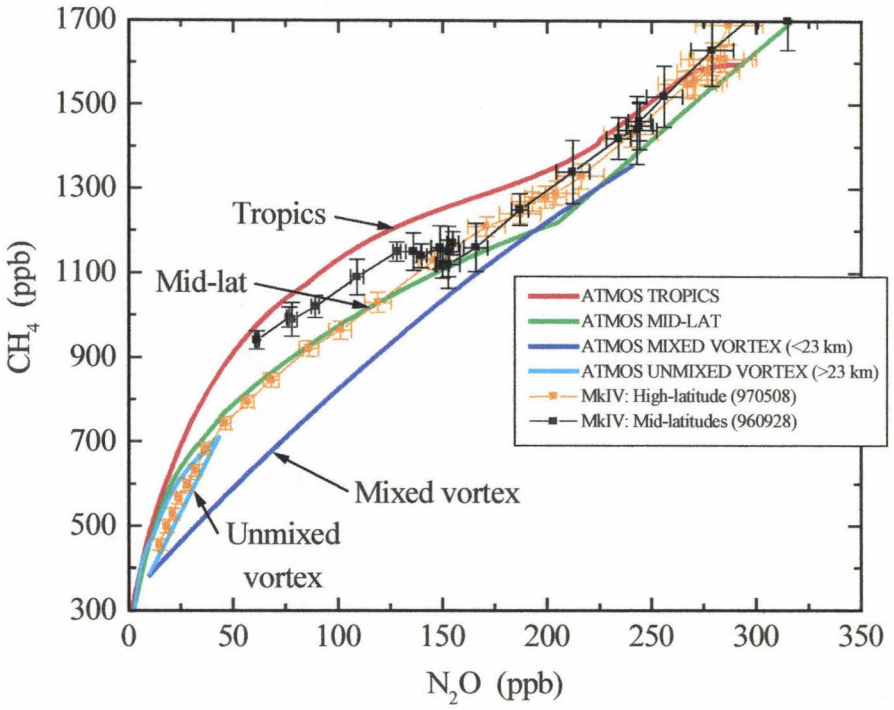

Figure 1b. CH_4 *vs.* N_2O volume mixing ratios. For $N_2O < 150$ ppb, the mid-latitude MkIV relation (960928 in yymmdd format) is intermediate between the ATMOS mid-latitude and tropical curves because the air has not yet mixed completely with its mid-latitude surroundings. The high-latitude MkIV relation (970508) is very similar to the ATMOS mid-latitude relation and the high latitude ALIAS II relation (970630) due to rapid meridional transport. Lines with symbols and error bars: MkIV (black: mid-latitudes, orange: high latitudes); thick lines: curve fits to ATMOS data [Michelsen et al., 1998].

background mid-latitude reservoir. This feature corresponds to higher mixing ratios of CH_4 and N_2O above 25 km ($\theta > 630$ K), as shown in Figure 2. Such features have often been measured at mid-latitudes by MkIV, ALIAS II (960921), and others [e.g., Kondo et al., 1996], and are manifestations of outflow from the tropics.

At high latitudes, the CH_4 *vs.* N_2O relation measured by ALIAS II (970630) is similar to the MkIV relation (970508) and the ATMOS mid-latitude relation due to rapid meridional transport within the extra-tropics. ATMOS measurements outside the polar vortex confirm this observation [Michelsen et al., 1998]. However, ALIAS II intercepted two narrow layers with anomalously low mixing ratios centered at $\theta \approx 515$ K (20.4 km) and 615 K (24.0 km) (Figure 2). At these altitudes, such low mixing ratios could only be associated with remnants of the Arctic polar vortex. These remnants are not evident in the MkIV high latitude data measured on 970508 because the flight was prior to the breakup of the vortex. All of the high latitude ALIAS II data that fall below the cluster of mid-latitude data in Figure 1a are from these layers and their partially mixed edges. These data are similar to the Arctic vortex CH_4 *vs.* N_2O relation of ATMOS because both are mixing lines between mid-latitude lower stratospheric air and Arctic polar vortex air that had descended from the upper stratosphere. Although meridional transport is rapid within the extra-tropics, the vortex remnants are preserved because mixing is slowest during the summer [e.g., Hess and Holton, 1985].

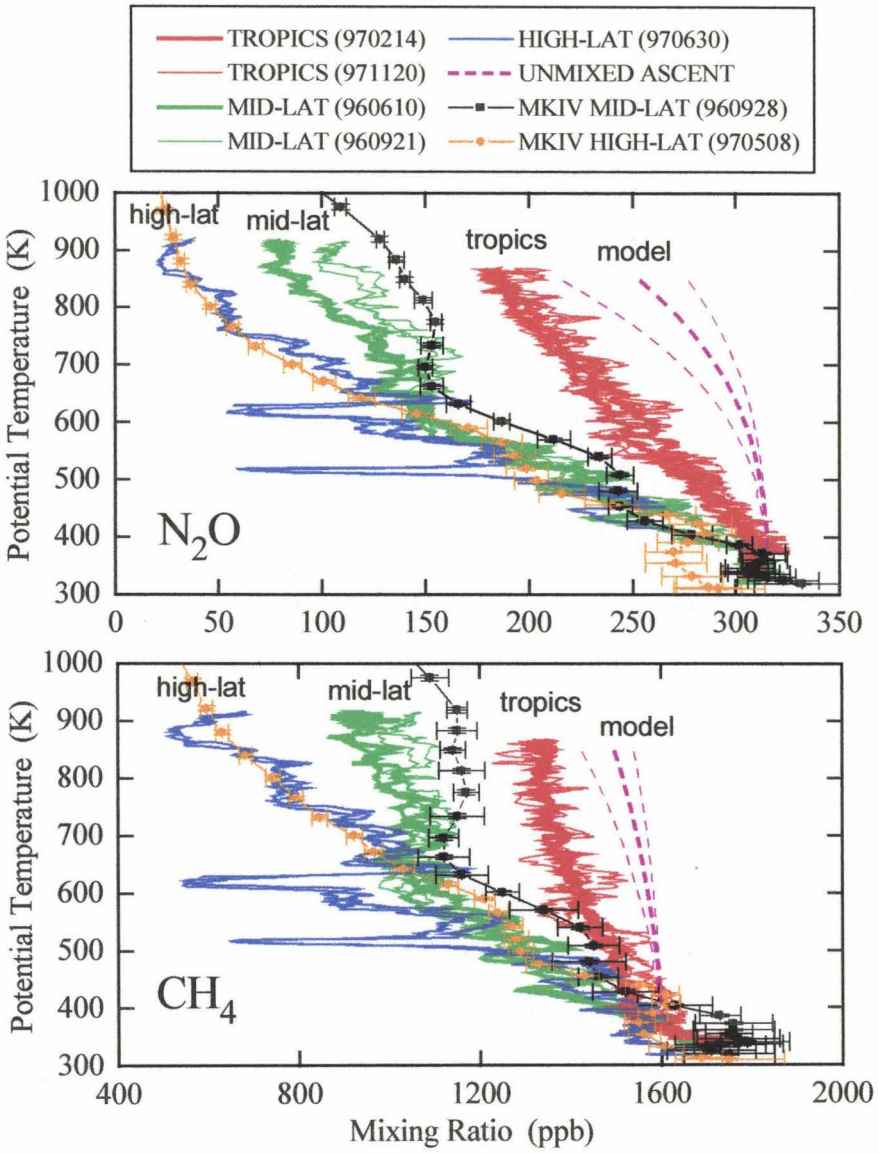

Figure 2. Potential temperature θ *vs.* N_2O and CH_4. The two thin remnants of the Arctic polar vortex are clearly seen in this figure at θ ≈ 520 K (55 hPa) and 620 K (32 hPa). The model of unmixed tropical ascent (entrainment time scale $\tau_{IN} \rightarrow \infty$) is significantly different from the observed tropical N_2O and CH_4. Red, green, and blue lines: ALIAS II (red: tropics, green: mid-latitudes, blue: high latitudes); lines with symbols: MkIV; pink line: model of unmixed tropical ascent (±1 st. dev.).

5.3 Tropical Model

For the purposes of estimating entrainment time scales, we use only the tropical and mid-latitude data. At a given potential temperature, the measured mixing ratios of N_2O and CH_4 in the tropics are considerably higher than in the extra-tropics (Figure 2) because tropical air has spent considerably less time in the stratosphere and has experienced less photochemical loss. The 971120 data show considerable variability, but N_2O and CH_4 are correlated with each other and with other tracers measured on the OMS payload. Furthermore, the mean profiles of N_2O and CH_4 are similar for both tropical flights, so in the analysis that follows, we use a polynomial fit to represent the tropical data.

We calculate the time scale for entrainment of mid-latitude air into the tropics by comparing the observed tropical mixing ratio profiles to values calculated by a simple tropical model allowing for photochemical loss, vertical advection, and mixing from mid-latitudes. For an air parcel ascending in the tropics with isentropic entrainment of extra-tropical air, the continuity equation is given by [Minschwaner et al., 1996; Volk et al., 1996]:

$$Q\frac{\partial \chi}{\partial \theta} = -L\chi - \gamma\chi + \left(\frac{\chi_{MID} - \chi}{\tau_{IN}}\right) \tag{5.1}$$

where Q is the mass-balanced heating rate, χ is the tropical mixing ratio, χ_{MID} is the mid-latitude mixing ratio at the same potential temperature, $L\chi$ is the local photochemical loss rate, $\gamma\chi$ is the long-term growth rate, and τ_{IN} is

the time scale for entrainment of mid-latitude air into the tropical stratosphere. Mass-balanced heating rates Q were calculated from a radiative heating model [Rosenlof, 1995], and averaged over latitude (9.5°S - 9.5°N), two years (July 1995 - June 1997), and all longitudes to obtain mean tropical heating rates. Long-term growth rates are included because stratospheric air is older than tropospheric air and thus has a time lag in its initial mixing ratio. These growth rates are global averages of recent tropospheric trends in data collected by the NOAA CMDL global network [Elkins and Dlugokencky, unpubl.].

Photochemical loss includes removal of N_2O by photolysis and reaction with $O(^1D)$, and removal of CH_4 by reaction with OH, $O(^1D)$, and Cl. Twenty four hour average photolysis rates were calculated with a radiative transfer model using observed temperature and O_3 profiles (JPL O_3 measurements from 0 to 30 km, and satellite-based climatology above 30 km) [Salawitch et al., 1994; Minschwaner et al., 1993]. The photochemical model was initialized with measured CH_4, N_2O, and H_2O. NO_y was inferred from the ATMOS relation with N_2O observed in the tropics during November 1994 [M. R. Gunson, pers. comm., 1998]. Cl_y (total inorganic chlorine) and Br_y (total inorganic bromine) were specified based on relations with CFC-11 observed by the NOAA Lightweight Airborne Chromatograph Experiment (LACE) [Elkins et al., 1996] and also inferred from *in situ* measurements of organic source gases near 20 km [Wamsley et al., 1998]. Sulfate aerosol surface area was estimated from SAGE II extinction measurements. Twenty four hour average concentrations of OH, $O(^1D)$, and Cl were calculated with this photochemical model [Salawitch et al., 1994] using reaction rates and absorption cross

sections from DeMore et al. [1997]. Our error estimates are 30% uncertainty in the N_2O photolysis rate, reaction rate coefficient uncertainties from DeMore et al. [1997], 20% uncertainty in radical concentrations, 40% uncertainty in the heating rate for $p < 50$ hPa, and 60% uncertainty in the heating rate for $50 < p < 90$ hPa (errors added in quadrature). However, we can reproduce CO measured in the tropical lower stratosphere with this tropical model to a high degree of accuracy (see Chapter 3). Errors in predicted CO propagated from the stated uncertainties lie well outside the range of the measured CO data, which suggests that the actual uncertainties in ascent rate are smaller than stated above.

5.4 Discussion

In the limit $\tau_{IN} \rightarrow \infty$, expression (5.1) represents vertical advection in the tropics with no mixing in from the extra-tropics, and is solved to obtain unmixed ascent profiles (Figure 2). The measured tropical N_2O and CH_4 decrease significantly faster with altitude than predicted by this model, so entrainment of extra-tropical stratospheric air is required to explain the observed mixing ratios [Minschwaner et al., 1996; Volk et al., 1996; Avallone and Prather, 1996].

To estimate the time scale for entrainment of mid-latitude air into the tropics, we first solve (5.1) for τ_{IN} at each potential temperature, θ, in the model. In Figure 3, the resultant best variable τ_{IN} for N_2O is shown as "variable τ." This time scale increases with altitude from less than 3 months

near the tropical tropopause ($\theta \approx 370$ K) to approximately 13.5 months at θ = 500 K. At θ = 600 K, τ_{IN} is approximately 16 months, and at $\theta > 790$ K, τ_{IN} becomes undefined as the expression in the denominator goes to zero. The shape of the variable τ_{IN} profile is similar to that derived by Minschwaner et al. [1996] based on balloon N_2O data from Goldan et al. [1980]. For $\theta >$ 550 K, τ_{IN} is significantly larger than that derived from N_2O measured by the Cryogenic Limb Array Etalon Spectrometer (CLAES) aboard the Upper Atmosphere Research Satellite (UARS) [Minschwaner et al., 1996]. This is largely a reflection of the large uncertainties (ca. 20%) in CLAES data.

We assess these different entrainment time scales by substituting values of τ_{IN} back into expression (5.1). Then, we forward-model tropical profiles of N_2O and CH_4, as shown in Figures 4 and 5, respectively. At first glance, most of these entrainment time scales fit the ALIAS II N_2O and CH4 data fairly well. However, the high altitude data ($\theta > 450$ K) are fitted best with entrainment time scales of 1 to 2 years. In contrast, the low altitude data fall off rapidly just above the tropopause despite photochemical lifetimes greater than 100 years. To fit the low altitude data, entrainment time scales shorter than 12 months are required. The simplest solution that reproduces the data well is a short entrainment time scale for the lower stratosphere and a longer time scale for the middle stratosphere, as shown in Figures 4 and 5. For N_2O, the best estimate of τ_{IN} is 7 (+10, -7) months at altitudes between the tropical tropopause and 20 km (385 K $< \theta <$ 450 K), and 16 (+18, -8) months for

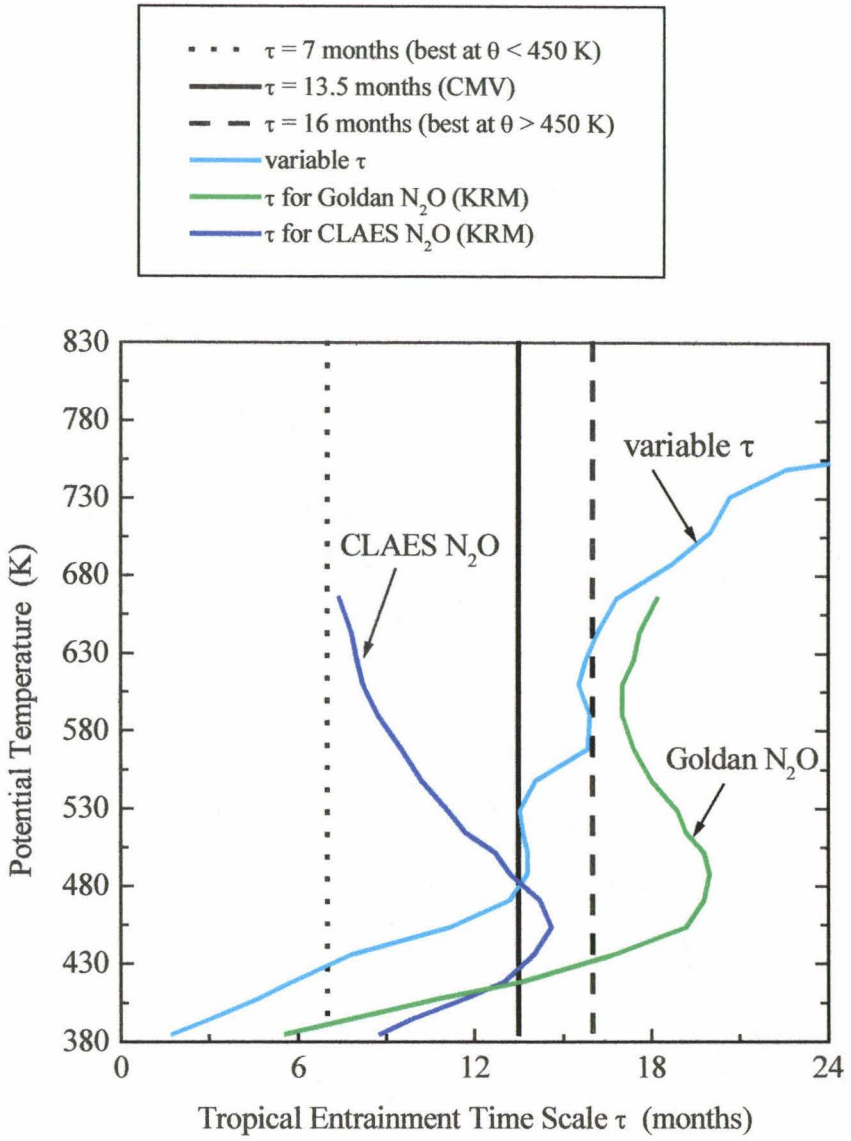

Figure 3. Entrainment time scales τ_{IN} for stratospheric air to be transported quasi-adiabatically from the extra-tropical "surf zone" into the tropics. The 13.5 month time scale (CMV) was determined by Volk et al. [1996] based on ER-2 tracer data at $\theta < 500$ K. Variable τ represents the best time scale for matching the ALIAS II N_2O at each θ. Goldan and CLAES time scales were determined by Minschwaner et al [1996] from old balloon and satellite data, respectively.

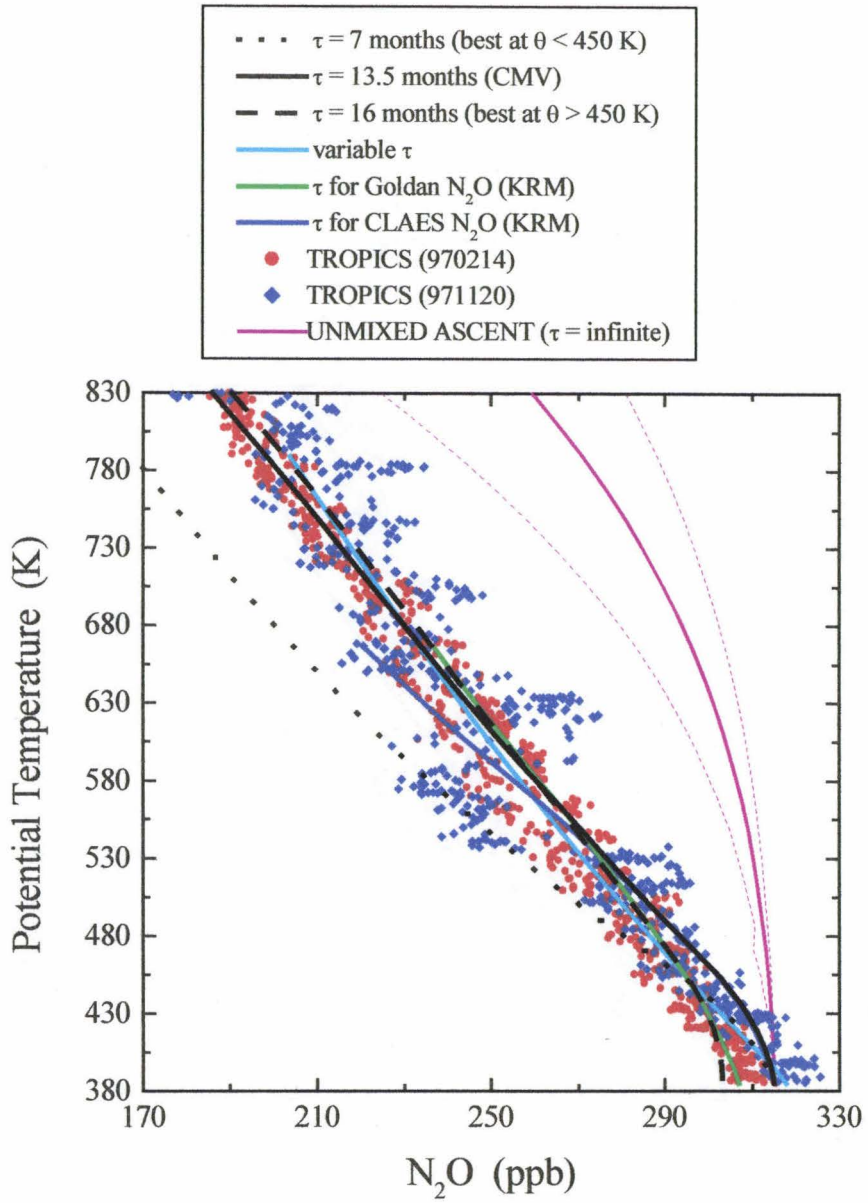

Figure 4. Potential temperature θ *vs.* tropical N_2O. The best N_2O tropical model has entrainment time scales of 7^{+10}_{-7} months for altitudes between the tropical tropopause and 20 km (385 K < θ < 450 K), and 16^{+18}_{-8} months for altitudes between 20 and 28 km (450 K < θ < 770 K). Red symbols: ALIAS II; pink line: same as Figure 2; other lines: different entrainment models as described in the legend.

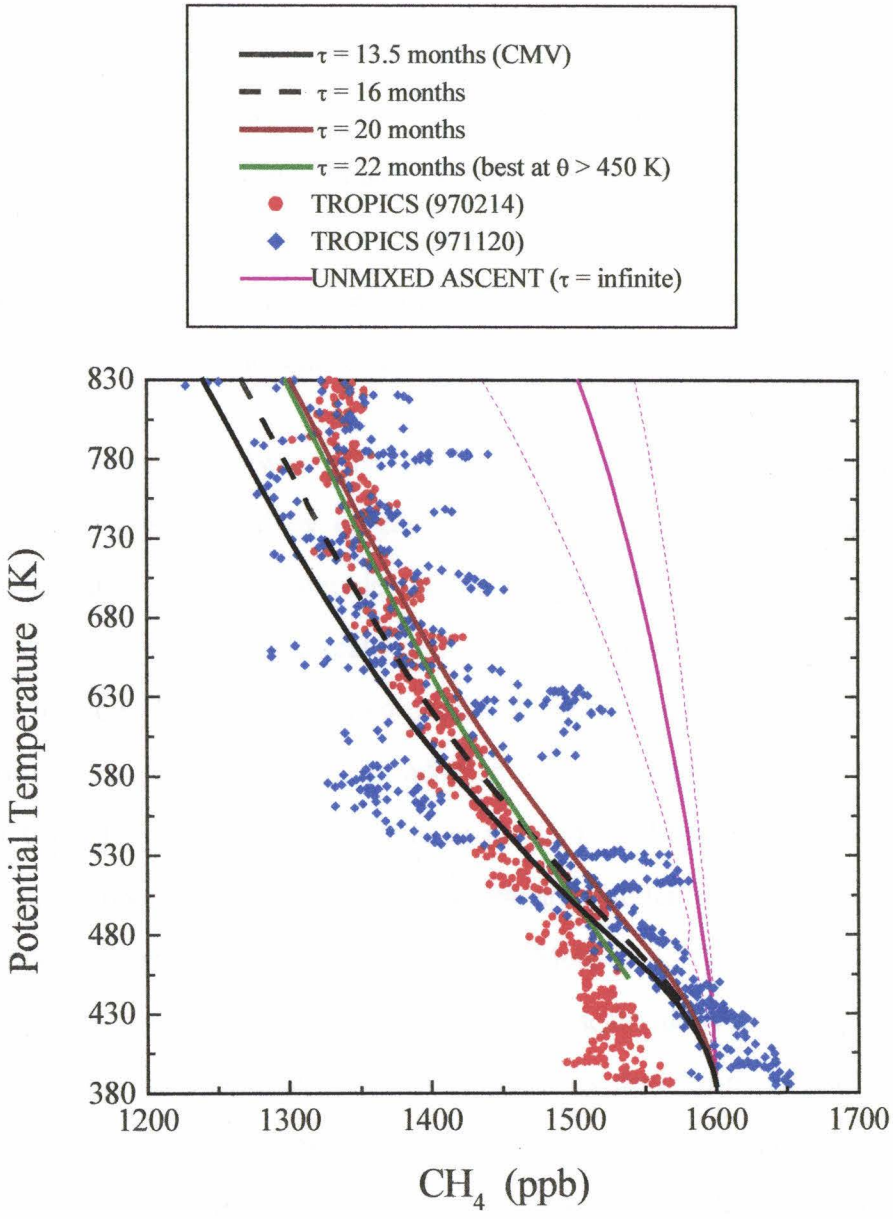

Figure 5. Potential temperature θ *vs.* tropical CH_4. The best CH_4 tropical model has an entrainment time scale of 22^{+38}_{-14} months for altitudes between 20 and 27 km (450 K < θ < 690 K). However, we have greater confidence in the N_2O data. Red symbols: ALIAS II; pink line: same as Figure 2; other lines: different entrainment models as described in the legend.

altitudes between 20 and 28 km (450 K < θ < 770 K). Entrainment time scales from Volk et al. [1996] and Minschwaner et al. [1996] also do a good job in fitting the N_2O data, with the exception of the time scale derived from CLAES data. For CH_4, τ_{IN} is approximately 8 months (highly uncertain) between the tropical tropopause and 20 km, increasing to 22^{+38}_{-14} months for altitudes between 20 and 27 km (450 K < θ < 690 K). Given the size of the error bars, we cannot rule out a time scale that is independent of altitude.

Discrepancies between the model and observations at the highest altitudes may be caused by outgassing of the balloon payload when it is stationary at its maximum altitude. Within the error bars, N_2O and CH_4 yield consistent entrainment time scales, but given the large differences in lower stratospheric CH_4 between the two tropical flights (Figure 5), we have higher confidence in the N_2O results. In addition to uncertainties stated above, the error bars of τ_{IN} include 5% instrument precision and the uncertainty in the observed slope. The derived time scales are similar to previous results [Minschwaner et al., 1996; Volk et al., 1996; Mote et al., 1996, 1998], but we reiterate that there is better agreement with time scales derived from previous balloon measurements of N_2O than from CLAES data [Minschwaner et al., 1996]. The shorter entrainment time scale below 20 km suggests that most of the entrainment into the tropics occurs in this portion of the lower stratosphere [Schoeberl et al., 1997].

In situ observations of N_2O and CH_4 reported here show distinct compact relations for the tropics and extra-tropics. We have used a simple model of the tropical upwelling region to quantify the entrainment rate of mid-latitude air

into the tropics. The mean time scale of entrainment increases with altitude from 7 (+10, -7) months for altitudes between the tropical tropopause and 20 km to 16 (+18, -8) months for altitudes between 20 and 28 km. Two dimensional stratospheric models typically allow for considerably faster exchange of mid-latitude and tropical air than found here. Our results have important implications for calculated trends of mid-latitude ozone [e.g., Volk et al. 1996] as well as the altitude and latitude distribution of NO_y released by future fleets of supersonic aircraft. Once in the tropical stratosphere, NO_y is efficiently lofted to higher altitudes where perturbations to ambient levels of NO_y lead to greater loss of O_3. The calculated entrainment time scales provide important empirical constraints for evaluating multi-dimensional models used to calculate the effects of anthropogenic gases on the global O_3 distribution.

Acknowledgements

We thank C. M. Volk, F. L. Moore, A. P. Ingersoll, M. A. Allen, and K. Minschwaner for helpful discussions, H. Vömel for temperature data, and A. E. Kulawik for computational assistance. We also thank W. H. Brune, G. J. Flesch, L. Kroll, M. Tuchscherer, J. Riccio, R. Howe, B. Wilson, J. Landeros, and the National Scientific Balloon Facility (NSBF) for making these balloon flights possible. Support for this work and the OMS balloon flights was provided by NASA's Upper Atmospheric Research Program and Atmospheric Effects of Aviation Project. H.A.M. was supported by NASA grant NAS1-96022. Part of the research described in this paper was carried out by the Jet

Propulsion Laboratory, California Institute of Technology, under a contract with the National Aeronautics and Space Administration. Division of Geological and Planetary Sciences, California Institute of Technology, Contribution 5762.

BIBLIOGRAPHY

Avallone, L. M., and M. J. Prather, Photochemical evolution of ozone in the lower tropical stratosphere, *J. Geophys. Res., 101,* 1457-61, 1996.

Brewer, A. W., Evidence for a world circulation provided by the measurements of helium and water vapor distribution in the stratosphere, *Q. J. Roy. Meteor. Soc., 75,* 351-63, 1949.

DeMore, W. B., S. P. Sander, D. M. Golden, R. F. Hampson, M. J. Kurylo, C. J. Howard, A. R. Ravishankara, C. E. Kolb, and M. J. Molina, Chemical Kinetics and Photochemical Data for Use in Stratospheric Modeling, Evaluation No. 12, *JPL Publication 97-4,* 1997.

Dobson, G. M. B., Origin and distribution of the polyatomic molecules in the atmosphere, *Proc. Roy. Soc. London, A, 236,* 187-93, 1956.

Ehhalt, D. H., E. P. Röth, and U. Schmidt, On the Temporal Variance of Stratospheric Trace Gas Concentrations, *J. Atmos. Chem., 1,* 27-51, 1983.

Elkins, J. W., et al., Airborne gas chromatograph for *in situ* measurements of long-lived species in the upper troposphere and lower stratosphere, *Geophys. Res. Let., 23,* 347-50, 1996.

Fabian P., R. Borchers, G. Flentje, W. A. Matthews, W. Seiler, H. Giehl, K. Bunse, F. Müller, U. Schmidt, A. Volz, A. Khedim, and F. J. Johnen, The Vertical Distribution of Stable Trace Gases at Mid-latitudes, *J. Geophys. Res. 86,* 5179-84, 1981.

Hess, P. G., and J. R. Holton, The origin of temporal variance in long-lived trace constituents in the summer stratosphere, *J. Atmos. Sci., 42,* 1455-63, 1985.

Jones, R. L., and J. A. Pyle, Observations of CH_4 and N_2O by the NIMBUS 7 SAMS: A Comparison With In Situ Data and Two-Dimensional Numerical Model Calculations, *J. Geophys. Res., 89,* 5263-79, 1984.

Kondo, Y., U. Schmidt, T. Sugita, P. Aimedieu, M. Koike, H. Ziereis, and Y. Iwasaka, NO_y correlation with N_2O and CH_4 in the midlatitude stratosphere, *Geophys. Res. Let., 23,* 2369-72, 1996.

Michelsen, H. A., G. L. Manney, M. R. Gunson, C. P. Rinsland, and R. Zander, Correlations of stratospheric [CH_4] and [N_2O] derived from ATMOS measurements made during the ATLAS space shuttle missions, *Geophys. Res. Let.*, submitted, 1998.

Minschwaner, K., A. E. Dessler, J. W. Elkins, C. M. Volk, D. W. Fahey, M. Loewenstein, J. R. Podolske, A. E. Roche, and K. R. Chan, Bulk properties of isentropic mixing into the tropics in the lower stratosphere, *J. Geophys. Res., 101,* 9433-9, 1996.

Minschwaner, K., R. J. Salawitch, and M. B. McElroy, Absorption of solar radiation by O_2 - implications for O_3 and lifetimes of N_2O, $CFCl_3$, and CF_2Cl_2, *J. Geophys. Res., 98,* 10543-61, 1993.

Mote, P. W., T. J. Dunkerton, M. E. McIntyre, E. A. Ray, P. H. Haynes, J. M. Russell III, Vertical velocity, vertical diffusion, and dilution by midlatitude air in the tropical lower stratosphere, *J. Geophys. Res., 103* , 8651-666, 1998.

Mote, P. W., K. H. Rosenlof, M. E. McIntyre, E. S. Carr, J. C. Gille, J. R. Holton, J. S. Kinnersley, H. C. Pumphrey, J. M. Russell III, and J. W. Waters, An atmospheric tape recorder: The imprint of tropical tropopause temperatures on stratospheric water vapor, *J. Geophys. Res., 101,* 3989-4006, 1996.

Murphy, D. M., D. W. Fahey, M. H. Proffitt, S. C. Liu, K. R. Chan, E. S. Eubank, S. R. Kawa, and K. K. Kelly, Reactive nitrogen and its correlation with ozone in the lower stratosphere and upper troposphere, *J. Geophys. Res., 98,* 8751-73, 1993.

Plumb, R. A., A "tropical pipe" model of stratospheric transport, *J. Geophys. Res., 101,* 3957-72, 1996.

Plumb, R. A., and M. K. W. Ko, Interrelationships between mixing ratios of long-lived stratospheric constituents, *J. Geophys. Res., 97,* 10145-56, 1992.

Rosenlof, K. H., Seasonal cycle of the residual mean meridional circulation in the stratosphere, *J. Geophys. Res., 100,* 5173-91, 1995.

Salawitch, R. J., et al., The diurnal variation of hydrogen, nitrogen, and chlorine radicals: implications for the heterogeneous production of HNO_2, *Geophys. Res. Let., 21,* 2551-4, 1994.

Schoeberl, M. R., A. E. Roche, J. M. Russell III, D. Ortland, P. B. Hays, and J.W. Waters, An estimation of the dynamical isolation of the tropical lower stratosphere using UARS wind and trace gas observations of the quasi-biennial oscillation, *Geophys. Res. Let., 24,* 53-6, 1997.

Toon, G. C., The JPL MkIV interferometer, *Optics and Photonics News, 2,* 19-21, 1991.

Volk, C. M., J. W. Elkins, D. W. Fahey, R. J. Salawitch, G. S. Dutton, J. M. Gilligan, M. H. Proffit, M. Loewenstein, J. R. Podolske, K. Minschwaner, J. J. Margitan, and K. R. Chan, Quantifying transport between the tropical and mid-latitude lower stratosphere, *Science, 272,* 1763-8, 1996.

Wamsley, P. R., et al., Distribution of halon-1211 in the upper troposphere and lower stratosphere and the 1994 total bromine budget, *J. Geophys. Res., 103,* 1513-26, 1998.

Waugh, D. W., Subtropical stratospheric mixing linked to disturbances in the polar vortices, *Nature, 365,* 535-7, 1993.

Webster, C. R., R. D. May, C. A. Trimble, R. G. Chave, and J. Kendall, Aircraft (ER-2) laser infrared absorption spectrometer (ALIAS) for *in-situ*

stratospheric measurements of HCl, N_2O, CH_4, NO_2, and HNO_3, *Appl. Opt., 33,* 454-72, 1994.

Chapter 6

Summary

In this thesis, we have presented new *in situ* measurements of tracers in the upper troposphere and stratosphere and have used them to infer transport time scales in the stratosphere. The photochemical lifetimes of these tracers range from three months for CO to years for N_2O and CH_4. Hence, they are sensitive to types of transport that occur on entirely different time scales. This chapter summarizes research undertaken in four areas: designing and building a new spectrometer for *in situ* stratospheric studies, analysis of CO measurements from ALIAS on the ER-2 aircraft, intercomparisons with other instruments and model predictions, and analysis of N_2O and CH_4 measurements from ALIAS II on a balloon payload.

6.1 Instrument Description

The Aircraft Laser Infrared Absorption Spectrometer II (ALIAS II) is an open-path, tunable diode laser (TDL), mid-infrared absorption spectrometer. It was designed and built by the author in collaboration with the Atmospheric Laser Spectroscopy Group at JPL as a smaller, more rugged version of ALIAS, which flies on the ER-2 aircraft. The purpose of ALIAS II is to make *in situ* measurements of trace gases at altitudes up to 30 km in the stratosphere, where

previously there have been few accurate, *in situ,* measurements. ALIAS II currently measures N_2O and CH_4, but could measure other infrared-active gases by simply changing TDLs. This is an extremely sensitive instrument that uses the 2f harmonic spectroscopy technique to measure absorptions as small as 1 part in 10^5, corresponding to less than 1 ppb of CH_4 or N_2O. Instrument accuracy is estimated to be ±5% over the pressure range of 30 to 500 hPa and ±10% at pressures less than 20 hPa. Accuracy is limited mainly by thermal drifts in the electronics. Flight precision is typically ±3%, limited by the stability of the optical alignment. These levels of accuracy and precision are adequate for scientific analysis of the N_2O and CH_4 data, but have the potential to be even better so that less abundant, reactive species such as HCl, NO_2, or HNO_3 could be measured by ALIAS II in the future.

6.2 CO Measurements and Analysis

CO was measured *in situ* in the upper troposphere and lower stratosphere by the ALIAS instrument during 58 flights of the ER-2 aircraft, spanning latitudes from 3°S to 90°N and altitudes up to 21 km. The author participated in the field support and calibration of ALIAS on many of these flights. ALIAS measured CO as part of two NASA ER-2 campaigns: Stratospheric TRacers of Atmospheric Transport (STRAT) in 1995 to 1996 and Photochemistry of Ozone Loss in the Arctic Region In Summer (POLARIS) in 1997. Based on these flights, we have established a CO climatology for the upper troposphere and lower stratosphere. This climatology will be particularly useful as a

reference for observations by future remote sensing instruments of the Earth Observing System (EOS), including the Measurements of Pollution in the Troposphere (MOPITT) instrument and the Tropospheric Emission Spectrometer (TES).

We have observed that CO mixing ratios are slightly lower in the upper troposphere than in the marine boundary layer, but have a similar seasonal cycle with maximum CO in autumn and winter and minimum CO in spring and summer. However, in Alaska, the highest CO mixing ratios in the upper troposphere were measured in June and July, 1997. It is hypothesized that forest fires are the source of this additional CO in the high latitude upper troposphere.

In the tropics, CO does not appear to have a significant seasonal cycle. In the upper troposphere, 60±5 ppb CO was measured by ALIAS over the central Pacific Ocean (10°N to 3°S, 150° to 160°W) on five flights. This abundance of CO is typical of remote tropical areas uncontaminated by biomass burning. At the tropical tropopause, there is consistently 58±5 ppb CO. In the lower stratosphere, CO decays due to photochemical loss. Simultaneous measurements of OH by the Harvard HO_x instrument imply that the photochemical lifetime of CO in the tropical lower stratosphere is 100±35 days. The tropical profile of CO is reproduced extremely well by a simple Lagrangian box model of tropical ascent using measured CH_4 and OH concentrations, Cl and $O(^1D)$ concentrations from a photochemical model, and diabatic heating rates from an independent radiative heating model. This

implies that the measurements, modeled radicals, heating rates, and reaction rate coefficients have a high level of consistency.

The relatively short photochemical lifetime of CO makes it a useful tracers of rapid motions in the lower stratosphere. Based on ALIAS measurements, the seasonal mean CO mixing ratios on a given isentropic surface decrease slightly from the equator to mid-latitudes in the lower stratosphere. Mid-latitude CO displays a significant seasonal dependence which implies that transport is faster during winter than during summer. Assuming that the dominant meridional motion in the lower stratosphere (below 20 km) is quasi-horizontal transport along isentropic surfaces, then the meridional decrease in CO corresponds to poleward transport time scales of less than one month. However, CO has a large vertical gradient above the tropopause, so vertical mixing by eddies should be considered as another means of transport. Vertical eddy diffusion coefficients K_z are not well quantified for the lower stratosphere, but are estimated to be of the order of 10^4 cm^2s^{-1} at mid-latitudes and smaller in the tropics. On a given isentropic surface, the difference between tropical and mid-latitude CO is typically ≤ 10 ppb. In the mid-latitude lower stratosphere, CO mixing ratios decrease by 10 ppb over a vertical distance of approximately 1.5 km. By a simple order of magnitude calculation, CO can diffuse a vertical distance L = 1.5 km on a time scale $t \approx L^2/K_z$ which is roughly one month. In future work, we will incorporate eddy diffusion into the model of CO transport. Other possible reasons why the CO isopleths are so flat include subtropical stratosphere-

troposphere exchange and relatively fast photochemical loss of CO in the tropics.

6.3 Intercomparisons

ALIAS II has flown six times on a balloon platform, measuring N_2O and CH_4 from 7 to 30 km altitude in the tropics (7°S), mid-latitudes (34°N), and high latitudes (65°N). These balloon measurements show vertical profiles similar to previous measurements by balloon and satellite instruments. Comparisons with other N_2O and CH_4 measurements indicate that ALIAS II measurements have an accuracy of ±5% in the pressure range of 30 hPa to 70 hPa. N_2O measurements at higher pressures are excellent, but CH_4 appears to have a systematic offset of -100 ppb at pressures between 100 hPa and 200 hPa. This offset occurs when the balloon passes through the region of lowest temperatures near the tropopause, and may be associated with uncertainties in the temperature dependence of CH_4 spectral parameters. Comparisons with the Caltech-JPL 2D model indicate that at all latitudes, the model overpredicts N_2O, CH_4, and CFC-11 (measured by the Lightweight Airborne Chromatograph Experiment on the same payload). Inaccurate parameterization of radiative transfer in the 185 to 210 nm spectral window could be the cause of this discrepancy.

6.4 Entrainment Time Scales Inferred from N_2O and CH_4

The ALIAS II measurements of N_2O and CH_4 are important because they have provided accurate tropical profiles of these gases, *in situ* observations of the CH_4 *vs.* N_2O tropical and extra-tropical correlations, and observations of Arctic polar vortex remnants above the altitude of the ER-2 aircraft. The functional relationship between CH_4 and N_2O is a linear, compact correlation throughout the lower stratosphere ($230 \leq N_2O \leq 310$ ppb) because both species have photochemical lifetimes in excess of 10 years at low altitudes and are thus in gradient equilibrium. For $N_2O < 230$ ppb (altitudes above 26 km in the tropics), there are different relationships between CH_4 and N_2O in the tropics and extra-tropics because mixing is slow between these regions. The extra-tropical relationship is established by rapid mixing in the mid-latitude "surf zone." Young air is rapidly transported to mid-latitudes from the tropics, where it is mixed with old air from the Arctic polar vortex. Deviations from the normal extra-tropical relationship are indicative of unmixed air parcels that originated either in the tropics (high CH_4 and N_2O) or in the polar vortex (low CH_4 and N_2O).

We use observed vertical profiles of N_2O and CH_4 and a simple Lagrangian box model to calculate the time scale for entrainment of mid-latitude stratospheric air into the tropics. This time scale is estimated to be 7^{+10}_{-7} months for altitudes between the tropical tropopause and 20 km, and 16^{+18}_{-8} months for 20 to 28 km. The error bars include a 60% uncertainty in tropical heating rates at pressures greater than 50 hPa, but the CO analysis indicates that the actual uncertainty is smaller. Hence, the error bars on the entrainment

time scales are probably smaller than shown here. The important point about these time scales is that at altitudes below 20 km, there is rapid transport from the tropics to mid-latitudes (inferred from CO) and slower but still significant transport from mid-latitudes to the tropics (inferred from N_2O and CH_4). Tropical CO is relatively insensitive to entrainment of extra-tropical air into the tropics because the 7 month entrainment time scale is twice as long as the CO photochemical lifetime. Transport from mid-latitudes to the tropics is slowest at altitudes between 20 and 28 km. These results are in quantitative agreement with time scales inferred from other tracer measurements (see Chapter 1).

The tracer measurements and transport time scales presented in this thesis have broader implications for public policy. Rapid meridional mixing between the tropics and mid-latitudes below 20 km implies that pollutants (mainly NO_x, H_2O, sulfur compounds, and soot) released by supersonic aircraft in the mid-latitude lower stratosphere may be transported to the tropics. Once in the tropics, diabatic ascent efficiently transports material to the dominant region of O_3 production. Elevated NO_x causes catalytic loss of O_3 in the middle stratosphere. H_2O released by aircraft could increase stratospheric H_2O abundances with potential impacts on the radiative balance of the stratosphere and on heterogeneous chemistry. If H_2O mixing ratios increased, then polar stratospheric clouds could condense at higher temperatures, activate more Cl, and cause more O_3 loss in the polar vortices. In addition, sulfate aerosol or soot could act as reactive surfaces for heterogenous chemistry or as condensation nuclei for volatile particles. Supersonic aircraft flying above 20 km at mid-latitudes would have a smaller impact on the tropical stratosphere

because transport is slow from the mid-latitudes to the tropics at these altitudes. However, the NO_x released by these aircraft would still reduce O_3 abundances at mid-latitudes.

The impact on O_3 of future supersonic aircraft or another anthropogenic perturbations to the atmosphere can only be predicted with comprehensive global atmospheric models. These models can be calibrated with tracer measurements and transport time scales such as those described in this thesis. Given the true three-dimensional nature of atmospheric transport, it is unlikely that two-dimensional models could ever perfectly simulate the stratosphere. However, they remain a useful tool for assessing global change. A challenge to the field measurement community is to provide accurate tracer observations over a wide range of latitudes, altitudes, seasons, and phase of the quasi-biennial oscillation (QBO) to further constrain atmospheric models.

GLOSSARY

Brewer-Dobson circulation. The mean meridional circulation pattern of the stratosphere in a Lagrangian sense: air crosses the tropical tropopause, rises in the tropics, is transported poleward, and descends at middle and high latitudes.

cold-shield. A reflective metal cover that is situated between the external cover and the cold finger of a Dewar. It blocks thermal infrared radiation emitted by the external cover.

Dewar. An insulated container for holding cryogens such as liquid nitrogen. Thermal conduction and radiation are minimized by isolating the cryogen inside a vacuum jacket with many layers of reflective tape.

gondola. The aluminum structure that holds instruments, batteries, et cetera, on a balloon payload.

Herriott cell. A pair of concave mirrors facing each other, such that light injected at a specified angle through a hole in one mirror is reflected multiple times between the mirrors before exiting the same hole.

middleworld. The layer of the atmosphere between the mid-latitude tropopause and the surface of 380 K potential temperature. Within this layer, adiabatic stratosphere-troposphere exchange can occur along isentropic surfaces that connect the tropical troposphere to the extra-tropical stratospheric middleworld.

open-path cell. An optical absorption cell that is open to the atmosphere and does not require air to be pumped through it.

overworld. The layer of the stratosphere above the surface of 380 K potential temperature. All of the air in the overworld entered the stratosphere through the tropical tropopause, in contrast to the middleworld.

stratosphere. The layer of the atmosphere above the troposphere and below the mesosphere, in which temperature increases with height due to absorption of solar radiation by O_3. The optical depth in the O_3 Hartley and Huggins bands reaches unity in the stratosphere.

subtropics. The transition region between the mid-latitudes and the tropics, typically at 15° to 25° latitude. The ratio of reactive nitrogen (NO_y) to O_3 has a large meridional gradient in the subtropical stratosphere due to slow transport from mid-latitudes to the tropics.

telemetry. Radio signal stream transmitted from a balloon payload.

tropopause. The boundary between the troposphere and stratosphere. The tropopause location is determined by a radiative balance between the convective regime in the troposphere and solar heating in the stratosphere. In the tropics, the tropopause is located approximately at the 370 K isentrope. Outside the tropics, the tropopause is defined as the surface of constant potential vorticity equal to 2×10^{-6} $m^2 s^{-1} K kg^{-1}$.

troposphere. The lowermost region of the atmosphere. The troposphere is heated from below by absorption of solar radiation at the surface, and undergoes convection.

volume mixing ratio. Mole fraction.

APPENDIX 1: HERRIOTT CELL EQUATIONS

[based on Herriott et al., 1964; Altmann et al., 1981; and Trimble, 1988]

The Herriott cell is an optical cavity with a concave mirror on each end. If the two mirrors are not at a confocal separation, then it is possible to set up off-axis reflections between them that enter and exit the cavity at the same point. Herriott cells are used in spectroscopy as multipass optical cells because they are extremely stable and less likely to experience interference fringes than White cells. Herriott et al. [1964] derived the mathematical description of the Herriott cell and Altmann [1981] first described its use in infrared absorption spectroscopy. Here is a derivation of the relevant equations, based on these publications.

Part I: Ray Optics, Matrix Method

For this analysis, consider two spherical concave mirrors of focal length f and mirror separation d. The initial ray is injected through a hole in mirror 0, as shown in Figure X. The z coordinate is located along the axis of the Herriott cell, and x and y are perpendicular to it. Assume that z_r, the z coordinate of the point of intersection of the ray and the mirror, is approximately the same as z_a, the z coordinate of the mirror apex (i.e., center). In this case, the mirror system is mathematically equivalent to a series of thin lenses of focal length f,

with equal spacing d (see Figure X). Using the matrix method of ray optics [Jenkins and White, 1976], a ray that has just passed through lens n is represented by the column vectors

$$\vec{X}_n = \begin{pmatrix} x_n \\ x_n' \end{pmatrix} \text{ and } \vec{Y}_n = \begin{pmatrix} y_n \\ y_n' \end{pmatrix}.$$

The point of intersection of the ray and the center plane of lens n is (x_n, y_n), and the projections of the ray slope after refraction by lens n are:

$$x_n' = \frac{dx}{dz} \text{ and } y_n' = \frac{dy}{dz},$$

in the x-z and y-z planes, respectively.

By radial symmetry, the x and y components are equivalent in the general solution. Consider only the x component for now. At the entrance to the first mirror,

$$\vec{X}_0 = \begin{pmatrix} x_0 \\ x_0' \end{pmatrix} \tag{A.1}$$

Where the ray intersects the second Herriott cell mirror,

$$\vec{X}_1 = \begin{pmatrix} x_0 + x_0' d \\ x_0' \end{pmatrix} = \begin{pmatrix} 1 & d \\ 0 & 1 \end{pmatrix} \begin{pmatrix} x_0 \\ x_0' \end{pmatrix} \tag{A.2}$$

because any traverse of horizontal distance d can be represented by the matrix $D = \begin{pmatrix} 1 & d \\ 0 & 1 \end{pmatrix}$. Likewise, passage through a thin lens (i.e., our representation of

a mirror reflection) is represented by the matrix $F = \begin{pmatrix} 1 & 0 \\ -1/f & 1 \end{pmatrix}$. After the ray has traversed the Herriott cell once and been reflected,

$$\vec{X} = \begin{pmatrix} 1 & 0 \\ -1/f & 1 \end{pmatrix}\begin{pmatrix} 1 & d \\ 0 & 1 \end{pmatrix}\begin{pmatrix} x_0 \\ x_0' \end{pmatrix} = \begin{pmatrix} 1 & d \\ -1/f & 1-d/f \end{pmatrix}\begin{pmatrix} x_0 \\ x_0' \end{pmatrix} \tag{A.3}$$

Define $H = \begin{pmatrix} 1 & d \\ -1/f & 1-d/f \end{pmatrix}$ as the matrix transformation representing one pass of the Herriott cell. After n passes,

$$\vec{X}_n = H^n \vec{X}_0 \tag{A.4}$$

A theorem of matrix algebra states that

$$\begin{pmatrix} A & B \\ C & D \end{pmatrix}^n = \frac{1}{\sin\theta}\begin{pmatrix} A\sin(n\theta) - \sin(n-1)\theta & B\sin(n\theta) \\ C\sin(n\theta) & D\sin(n\theta) - \sin(n-1)\theta \end{pmatrix} \tag{A.5}$$

where $\cos\theta = \frac{1}{2}(A + D)$. (A.6)

Applying equation (A.4) to equation (A.3),

$$\begin{pmatrix} x_n \\ x_n' \end{pmatrix} = \frac{1}{\sin\theta}\begin{pmatrix} \sin(n\theta) - \sin(n-1)\theta & d\sin(n\theta) \\ -\frac{1}{f}\sin(n\theta) & \sin(n\theta) - \frac{d}{f}\sin(n\theta) - \sin(n-1)\theta \end{pmatrix}\begin{pmatrix} x_0 \\ x_0' \end{pmatrix} \tag{A.7}$$

and $\cos\theta = 1 - \frac{d}{2f}$ (A.8)

Applying equation (A.8) to a right triangle,

$$\sin\theta = \frac{1}{2f}\sqrt{d(4f - d)}. \tag{A.9}$$

Now by the trigonometric identity for $\sin(\alpha+\beta)$,

$$\sin((n-1)\theta)=\sin(n\theta)\cos(\theta)-\sin(\theta)\cos(n\theta). \tag{A.10}$$

Expanding equation (A.7), the first term is

$$x_n=\frac{x_0\sin(n\theta)}{\sin\theta}-\frac{x_0\sin(n-1)\theta}{\sin\theta}+\frac{x_0' d\sin(n\theta)}{\sin\theta}. \tag{A.11}$$

After substitution of equations (A.9) and (A.10) into (A.11), this reduces to:

$$x_n=x_0\cos(n\theta)+\sqrt{\frac{d}{4f-d}}\left(x_0+2fx_0'\right)\sin(n\theta), \tag{A.12}$$

which is equation (1) in Herriott et al. [1964]. Likewise for the slope x_n', substitution of equations (A.8), (A.9), and (A.10) into (A.7) gives

$$x_n'=x_0'\cos(n\theta)-\sqrt{\frac{d}{4f-d}}\left(x_0'+\frac{2x_0}{d}\right)\sin(n\theta). \tag{A.13}$$

The corresponding equations in the y coordinate are:

$$y_n=y_0\cos(n\theta)+\sqrt{\frac{d}{4f-d}}\left(y_0+2fy_0'\right)\sin(n\theta) \tag{A.14}$$

and

$$y_n'=y_0'\cos(n\theta)-\sqrt{\frac{d}{4f-d}}\left(y_0'+\frac{2y_0}{d}\right)\sin(n\theta). \tag{A.15}$$

Part II, Closure Condition

If the term $\sqrt{\frac{d}{4f-d}}$ is real, then we have the condition $0 < \frac{d}{f} < 4$ which is required for a stable mirror system. In the following analysis, only solutions for $d \leq 2f$ will be considered. With a phase shift α, equation (A.12) can be rewritten as

$$x_n = A\sin(n\theta + \alpha). \tag{A.16}$$

Likewise for the y coordinate, equation (A.14) becomes

$$y_n = B\sin(n\theta + \beta). \tag{A.17}$$

The parametric equations (A.16) and (A.17) describe an ellipse in the x-y plane. This is the general shape of the spot pattern seen on a Herriott cell mirror, as shown in Figure X, with even-numbered spots on mirror 0 and odd-numbered spots on mirror 1. From equations (A.16) and (A.17), the polar angle projected onto the x-y plane between any two consecutive spots is θ. The condition for the ray to return to its starting point (x_0, y_0) on mirror 0 is:

$$n\theta = 2\pi\mu, \tag{A.18}$$

where n is the number of spots (both mirrors superimposed) and μ is the number of times the spot pattern travels around the ellipse. To verify this condition, we substitute equation (A.18) into (A.12) and (A.14) to get $x_n = x_0$

and $y_n = y_0$. If there is a hole in mirror 0 at (x_0, y_0), then both entrance and exit beams will pass through it.

Depending on the mirror separation *d*, there are different symmetries to the Herriott cell spot patterns. What follows is a published case for $f \le d < 2f$ [Altmann et al., 1981]. First consider $d = f$: from equation (A.8), $\theta = \pi/3$ and closure is achieved for $n = 6$ passes and $\mu = 1$. This ray trace has D_3 symmetry for circular spot patterns. If the mirrors are separated slightly greater than *f*, the sixth pass misses the exit hole and the polar angle $\theta > \pi/3$. When $\mu = 2$, there is closure after $n = 10$ passes. At greater mirror separations *d*, the pattern continues with closure achieved for

$$n = 4\mu + 2, \quad \mu = 1,2,3,... \tag{A.19}$$

From equation (A.18), the corresponding polar angle

$$\theta = \frac{2\pi\mu}{n} = \left(\frac{n-2}{2n}\right)\pi, \tag{A.20}$$

and equation (A.8) is solved for the corresponding mirror separation

$$d = 2f\left[1 - \cos\left(\frac{n-2}{2n}\right)\pi\right]. \tag{A.21}$$

In general, this family of optical solutions has $D_{n/2}$ symmetry for circular spot patterns. As *n* increases, θ approaches $\pi/2$ and *d* approaches $2f$. An upper limit for the number of passes *n* is set by the requirement that the

(n-4)th spot does not overlap with the exit hole. At $d \approx 2f$, the spots overlap and the number of passes collapses to $n = 4$. For a flight instrument, the realistic upper limit to n is determined by the mechanical stability of the Herriott cell because the change in mirror separation d between adjacent configurations asymptotically approaches 0 for large n.

There are other families of beam patterns with different symmetries and closure conditions. The author has empirically found expressions for two families that have a large number of passes for $d \approx f$. With a visible HeNe laser and a Herriott cell, the author determined that for $d \leq f$, $\theta \leq \pi/3$ and closure is achieved if

$$n = 6\mu + 2, \quad \mu = 1,2,3,\ldots, \tag{A.22}$$

$$\theta = \left(\frac{n-2}{3n}\right)\pi, \tag{A.23}$$

and the corresponding mirror separation

$$d = 2f\left[1 - \cos\left(\frac{n-2}{3n}\right)\pi\right]. \tag{A.24}$$

Table 2 on the following page is a list of some possible solutions to (A.24) for the 0.750 m focal length mirrors of ALIAS II.

#passes	theta	d/f	d (m)	pathlength (m)
8	45.00	0.58579	0.43934	3.515
14	51.43	0.75302	0.56477	7.907
20	54.00	0.82443	0.61832	12.366
26	55.38	0.86387	0.64790	16.845
32	56.25	0.88886	0.66664	21.332
38	56.84	0.90610	0.67958	25.824
44	57.27	0.91872	0.68904	30.318
50	57.60	0.92835	0.69626	34.813
56	57.86	0.93594	0.70195	39.309
62	58.06	0.94207	0.70655	43.806
68	58.24	0.94714	0.71035	48.304
74	58.38	0.95139	0.71354	52.802
80	58.50	0.95500	0.71625	57.300
86	58.60	0.95812	0.71859	61.799
92	58.70	0.96083	0.72062	66.297
98	58.78	0.96321	0.72241	70.796
104	58.85	0.96532	0.72399	75.295
110	58.91	0.96721	0.72540	79.794
116	58.97	0.96889	0.72667	84.294
122	59.02	0.97041	0.72781	88.793
128	59.06	0.97179	0.72885	93.293
134	59.10	0.97305	0.72979	97.792
140	59.14	0.97420	0.73065	102.291

Table 2. Herriott cell configurations based on (A.24) and focal length f = 0.750 m.

For $d \geq f$, $\theta \geq \pi/3$ and closure is achieved if

$$n = 6\mu - 2\,, \quad \mu = 1,2,3,\ldots, \tag{A.25}$$

$$\theta = \left(\frac{n+2}{3n}\right)\pi\,, \tag{A.26}$$

and the corresponding mirror separation

$$d = 2f\left[1 - \cos\left(\frac{n+2}{3n}\right)\pi\right]. \tag{A.27}$$

Both families of optical solutions have $C_{(\pi/2)v}$ symmetry.

Part III: Entrance and Exit Slopes

To simplify this discussion, define the x axis to be along the radius of the injection hole, which is at $(x_0, 0)$. Consider circular spot patterns: as shown in Figure X, the position of spot #1 is $(x_0 \cos\theta, x_0 \sin\theta)$ so the entrance ray slopes are:

$$x_0' = \frac{x_0}{d}(\cos\theta - 1) \tag{A.28}$$

and

$$y_0' = \frac{x_0 \sin\theta}{d}\,. \tag{A.29}$$

Substituting equation (A.8) into (A.28), we get

$$x_0' = -x_0/2f \tag{A.30}$$

regardless of the mirror separation d. Substituting equation (A.9) into (A.29),

$$y_0' = \frac{x_0}{2f}\sqrt{\frac{4f-d}{d}}, \tag{A.31}$$

so the y entrance slope depends on the mirror separation.

The exit slope is given by x_{n-1}', since the ray is not reflected off mirror 0 in the final pass n through the Herriott cell. Solving $\vec{X}_{n-1} = H^{n-1}\vec{X}_0$ for x_{n-1}',

$$x_{n-1}' = x_0/f + x_0' \tag{A.32}$$

and substitution of equation (A.30) into (A.32) yields an exit ray slope

$$x_{n-1}' = x_0/2f\,. \tag{A.33}$$

Likewise for y, $\vec{Y}_{n-1} = H^{n-1}\vec{Y}_0$ can be solved for y_{n-1}':

$$y_{n-1}' = y_0' \tag{A.34}$$

because $y_0 = 0$. Hence the exit slope is the x-z mirror image of the entrance slope (there is a sign change for the exit ray because it is in the -z direction). If the entrance slope is fixed, then the exit slope will not change, regardless of mirror separation.

BIBLIOGRAPHY

Altmann, J., R. Baumgart, and C. Weitkamp, Two-mirror multipass absorption cell, *Appl. Optics, 20,* 995-9, 1981.

Herriott, D., H. Kogelnik, and R. Kompfner, Off-Axis Paths in Spherical Mirror Interferometers, *Appl. Optics, 3,* 523-6, 1964.

Jenkins, F. A., and H. E. White, *Fundamentals of Optics*, 4th ed., McGraw-Hill, New York, 1976.

Trimble, C. A., unpubl., 1988

APPENDIX II: FLIGHTS OF ALIAS AND ALIAS II

In this appendix, we describe the flights made by ALIAS and ALIAS II. ALIAS is mounted inside a pod on the right wing of the NASA ER-2 high-altitude aircraft. Twenty five other experiments are aboard the aircraft, allowing simultaneous measurements of a large suite of tracers, reactive species, and meteorological parameters. From October, 1995, through December, 1996, this ER-2 payload participated in the Stratospheric TRacers of Atmospheric Transport (STRAT) campaign in order to investigate transport within the lower stratosphere and between the stratosphere and troposphere. In 1997, the same payload participated in the Photochemistry of Ozone Loss in the Arctic Region In Summer (POLARIS) campaign. Although the focal point of this campaign was stratospheric O_3, the tracer observations extended the STRAT record to new times of the year and higher latitudes. The entire series of ER-2 flights is shown in Table 3.

Table 3. Next three pages:

Deployment	Date	Flight Type	Duration	N2O	CH4	HCl	CO	Comments
STRAT 2	951020	test	1.5 hr	-	-	-	-	ALIAS failed due to halt on keyboard error
	951024	N. survey	8 hr	-	-	-	-	ALIAS failed due to heater wiring error
	951026	stair-step	5 hr	partial	partial	-	partial	Lines lost during cruise climb
	951031	stair-step	5 hr	full	full	-	full	Low N2O at high P; high CH4
	951102	transit	6 hr	full	full	-	full	
	951105	S. survey	8 hr	full	full	-	full	
	951107	stair-step	5.5 hr	TBD	full	-	full	Noisy CH4 and N2O; high CH4 at low P
	951109	transit	6 hr	full	full	-	full	
STRAT 3	960126	test	2 hr	full	full	full	full	9 sec. early
	960129	stair-step	5 hr	full	full	full	full	
	960201	N. survey	8 hr	full	full	full	partial	CO line lost at 80 ksec; low CH4; high N2O
	960202	stair-step	5 hr	full	full	-	partial	CO line lost at 73 ksec
	960205	transit	6 hr	full	full	-	-	Best N2O and CH4; CO line lost; possibly 9 sec. early
	960208	stair-step	2.5 hr	-	-	-	partial	Aircraft DC overvoltage; weird N2O and CH4; spikes
	960212	stair-step	3 hr	full	full	-	full	Low CH4 at low P; spikes
	960213	S. survey	8 hr	TBD	TBD	-	full	Poor N2O mode purity after 78 ksec; spikes
	960215	transit	6 hr	TBD	TBD	-	full	Low CH4; low laser power; spikes
STRAT 4	960718	test	2 hr	TBD	full	full	full	Very low CH4 on descent; spikes; extremely noisy N2O
	960722	N. survey	8 hr	TBD	-	partial	partial	60 sec. early; very low CH4; no descent; noisy CO after 59 ksec; spike
	960725	stair-step	5 hr	TBD	TBD	full	full	N2O is weird at high P; spikes
	960730	transit	6 hr	TBD	full	-	full	Good CH4; spikes
	960801	S. survey	8 hr	TBD	full	-	full	Good CH4; spikes
	960803	sunrise	5.5 hr	TBD	full	-	full	Low tropospheric CH4; spikes
	960805	stair-step	1 hr	TBD	partial	-	partial	Aircraft problem, data stops at 83.1 ksec; spikes
	960807	stair-step	2.5 hr	TBD	full	-	full	Good CH4; spikes
	960808	S. survey	6 hr	TBD	TBD	-	TBD	Low CH4 on descent; spikes (including CO)
	960810	transit	6 hr	TBD	TBD	-	TBD	Good CH4; spikes (including CO)
STRAT 5	960913	test	2 hr	full	full	-	full	Good CH4; low N2O; spikes
	960916	S. survey	8 hr	partial	partial	-	partial	High N2O; no descent data; spikes
	960918	test	2 hr	full	full	-	full	High N2O; spikes (including CO)
	960921	OMS comp.	5 hr	full	TBD	-	partial	N2O and CH4 are weird during dive and descent; noisy CO
STRAT 6	961204	test		TBD	TBD	-	TBD	Spikes (including CO)
	961206	transit		TBD	full	-	full	60 sec. early; spikes; good CH4; N2O low at high P (but dive is OK
	961208	stair-step		full	full	-	full	Very low CH4 (by 80-100 pbbv); N2O low at high P; spikes
	961209	stair-step		full	full	full	full	Very low CH4 (by 50-100 ppbv); N2O low at high P; spikes
	961211	S. survey		TBD	TBD	TBD	TBD	Very low CH4; no CH4 after 73.3 ksec; noisy N2O with large spikes
	961213	transit		full	full	full	full	Low CH4; spikes
	961216	N. survey		TBD	TBD	TBD	TBD	Very low CH4; partial descent data due to imod problem
	961218	N. survey		TBD	TBD	TBD	TBD	Very low CH4; spikes
	961219	stair-step		TBD	TBD	TBD	TBD	TBD

Deployment	Date	Flight Type	N2O intercomparison	CH4 intercomparison
STRAT 2	951020	test	-	-
	951024	N. survey	-	-
	951026	stair-step	3-5 ppbv higher than ATLAS after scaling	~ ACATS
	951031	stair-step	10 ppbv higher than ATLAS at low P (low at high P)	~ ACATS (bows up 50 ppbv at high P)
	951102	transit	5 ppbv higher than ATLAS at low P	~ ACATS (ACATS data is poor after 82 ksec)
	951105	S. survey	~ ATLAS, but 3-5 ppbv higher at high P	0-20 ppbv lower than ACATS (ACATS poor in dive)
	951107	stair-step	~ ATLAS, but bows at high P	~ ACATS, except 50 ppbv higher at low P
	951109	transit	no 951109 ATLAS data, but ~ 951105 ATLAS data	~ ACATS
STRAT 3	960126	test	~ ATLAS	~ ACATS (very limited ACATS data)
	960129	stair-step	4 ppbv lower than ATLAS at low P (bows at high P)	~ ACATS (very limited ACATS data)
	960201	N. survey	5-10 ppbv higher than ATLAS	30 ppbv lower than WAS; 80 ppbv lower than ACATS
	960202	stair-step	~ATLAS (bows during start of flight)	80 ppbv lower than WAS at low P; ~ ACATS
	960205	transit	0-3 ppbv higher than ATLAS	0-40 ppbv lower than WAS and ACATS
	960208	stair-step	weird	weird
	960212	stair-step	0-3 ppbv higher than ATLAS	~ ACATS and WAS (no WAS data available at low P)
	960213	S. survey	weird	0-40 ppbv higher than ACATS, ~ WAS (limited data)
	960215	transit	5 ppbv higher than ATLAS	~ WAS at high P, 50 ppbv higher than WAS at low P
STRAT 4	960718	test	extremely noisy ALIAS N2O	~ ACATS, except 100 ppbv lower on descent
	960722	N. survey	10 ppb>ATLAS at high P; 10 ppb<ATLAS at low P	20% too low
	960725	stair-step	weird	TBD
	960730	transit	TBD	0-30 ppbv lower than ACATS (~ 951105 ALIAS data)
	960801	S. survey	20% low	0-40 ppbv lower than ACATS (~ 951105 ALIAS data)
	960803	sunrise	TBD	60 ppbv lower than ACATS in upper troposphere
	960805	stair-step	14% high	30-40 ppbv lower than ACATS in upper troposphere
	960807	stair-step	20% high	~ ACATS at low P, 50 ppbv lower at high P
	960808	S. survey	TBD	0-30 ppbv lower than ACATS; descent CH4 too low
	960810	transit	TBD	no ACATS data available for comparison
STRAT 5	960913	test	0-5 ppbv higher than ATLAS after scaling	no ACATS data available for comparison
	960916	S. survey	0-8 ppbv higher than ATLAS after scaling	no ACATS data available for comparison
	960918	test	0-10 ppbv higher than ATLAS after scaling	no ACATS data available for comparison
	960921	OMS comp.	0-15 ppbv higher than ATLAS after scaling	no ACATS data available for comparison
STRAT 6	961204	test	0-15 < ATLAS in trop. ascent; 0-20 > ATLAS otherwise	no ACATS data available for comparison
	961206	transit	10-12 > ATLAS at low P; too low at high P (but dive OK)	~ ACATS or 20 ppbv higher
	961208	stair-step	ALIAS bows at high P; very limited ATLAS data	no ACATS data available for comparison
	961209	stair-step	ALIAS bows at high P; 0-4 ppbv > ATLAS at low P	50-100 ppbv lower than ACATS
	961211	S. survey	0-3 ppbv > ATLAS, except 8-15 ppbv too low in dive	~ 100 ppbv lower than ACATS
	961213	transit	0-10 ppbv > ATLAS at low P; 5 ppbv too low in dive	~ ACATS except too low at high P
	961216	N. survey	too low in trop. ascent, but gradually gets > ATLAS	TBD
	961218	N. survey	too low in trop. ascent, but gradually gets > ATLAS	50-100 ppbv lower than ACATS
	961219	stair-step	TBD	TBD

Deployment	Date	Flight Type	Submitted N2O file	Submitted CH4 file	Submitted HCl file	SubmittedCO file
STRAT 2	951020	test	-	-	-	-
	951024	N. survey	-	-	-	-
	951026	stair-step	NOBFIT.SCL	CH3NOBFIT.FLT	-	NOBFIT.COR
	951031	stair-step	NOBFIT.FLT	NOBFIT_CH3.FLT	-	103195.FLT
	951102	transit	110295.FLT	CH3SUMALL.FLT	-	110295.FLT
	951105	S. survey	1108COR.FLT	SUM12.FLT	-	110595.FLT
	951107	stair-step	1108COR.EDT (TBD)	110795.FLT	-	110795.FLT
	951109	transit	1108COR.FLT	110995_CH3.FLT	-	110995.EDT
STRAT 3	960126	test	012696.FLT	CH2_012696.FLT	012696.DAT	012696.COR
	960129	stair-step	012996.FLT2	CH2_012996.FLT	012996.DAT	012996.COR
	960201	N. survey	020196.FLT	020196.FLT	020196.DAT	020196.FLT
	960202	stair-step	020296.FLT	RDM_020296.FLT	-	020296.DAT
	960205	transit	020596.FLT	CH2_020596.FLT	-	-
	960208	stair-step	-	-	-	020896.FLT
	960212	stair-step	021296.FLT (TBD)	021296.FLT (TBD)	-	021296.COR
	960213	S. survey	TBD	TBD	-	021396.FLT
	960215	transit	021596_129COR.FLT (TBD)	TBD	-	021596.FLT
STRAT 4	960718	test	TBD	071896.EDT (TBD)	071896.DAT	071896.COR
	960722	N. survey	TBD	TBD	072296.EDT	072296.ASCENT
	960725	stair-step	TBD	TBD	072596.EDT	072596.COR
	960730	transit	TBD	073096.EDT (TBD)	-	073096.FLT
	960801	S. survey	TBD	080196.EDT (TBD)	-	080196.FLT
	960803	sunrise	TBD	080396.COR	-	080396.COR
	960805	stair-step	TBD	080596.COR	-	080596.COR
	960807	stair-step	TBD	080796.EDT	-	080796.EDT
	960808	S. survey	TBD	080896.FLT (TBD)	-	080896.EDT (TBD)
	960810	transit	TBD	081096.FLT (TBD)	-	081096.FLT (TBD)
STRAT 5	960913	test	091396_110.SCL	091396_0985.SCL	-	091396.COR
	960916	S. survey	2_091696_110.SCL	2_091696_0985.SCL	-	091696.FLT
	960918	test	091896_110.SCL	091896_0985.SCL	-	091896.FLT
	960921	OMS comp.	092196_110_NEW.SCL	TBD	TBD	092196.FLT
STRAT 6	961204	test	TBD	TBD	-	TBD
	961206	transit	TBD	120696_FIT.COR_NEW	-	120696.FLT
	961208	stair-step	120896.FLT	120896.COR_NEW	-	120896.FLT
	961209	stair-step	120996.EDT	120996_103.SCL	120996.DAT	120996.FLT
	961211	S. survey	TBD	TBD	TBD	TBD
	961213	transit	121396.SCL107	121396_103.SCL	121396.SCL049	121396.FLT
	961216	N. survey	TBD	TBD	TBD	TBD
	961218	N. survey	TBD	TBD	TBD	TBD
	961219	stair-step	TBD	TBD	TBD	TBD

POLARIS ER-2 Campaign

Deployment	Flight date	Description	length (hr)	N2O	CH4	HCl	CO	H2O
Pol. I	970416	test flight - no ALIAS or JPL water	1.98					
	970418	test flight - no ALIAS or JPL water	5.03					
	970422	southern survey from Ames, 1 dive - seal problem on Moo valve	7.64	----	----	----	----	G
	970424	ferry flight to Fairbanks, 1 dive	5.76	G	G	G	low!	H. hi
	970426	polar flight, 1 dive at pole, caught vortex edge	7.86	G	G	G	G	H. hi
	970430	sunrise SZA flight	6.4	G	G	tail	G	H. hi
	970502	integrated photolysis flight, 1 dive	7.46	G	G	G	G	H. hi
	970506	integrated photolysis flight, 2 dives	6.77	hi?	G	tail	low!	G (H bad)
	970509	sunset SZE flight	6.13	hi?	low	tail?	G	G - no H
	970511	stack flight	4.90	G	low	tail	G	G
	970513	Integrated photolysis, 1 dive - no HCl power ALIAS wet on landing, failed 4 times on ascent, then OK	6.57	G	low	----	G	G
Pol. II	970626	Integrated photolysis, N. and S. legs, 2 dives	7.42	G	G	tail	G	G
	970629	southern survey, 2 dives	6.61	G	G	tail	G	G
	970630	stack flight & OMS intercomparison	4.48	G	G	G	G	G
	970704	southern survey, 2 dives	8.09	G	G	G	G	H hi
	970707	polar flight, 1 dive	7.81	G	G	G	G	H hi
	970710	stack flight - ALIAS mode problems- data but no submission yet	5.69	----	----	----	----	H hi - esp at end
Pol. III	970908	integrated photolysis, 2 dives - CH4 mode problems	7.60	G	hi?	G	G	G
	970911	sunset SZA flight	4.16	G	G	G	G	H low at end
	970914	sunrise SZA flight - HOx failed	6.33	G	G	tail	G	G
	970915	sunrise SZA flight - HOx failed	6.55	G	G	G	G	G
	970918	integrated photolysis, 1 dive - CH4 low on ascent and dive	7.88	G	part low	G	G	H hi
	970919	noon SZA flight	7.12	G	G	tail	G	H hi
	970921	ferry flight to Hawaii, 1 dive - saw high-N2O, high-CH4 airmass soon after dive - HCl vs. N2O is high here	7.35	G	G	???	G	----
	970923	equatorial flight, 1 dive - no ALIAS data submitted yet	7.97	----	----	----	----	----
	970925	ferry to Ames	5.89	----	----	----	----	----

POLARIS Notes: "G" = good. ATLAS N_2O had problems all of Polaris III. When Harvard water ("H.") is higher than JPL, it tends to rise higher toward

the end of the flight. HCl "tails" are points at high N_2O that are higher than expected Cl_y.

As mentioned in Chapter 2, ALIAS II is mounted onto a balloon gondola with five other tracer instruments. This payload has made six balloon flights in 1996 and 1997 as part of the Observations from the Middle Stratosphere (OMS) campaign. The dates and locations of the ALIAS II flights are shown in Table 4.

OMS Balloon Flights:

Flight date (yymmdd)	Location	Latitude	Longitude
960610	Ft. Sumner, NM	34° N	104° W
960921	Ft. Sumner, NM	34° N	104° W
970214	Juazeiro do Norte, Ceará, Brazil	7° S	39° W
970630	Fairbanks, AK	65° N	148° W
971111	Juazeiro do Norte, Ceará, Brazil	7° S	39° W
971120	Juazeiro do Norte, Ceará, Brazil	7° S	39° W

Table 4. Flights of the OMS Balloon Payload.